Manganese as secondary electron donor in native bacterial reaction centers

Matei-Alexandru Ivanescu

A Thesis

In the Department

Of

Physics

Presented in Partial Fulfilment of the Requirements

For the Degree of

Masters of Science (Physics) at

Concordia University

Montreal, Quebec, Canada

August 2014

© Matei-Alexandru Ivanescu, 2014

CONCORDIA UNIVERSITY
School of Graduate Studies

This is to certify that the thesis prepared

By: Matei-Alexandru Ivanescu

Entitled: Manganese as secondary electron donor in native bacterial reaction centers

and submitted in partial fulfillment of the requirements for the degree of

Masters of Science (Physics)

complies with the regulations of the University and meets the accepted standards with respect to originality and quality.

Signed by the final examining committee:

Dr. Cristophe Grova Chair

Dr. Valter Zazubovits Examiner

Dr. Pablo Bianucci Examiner

Dr. Laszlo Kalman Supervisor

Approved by _____
Chair of Department or Graduate Program Director

_____
Dean of Faculty

Date 12th September, 2014.

Abstract

Manganese as secondary electron donor in native bacterial reaction centers

Matei-Alexandru Ivanescu

Catalytic water splitting by oxygenic photosynthetic organisms has provided a primary energy source for sustaining life for over 2 billion years. The incorporation of manganese ions by primitive photoautotrophs represents an evolutionary breakthrough in the transition from anoxygenic to oxygenic photosynthesis. This study presents the first time observation of electron donation from manganese to the oxidized dimer in native bacterial reaction centers. This has been achieved by simultaneously fulfilling three requirements: i) lowering the oxidation/reduction potential of the Mn^{2+} ions by coordination with bis-tris propane to as low as 332 mV ii) elevating the potential of the dimer by ~60 mV, and iii) increasing the lifetime of the charge-separated state. Kinetic analysis revealed that the first-order electron transfer proceeds with time constant of ~83 ms and the bound manganese must be about 22 Å away from the dimer. Changes in dipole moments of the bacteriochlorophyll monomers and the change of the polarizability of the dimer upon manganese binding suggest that Mn^{2+} could bind in two solvent-accessible cavities near the two monomers. Measurements of electron transfer from cyt c_2^{2+} to P^+ in an environment with high Mn^{2+} concentration reveal a disruption of the function of the natural secondary electron donor for the BRC which could have profound implications regarding the aforementioned evolutionary transition.

Acknowledgements

I would like to thank my supervisor, Dr. László Kálmán, for all the valuable help throughout the project and for keeping faith in me.

I would also like to thank my wife, Kathryn, and her family for all the help and support through this entire process and for taking care of everything for me to be able to finish. I don't think I would have gotten to this point without you.

A special thank you to my friend and lab colleague, Dr. Sasmit Deshmukh, for all the help with the work and for being supportive.

I would also like to thank my lab colleagues Charles Protheroe and Sarah Lag for interesting discussions.

Finally, I would also like to acknowledge the technical staff: Zeljko Bulut, Richard Allix, Aldo Dissegna, Gheorghe Dan Duru, Chris Kowalewski, and Robert Pisarsky for all technical support.

Table of Contents

Abbreviations

B	Bacteriochlorophyll monomer
BChl	Bacteriochlorophyll
B_L	Bacteriochlorophyll monomer L (active)
B_M	Bacteriochlorophyll monomer M (inactive)
Bpheo	Bacteriopheophytin
BRC	Bacterial reaction center
BTP	Bis-tris propane (1, 3-bis(tris(hydroxymethyl)methylamino)propane)
CAPS	N-cyclohexyl-3-aminopropanesulfonic acid
c.m.c.	Critical micelle concentration
Cyt c_2	Cytochrome c_2
Da	Dalton
DAD	Diaminodurene
EDTA	Ethylenediaminetetraacetic acid
E_M	Midpoint potential
H	Bacteriopheophytin
H_L	Bacteriopheophytin L (active)

H_M	Bacteriopheophytin M (inactive)
LDAO	Lauryldimethylamine-oxide
NIR	Near-infrared
P	Bacteriochlorophyll dimer, primary electron donor of BRC
PDB	Protein data bank
Q_A	Ubiquinone A, primary electron acceptor of BRC
Q_B	Ubiquinone B, secondary electron acceptor of BRC
Rb.	Rhodobacter
RC	Reaction center
TEN	Tris-HCl, EDTA, NaCl
TLE	Tris-HCl, LDAO, EDTA
Tris	Tris(hydroxymethyl)aminomethane
TX-100	Triton X-100
UV	Ultraviolet
VIS	Visible
WT	Wild type

List of Figures

List of Tables

List of Schemes

Introduction

1.1 Implications of the evolution from anoxygenic to oxygenic photosynthesis

Photosynthesis is the primary solar energy conversion process from light energy to chemical energy that allows photosynthetic organisms to sustain life. In photosynthesis, light from the Sun provides an inexhaustible energy source to fix carbon dioxide and split water, generating simple sugars used as energy sources for the organisms to grow and reproduce [1]. Photosynthetic organisms provide the first link in the food chain on Earth. Furthermore, oxygen, a by-product of catalytic water splitting in oxygenic photosynthesis, is crucial for vital processes in all aerobic life forms. The formation of oxygenic atmosphere is believed to be a consequence of the oxygen released by ancient photoautotrophs started about 2.8 billion years ago (Fig. 1.1) [2]. However, before oxygen evolving photosynthesis was developed, anoxygenic photosynthetic organisms had already existed for about a billion years (Fig. 1.1). In anoxygenic photosynthesis, organisms convert light energy to glucose without releasing oxygen. These anoxygenic photoautotrophs are believed to be the first examples of self-sustaining life [3]. The development of the ability to split water into molecular oxygen and protons is thought to be a pivotal moment in the evolution of life on Earth. The omnipresence of water, carbon dioxide and sunlight meant that photosynthetic organisms had a vast pool of resources. In the span of some 800 million years, oxygen participated in the oxidation of ferrous iron to ferric iron in the Archaean oceans [4]. Ultimately, the abundance of oxygen in the atmosphere led to the evolution of more advanced organisms capable of using aerobic respiration.

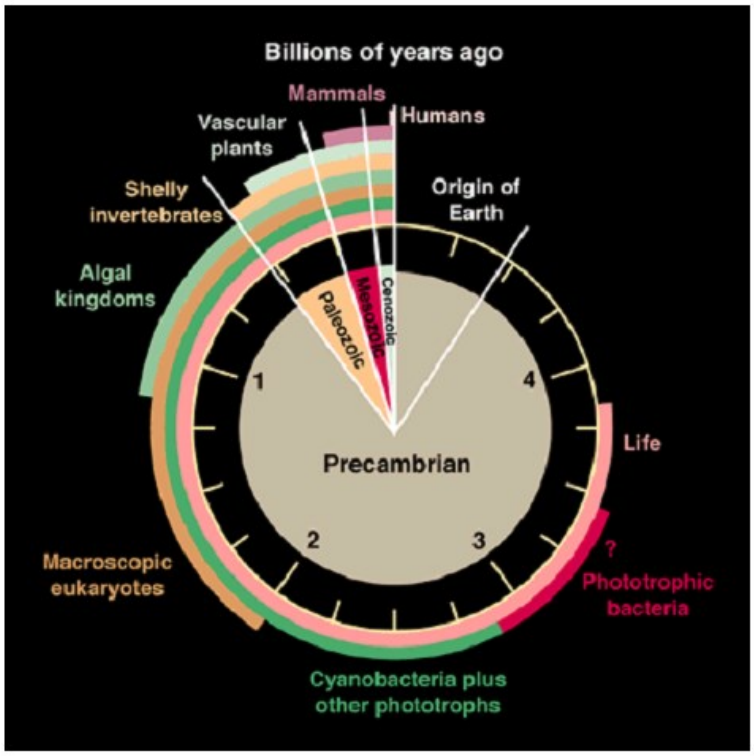

Figure 1.1 The biogeological clock of Earth. A symbolic representation of the Earth's 4.6 billion year history. The onset of life occurred ~3.8 billion years ago. Phototrophic anoxygenic bacteria appeared ~3.5 billion years ago. Evolution into oxygen evolving bacteria is dated back ~2.8 billion years ago in the Archaean ocean. Another ~800 million years were necessary for the development of the oxygenic atmosphere as the oxygen was used to oxidize all the ferrous iron to ferric iron. The oxygenic atmosphere facilitated the development of aerobic respiration, leading to the diversity of organisms on Earth today. Figure taken from [5].

Apart from generating energy, oxygen, and providing a primary food source, photosynthetic organisms also contributed both directly and indirectly to the majority of the world's fuel supply. The anaerobic decomposition of the remains of phytoplankton and zooplankton over the ages is responsible for the world's fossil fuel reserves [6]. Ethanol, which is used as a fuel source or fuel enhancer, is produced through the fermentation of photosynthetic biomass [7]. As the world's fuel supplies are dwindling and the by-products of fuel consumption are believed to be affecting the Earth's climate, there is a heightened search for renewable and clean fuel sources. One proposed variant to fossil fuels is hydrogen. Oxygenic photosynthesis consists of the splitting of water into oxygen and protons [8]. The latter can be fed to hydrogenase enzymes to produce

molecular hydrogen, which can ultimately be used as a clean fuel [9]. The potential use of photosynthesis as a component in producing alternative fuels requires a deeper understanding of the oxygen evolving process and the ability to replicate it successfully in artificial systems.

The importance of photosynthesis in the survival of life on Earth calls for an investigation into the possible onset of the evolutionary mechanism that led to the transition from anoxygenic to oxygenic photosynthetic organisms. Furthermore, this investigation can also provide a platform for artificial photosynthetic design by replicating oxygen evolution in a more rudimentary system like the bacterial reaction centers (BRCs). BRCs are the pigment-protein complexes responsible for the light-energy conversion in anoxygenic photosynthetic bacteria, while photosystem II (PS II) performs the same process in oxygenic photosynthesis. The two trans-membrane reaction centers share the same function: conversion of photon energy to create a proton gradient over a membrane. With the advance of X-ray crystallography, it has been shown that the two proteins have very similar structures [10]. Indeed, these similarities, combined with phylogenetic studies have established that BRCs and PS II share a common ancestor [11] (Fig. 1.2).

The current structure of the BRC is more similar to that of the common phototrophic bacterial ancestor than PS II is. Although functionally and structurally similar, the added complexity of PS II due to the additional subunits and cofactors hinders the study of energy conversion in oxygenic photosynthetic systems. Thus, it is more beneficial to conduct these studies on a simpler model like the BRC. The focus is on the BRC extracted from the anaerobically grown purple bacterium *Rhodobacter (Rb.) sphaeroides*. This pigment-protein complex has been extensively studied in order to determine the characteristics of the proton and electron transfer and the conformational changes related to these processes [12,13,14,15].

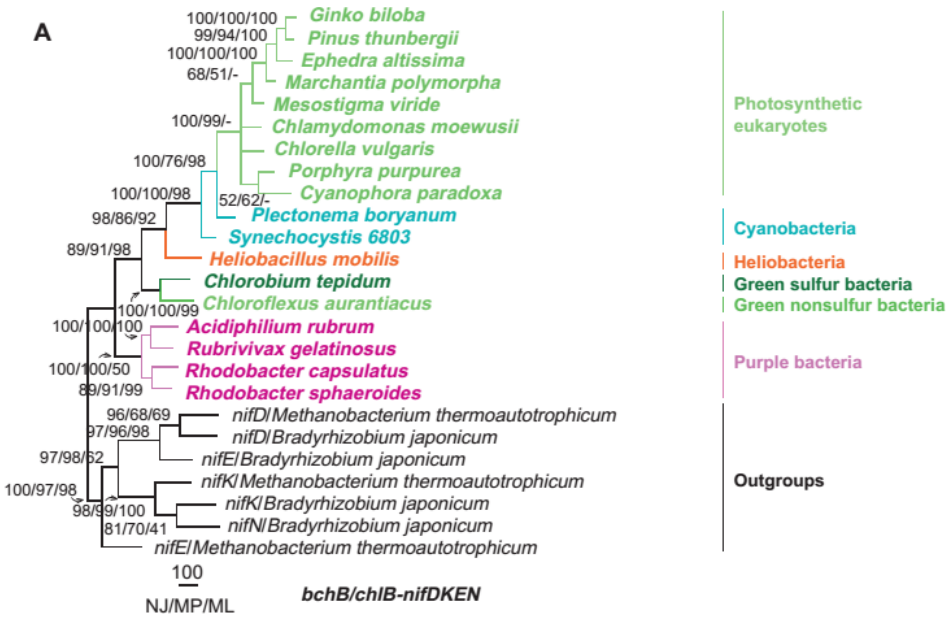

Figure 1.2 Phylogenetic tree for chlorophyll containing organisms from the Bacteria and Archaea groups. Anoxygenic photosynthetic organisms are purple, green nonsulfur and sulfur bacteria, while photosynthetic organisms are heliobacteria, cyanobacteria and the eukaryotes present in the tree. There is a common ancestor of both purple bacteria and photosynthetic organisms. Figure taken from [12].

1.2 Structural comparison of BRC from *Rhodobacter sphaeroides* and PS II from higher plants or cyanobacteria

The three-dimensional structure of both the BRC and PS II has been determined to a resolution of 1.9 Å [17,18] using X-ray crystallography. The BRC of *Rb. sphaeroides* is composed of ~800 amino acid residues arranged in three subunits and having a total mass of ~100 kDa (1Da = 1g/mol). The L (light), M (medium) and H (heavy) subunits each contain 5, 5 and 1 membrane-spanning helices respectively (Fig. 1.3 A). The nomenclature does not accurately describe the molecular weights of the respective subunits, but rather their mobility during electrophoresis on

SDS gel. There are a total of 9 cofactors associated with the L and M subunits: one bacteriochlorophyll (BChl) dimer (P) composed of two BChls, two BChl monomers (B_L and B_M), two bacteriopheophytins (H_L and H_M), one primary ubiquinone (Q_A), one secondary ubiquinone (Q_B) and a divalent non-heme iron. The cofactors are arranged around a pseudo-2-fold symmetry axis that passes through the center of the dimer and the non-heme iron, separating the L and M subunits. Although no cofactors are directly associated with the H subunit, it is thought that it plays a role in the electron transfer from Q_A^- to Q_B.

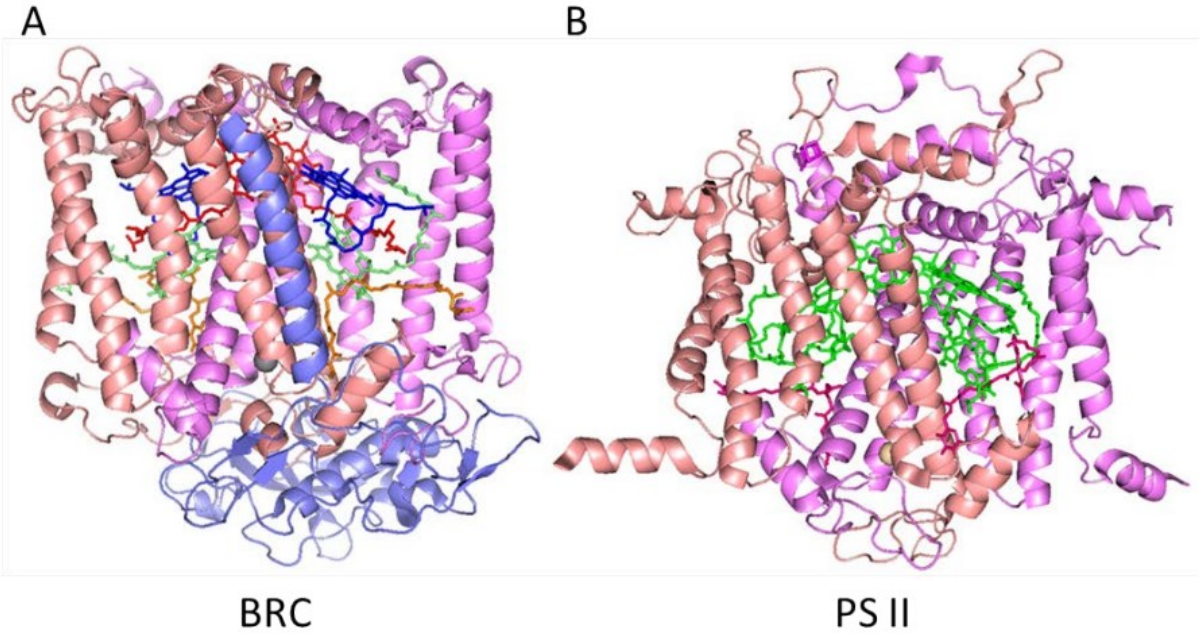

Figure 1.3 Structure of the BRC (A) and PS II (B). A. The arrangement of subunits in BRC: M (salmon), L (purple) and H (blue). 5 transmembrane helices span the L and M subunit and 1 transmembrane helix spans the H subunit. The nine cofactors are: BChl dimer (red), BChl monomers (blue), Bpheos (green), ubiquinones (orange) and non-heme iron (gray). The axis of symmetry for the cofactors passes vertically through the plane of the paper from the dimer to the non-heme iron. **B**. The core of the PSII protein. The arrangement of the D1 (purple) and D2 (salmon) subunits is shown, both consisting of 5 transmembrane helices. These subunits show a strong homology with the L and M subunit of the BRC with differences mainly in the C and N terminus regions. The chlorophylls and pheophytins are depicted in green, the plastoquinones in purple and the non-heme iron in light brown. PDB codes: BRC structure – 4RCR [19]; PS II structure – 1S5L [20].

PS II is a much more complex protein consisting of over 20 subunits and at least 99 cofactors. The core of the reaction center (RC), however, bears strong resemblance to the BRC. The D1

and D2 subunits both contain five transmembrane helices and have strong homology to the L and M subunits of the BRC (Fig. 1.3 B). The core also contains similar cofactors to the BRC cofactors: four chlorophyll molecules, two of which form a pair of chlorophylls ("special pair") with a strong absorbance band at 680 nm (P_{680}), two pheophytins, two plastoquinones, one non-heme iron and the oxygen evolving complex (OEC). The arrangement of these cofactors inside the core of the PS II also resembles that of the BRC, with a pseudo-two-fold symmetry axis going through the special pair and the non-heme iron, which separates the cofactors into two branches. The differences occur at the N and C terminal ends of the protein, as well as in the identity of the secondary electron donors. The OEC is the site of water oxidation. It is comprised of four Manganese (Mn) ions, which can have oxidation states from +2 to +4, one divalent calcium (Ca^{2+}) ion, as well as oxygen atoms and water molecules that help bridge the complex (Fig. 1.3). The OEC can store up to four charges generated from splitting water. However, the exact oxidation states of the manganese in various steps of the Kok cycle is still debated [21].

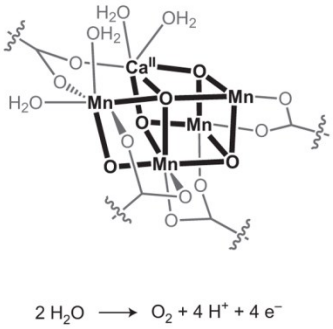

Figure 1.4 The oxygen-evolving complex. The complex is composed of four Mn ions, a Ca^{2+} ion and several oxygen and water molecules that bridge the complex. The Mn ions are utilised to store the electron equivalents . The chemical reaction of water splitting involves two water molecules transformed into molecular oxygen, four protons and four electrons in a four step process known as the Kok cycle. Figure taken from [22]**.**

Although light energy is harvested to produce a transmembrane proton gradient in both the BRC and PS II, the high oxidizing power of the P_{680}^{+} combined with the presence of the oxygen evolving complex enables it to split water. The dimer in BRC has a lower oxidizing power thus,

it requires lower potential electron donors (cytochromes) in order to maintain the electron transfer cycle.

1.3 Transmembrane charge separation in BRC and PS II

Light-induced electron transfer is a series of step-wise reactions starting with the absorption of a photon at P and resulting in a $P^{+}Q_{B}^{-}$ charge separated state. The charge separation has a quantum yield of nearly unity, making it the most efficient energy conversion process found in nature. The absorbed photon excites an electron from P, the primary electron donor, which is transferred sequentially through a group of intermediate acceptors (B_L, H_L and Q_A) before transferring to the final electron acceptor (Q_B) (Fig. 1.5A) [23]. The electron transfer occurs completely along the L branch. This is due to the lower energy level of B_L compared to B_M caused by the interaction of the cofactors with three natural lipids (glycolipid, phospholipid, and cardiolipin) [24]. The final electron acceptor in the chain is Q_B because it has a lower energy level than Q_A due to the higher degree of solvent accessibility of Q_B and the changes in the structure of the protein associated with the electron transfer. The electron transfer is exceptionally efficient because it is orders of magnitude faster in the forward direction than in the reverse direction (Fig. 1.5 B). This advantage is thought to be due to conformational changes occurring in the protein after light excitation [25].

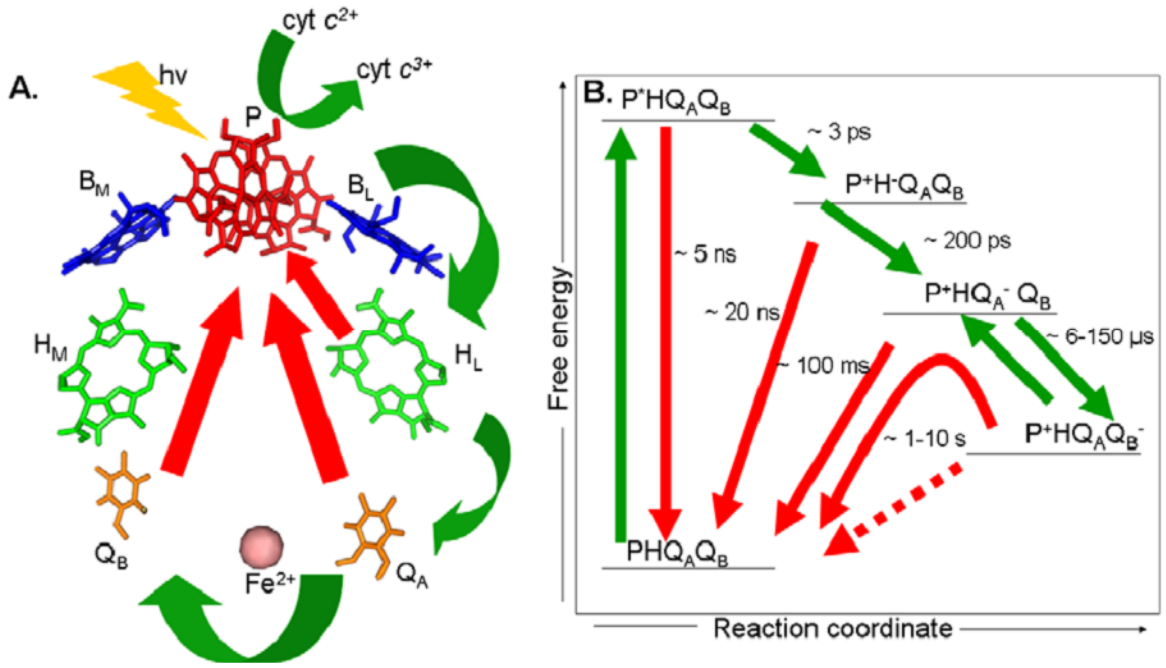

Figure 1.5 Light-induced electron transfer process in photosynthetic BRC. A. The light-induced electron transfer chain. The electron resulting from the light-excitation of the dimer travels down the L side from P to B, H, Q_A and Q_B. Phytyl chains of the tetrapyrrols were removed for clarity. B. The energy levels of various redox states formed in the electron transfer process are plotted with respect to the reaction coordinate. The lifetimes of the forward (green) and reverse (red) reactions are presented. Green arrows show the forward electron transfer while red arrows show the charge-recombination processes.

In order for the cycle to continue, the charge-separated state $P^+Q_B^-$ has to recover to the original state PQ_B. *In vivo*, Q_B can carry two electrons and absorbs two protons to form a quinol (Q_BH_2). The formation of Q_B^- causes the uptake of a proton from the cytoplasmic environment, which is coupled to a second electron transfer from Q_A^- to Q_B^- and a second proton uptake. The quinol dissociates and is oxidized by the cytochrome bc_1 complex followed by the subsequent release of protons and electrons across the membrane [25,26]. Conversely, P^+ is reduced by an external electron donor. In anoxygenic photosynthetic bacteria, cytochromes act as secondary electron donors. In laboratory environments, however, other secondary electron donors have also been used, such as ferrocene and 3,6 diaminodurene (DAD) [15]. In order for a molecule to act as a secondary electron donor, it has to have a lower oxidation-reduction potential than that of the

oxidized dimer (with a potential of 505 mV in dark-adapted native BRCs). The site of association between the secondary electron donor and the reaction center is in close proximity to the dimer [26].

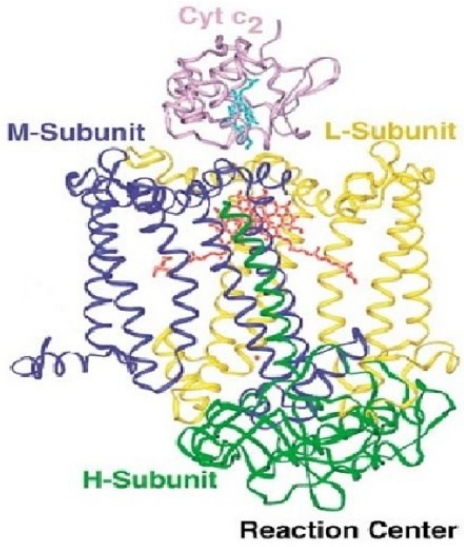

Figure 1.6 Cytochrome binding on the BRC in *Rhodobacter sphaeroides.* A cartoon representation of the association between cytochome c_2 (cyt c_2)and the BRC. The binding site rests at the top at approximately 10 Å from the dimer. Figure taken from [26].

The forward electron transfer process in PS II occurs in a very similar fashion [27] [28]. Light excitation of an electron on the special pair P_{680} is followed by an electron transfer to the nearby pheophytin. The electron is further shuttled to a plastoquinone in the Q_A site before arriving at the final electron acceptor, the plastoquinone at Q_B. The arrival of a second electron to Q_B is coupled to an uptake of two protons to form quinol. Similarly to BRC, slight changes in the cofactor environment of PS II lowers the energy levels in the D1 branch as opposed to the D2 branch, allowing for a unidirectional electron transfer along D1 [27]. The positively charged P_{680}^+ has a great oxidizing potential (~1.2V), which allows it to receive an electron from the

nearby manganese cluster with the help of a tyrosine residue [29]. The oxygen evolving complex extracts four electrons from two water molecules and stores them in the OEC. During the reaction, the water molecules are split into two oxygen molecules and four protons, which are released in the environment.

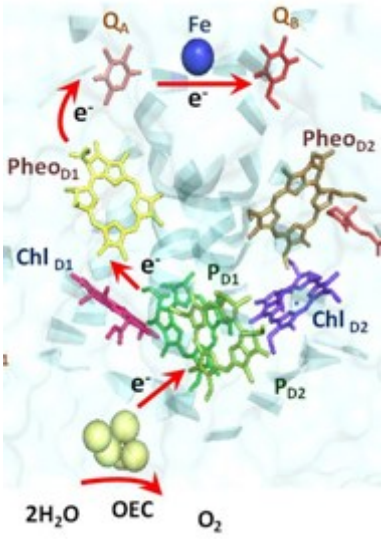

Figure 1.7 Arrangement of cofactors and the transmembrane charge separation in PS II. The cofactors of PS II are: four chlorophylls (two in the "special pair" P_{D1} and P_{D2} and two others Chl_{D1} and Chl_{D2}), two pheophytins ($Pheo_{D1}$ and $Pheo_{D2}$), two quinones (Q_A and Q_B), a non-heme iron (Fe) and the OEC. The electron is excited at P and is subsequently transferred down the D1 branch to $Pheo_{D1}$, Q_A and finally Q_B. The secondary electron is provided by the OEC which extracts four electrons from two water molecules. Figure taken from [30].

The inclusion of the multivalent Mn ions in the OEC is the key to understanding the mechanism of water splitting. In order for the evolutionary transition from anoxygenic to oxygenic photosynthetic organisms to have occurred, a redox interaction had to be established between manganese and an anoxygenic photosynthetic reaction center. By studying the possible association between manganese and the anoxygenic BRC, we can emulate the conditions that led to the development of the oxygen evolving cluster and assist in reproducing water splitting. Optical spectroscopy is a powerful tool that provides insight on the interactions of the protein with external factors and can yield critical information on the relationship between Mn and BRC.

1.4 Marcus-theory of electron transfer

The light-induced electron transfer in photosynthetic systems can be explained by Marcus theory. This formulation applies concepts used in vibrational state electron transitions to intermolecular electron transfer. The Franck-Condon principle states that the transition of an electron between two different electronic levels in a molecule is heavily dependent on the overlap between the wave functions of the two states. Similarly, in Marcus theory, the electron transfer from a donor molecule to an acceptor molecule is dependent on the overlap between the potential energy functions of the reactants and the products [31,32]. The potential energy functions originate from the harmonic oscillator model, and therefore can be considered as parabolas. The intersection of the two parabolas characterizes the conditions necessary for the electron transfer to occur (Fig. 1.8).

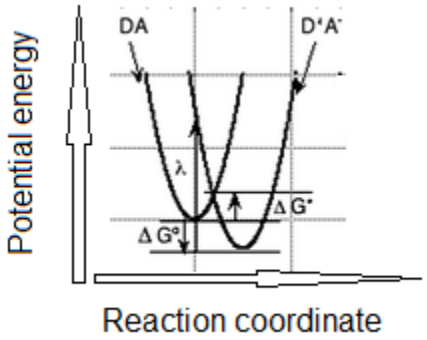

Figure 1.8 Potential Energy Diagram in Marcus Electron Transfer. The curves represent the potential energy with respect to the reaction coordinate (horizontal). The parabola on the left represents the donor-acceptor couple before the electron transfer (reactants), while the curve on the right represents the donor acceptor couple after the electron transfer (products). The reorganization energy (λ_0) is the energy necessary in order for the donor and acceptor to be in the state where electron transfer can occur. ΔG^0 is the standard reaction Gibbs free energy and $\Delta G^{\dagger}$ is the activation energy required for the electron transfer to overcome.

The reorganization energy (λ_0) represents the energy cost due to geometry modifications for the transfer of a unit of charge to occur. The equation for the determination of the activation energy ($\Delta G^{\dagger}$) of the electron transfer depends on the reorganization energy and the standard reaction Gibbs energy (ΔG^0) (Equation 1.1).

$$\Delta G^{\dagger} = \frac{(\lambda_0 + \Delta G^0)^2}{4\lambda_0} \tag{1.1}$$

The electron is transferred as an entity, meaning the point of intersection of the parabolas represents the value of activation energy for the process and not a transition state similar to those found in chemical reactions like substitution. The energy necessary for the transition in non-adiabatic Marcus electron transfer is provided by the environment. Solvation shells around the donor and acceptor molecules undergo thermally induced changes to accommodate the change in charge as part of the electron transfer. In this type of approach, the electronic coupling between donor and acceptor is considered weak and thus the thermal energy input from the surroundings is necessary to assist the electron transfer. In adiabatic electron transfer, the coupling between donor and acceptor is stronger and the electron can tunnel through the potential barrier.

The probability of the electron transfer is inversely proportional to the tunneling distance between the donor and acceptor molecules and is highly dependent on the surroundings. Photosynthetic reaction centers have evolved an extremely efficient electron transport chain based on small distances between donors and acceptors. Photosynthetic pigments contain conjugated porphyrin macrocycles that allow the distribution of the electron over a large area. In highly conjugated systems, the donor-acceptor distance is reduced to the distance between the closest points in the conjugation of each molecule (edge-to-edge distance). Typical tunneling distances of 4 to 24 Å have been reported for electron transfers in proteins which have rates

ranging twelve orders of magnitude [33]. The relationship between distance and electron transfer rate is exponential and depends on the packing factor β (Fig. 1.9).

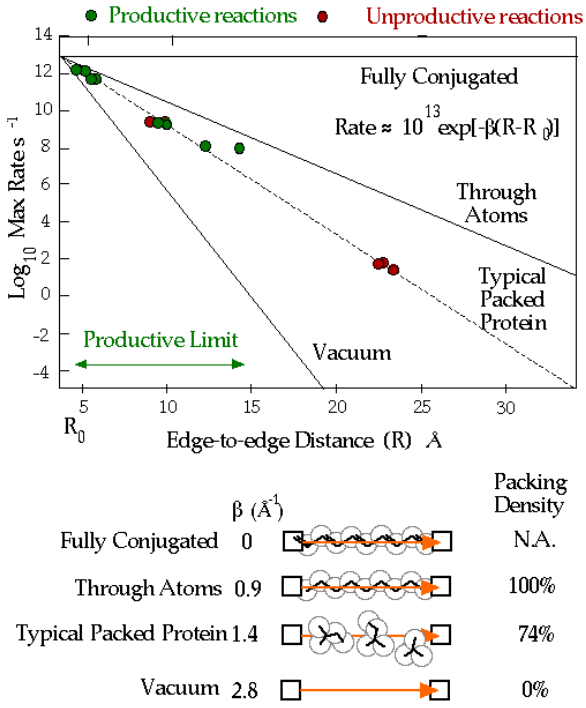

Figure 1.9. Relationship between donor-acceptor distance and rates in different environments. The electron transfer rates are dependent on the distance and the packing factor β which represents the slope of the regression lines in the graph. The packing factor in various different environments is analyzed. In fully conjugated systems, the electron transfer is distance independent. In vacuum, the electron transfer is the least efficient. The protein in the example is the BRC, which has a β of 1.4 Å^{-1}. Figure taken from [33]

The electron transfer in photosynthetic RCs is facilitated by the low dielectric constant in the immediate environment of the pigments [34]. The dielectric constant is very susceptible to the arrangement of the nearby amino-acids and the presence of charges in the vicinity. The high level of hydrophobicity in the core of the RC decreases the dielectric constant from that in solution.

1.5 Electronic Transitions in the Optical Spectrum of the BRC

The specific protein environment around the BChls, BPheos and quinones can be characterized using absorption spectroscopy. The high degree of conjugation in the pigment molecules associated with the BRC allows the π to π^* electronic transitions to no longer fall into the ultraviolet (UV) spectral region but rather into the visible (VIS) and into the near infrared (NIR) regions [35]. The electronic absorption spectrum of the BRC shows distinct features for each pigment due to the influence of the immediate environment. The complex structure of porphyrin molecules allows for two electronic transitions to take place (Q_X and Q_Y). The Q_X transition has a dipole moment in the plane of ring 4 to ring 2 while the Q_Y has a dipole moment in the plane of ring 3 to ring 1 (Fig. 1.10 B). In the absorption spectrum of the BRC, along the Q_Y transition moment the BChl dimer absorbs around 865 nm, BChl monomers (B_L and B_M) absorb around 800 nm, Bpheos (H_L and H_M) absorb around 760 nm and in the Q_X region, all BChls absorb around 600 nm and BPheos absorb around 540 nm (Fig. 1.10 A). The Soret band characteristic of porphyrin macrocycles is situated below 400 nm, while the 280nm band is typical of aromatic amino-acids such as tryptophans, tyrosines and phenylalanines. The higher level of conjugation in the Q_Y than in the Q_X means the electronic transition along Q_Y happens at lower energies than along Q_X. The level of conjugation in a single ring aromatic systems such as those found in Tyr, Trp, Phe amino acids is even smaller and that is why the $\pi \rightarrow \pi^*$ transition is detected in the UV spectral range. The electronic coupling between the two halves of the dimer causes a higher degree of conjugation and a shift of the absorption peak to higher wavelengths.

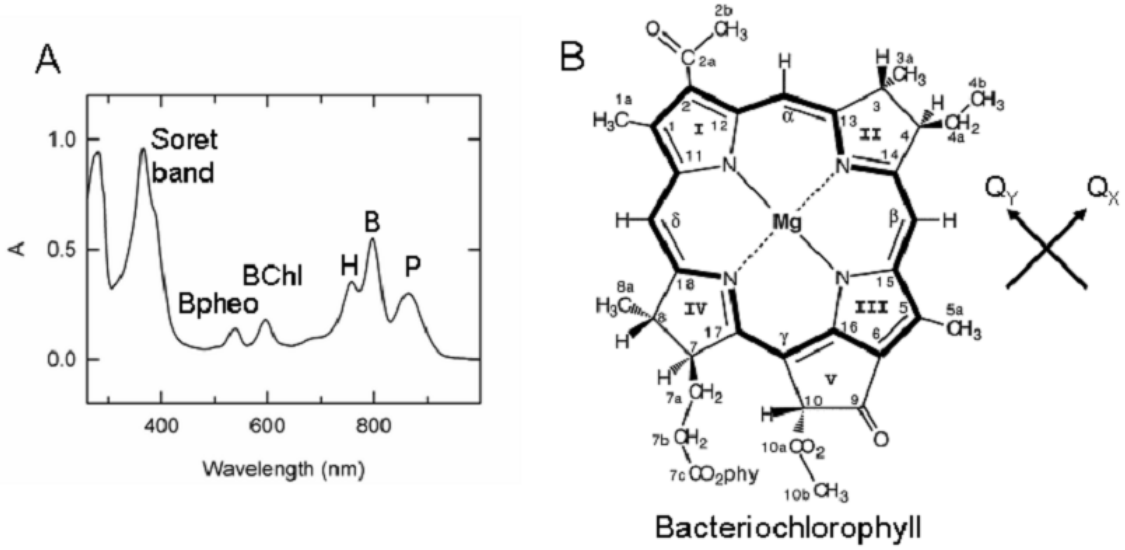

Figure 1.10 Electronic absorption spectrum of the BRC (A) and the structure of the bacteriochlorophyll molecule (B). A. In the optical spectrum of the BRC the Q_Y absorption peaks of the dimer (P), two monomers (B_L and B_M), and two bacteriopheophytins (H_L and H_M) are situated around 865, 797, and 760 nm, respectively. In the Q_X region bacteriochlorophylls (BChl) and bacteriopheophytins (Bpheo) absorb around 600 and 540 nm, respectively. B. The bacteriochlorophyll molecule is a tetrapyrrole macromolecule coordinated by a central magnesium. The Q_X dipole moment is formed between rings 2 and 4, while the Q_Y transition moment is defined between rings 1 and 3.

The sensitivity of the pigment molecules to surrounding electric fields allows local changes in the electrostatics to be monitored using optical spectroscopy. These changes are due to different protein conformation in reaction to stimuli such as illumination or interactions between the protein and other molecules in solution. The absorption bands of the pigments can be bleached, shifted, or broadened. Bleaching is due to the disappearance of a species, shifts are due to the changes in the polarization and broadenings are due to changes in dipole moment (Fig. 1.11) [36].

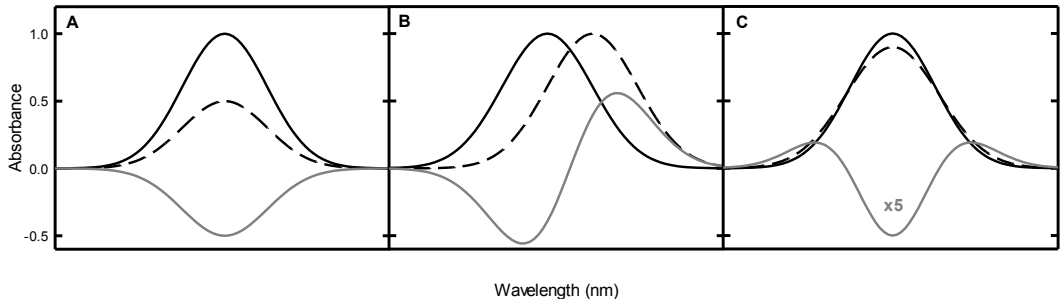

Figure 1.11 Electrochromic absorption changes observed in an optical spectrum. An absorption band can be bleached (A), shifted (B) or broadened (C) due to the changes of the permanent dipole of an absorbing molecule. Solid and dashed black lines represent the initial and final states, respectively. Gray solid lines represent difference spectra between the final and initial states. Bleaching is due to the disappearance of the absorbing species and can be used to monitor a reaction. Shifts are due to the change in polarizability and broadenings are due to changes in dipole moment of the molecule in response to changes in electrostatic interactions with the local electric field.

The presence of the light-induced charge-separated state P^+Q^- creates a dipole moment, which induces changes in the spectra of the cofactor. The light-minus-dark difference spectrum associated with the charge-separated state is presented in Figure 1.12 A. The light-minus-dark spectrum is obtained by taking the difference between the light-induced spectrum and the dark spectrum. The characteristics of the individual components of the light-minus-dark spectrum are: a bleaching of the P band due to the formation of P^+, a hypsochromic shift in the monomer band due to the presence of the the positive charge on P after charge separation and a bathochromic shift in the pheophytin band mainly due to the nearby negative charge on the quinone. A secondary electron donor to P^+ would remove the charge from the dimer, establishing the PQ^- state. The specific components of the light-minus-dark absorption spectra of this state (Fig. 1.12 B) are: a bathochromic shift on the pheophytin and a hypsochromic shift on the dimer due to Q^-. There is no visible change on the monomer because the distance between the Q_Y dipole moment of the monomers and the negative Q^- charge is large and the orientation of the electric field of the charge is perpendicular to the dipole moment.

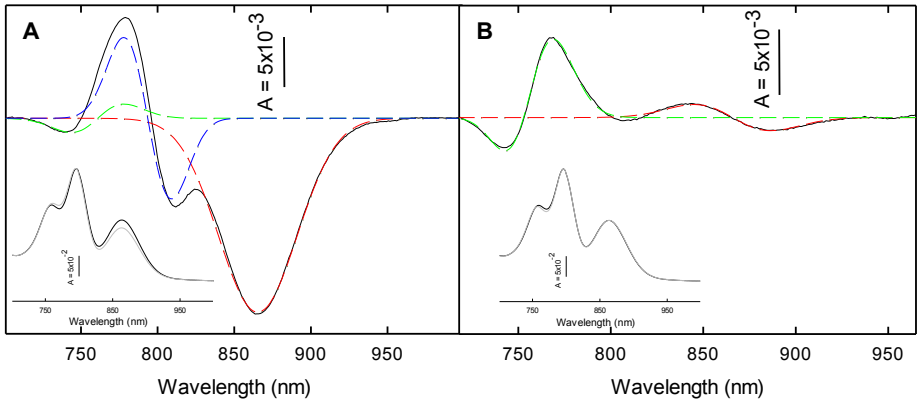

Figure 1.12 Decomposition of the near infra red (NIR) spectra during illumination. A. The NIR spectra of the BRC with no external electron donor. The presence of the P^+Q^- dipole causes a bathochromic shift on the pheophytins (green) and a hypsochromic shift on the monomers (blue). The shift on the monomer A is more pronounced than that of monomer B (not shown in figure). The absence of the P peak is observed by the bleaching of the 865 nm band (red). B. The near IR spectra of the RC in the presence of a secondary electron donor (cytochrome c_2 in this case). The oxidized P^+ state is continuously reduced to the P state. The presence of the Q^- charge causes a hypsochromic shift on the dimer (red) and a bathochromic shift on the pheophytins (green). The influence is different on the two pheophytins (not shown for clarity). The influence on the monomers in negligible because the Q^- lies perpendicular to the Q_Y moment of the monomers. The inserts represent the NIR spectrum of the BRC in the dark (black trace) and light (gray trace).

The appearance and disappearance of certain species can also be monitored with absorption spectroscopy. The linear correlation between the intensity of an absorption peak and the concentration is given by the Beer-Lambert law (Equation 1.2).

$$A = c\varepsilon L \tag{1.2}$$

The intensity of the absorption of light at a certain wavelength (A) is the product of the concentration of that species (c), the extinction coefficient (ε) and the optical path length (L). Since the latter two remain constant throughout the reaction, the degree of absorption is correlated to the concentration of the species producing the absorption. The effect of continuous illumination on P can be determined by monitoring the absorption at 865 nm before, during and after an illumination (Fig. 1.13). Before illumination, there is no change in the absorption of the dimer. Promptly after the light is turned on (Fig. 1.13 red trace) the absorption at 865 nm drops

as the P^+ state is formed. Continuous sub-saturating illumination causes the protein to go into the light-adapted conformational state which causes the signal to decrease further (blue trace). The fraction of the protein in the light-adapted state increases at a slower rate. After light is turned off, a fraction of the protein that is in the dark-adapted state recovers instantaneously (green trace). The fraction of the protein in the light-adapted conformation recovers at a slower pace (pink trace) due to the stabilizing effect of the conformational changes on P^+.

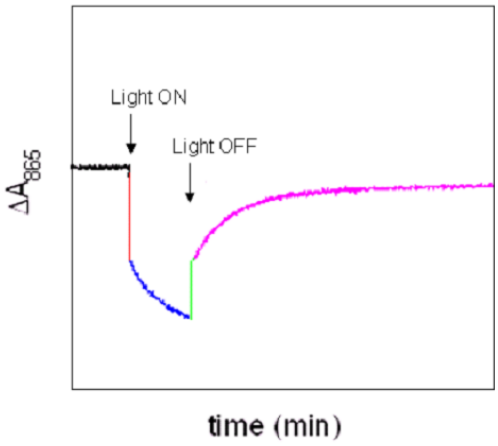

Figure 1.13 Identification of the different conformational states formed after the illumination. Multiple components were identified in the kinetic traces. The red component is representative of the sudden change due to the formation of charge-separated state in the dark-adapted conformation. The blue component decreases gradually as prolonged non-saturating illumination causes light-induced structural changes. After illumination is turned off, charge recombination from the dark-adapted conformation takes place very rapidly (~ 100 ms from Q_A and ~ 1 s from Q_B), which is represented by the green part of the trace. The fraction of P^+ that is recovering from the light-adapted state recovers on a longer time-scale (pink part of the trace). Charge-recombination kinetics can have multiple components related to different light-adapted conformational states, but only one component was shown for simplicity (pink trace).

1.6 Manganese coordination

Manganese is a transition metal with the $[Ar]4s^25d^5$ electronic configuration. Free-floating aqueous Mn is usually found in the divalent form (Mn^{2+}). However, Mn has seven possible

oxidation states (from Mn^0 to Mn^{7+}) and it can accept or donate an electron and go between adjacent oxidation states. The electron transfer between manganese species and other redox active molecules partly depends on the value of the Gibbs free energy. The Gibbs free energy (equation 1.3) represents the product of the number of electrons (n), Faraday's constant (F) and the difference in oxidation/reduction potentials between the acceptor and the donor. A negative Gibbs free energy implies then the reaction will happen spontaneously. A necessary rule for the electron transfer between two species to take place spontaneously is a higher electrochemical potential of the acceptor than the donor.

$$\Delta G = -nF\left(E_{acceptor} - E_{donor}\right) \tag{1.3}$$

Water coordinates Mn^{2+} in the *hexa-aquo* complex involving six symmetrically arranged water molecules as ligands forming a perfect octaheder around the Mn^{2+} ion. Any ligand replacement will distort this highly symmetrical complex reducing the stability of the Mn^{2+} state (Fig. 1.14 A). The charge-dipole interactions between the ligands and the core are strong and the energy required to add an extra charge is high (hence the high Mn^{2+}/Mn^{3+} potential of 1.2 V [11]). Coordinating with a negatively charged ligand provides a favorable Coulombic interaction, which stabilizes the cluster and lowers its oxidation/reduction potential. Bicarbonate $(HCO_3)^-$ ions have been used as ligands to Mn^{2+} (Fig. 1.14 B) [11,37]. Coordination with one bicarbonate reduces the potential by ~300 mV, and with two bicarbonate reduces it further by another 300 mV.

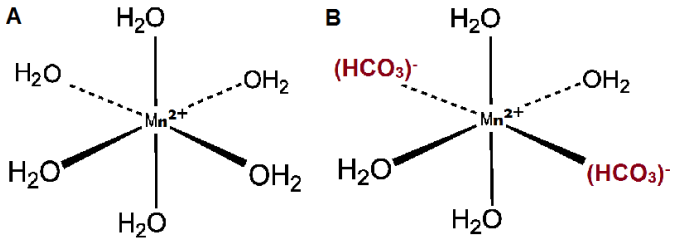

Figure 1.14 Manganese coordination complexes. A. The *hexa-aquo* manganese complex. Six water molecules are arranged in an octahedral geometry around the Mn^{2+} core. B. The bicarbonate *tetra-aquo* coordination complex. Two water molecules have been replaced by bicarbonate ions.

A commonly used pH buffer, bis-tris propane (BTP) has also been shown to coordinate manganese ions in synthesized clusters [38]. BTP is an organic molecule with six hydroxyl groups and two secondary amine groups placed symmetrically (Fig. 1.15). The amine groups can lose their protons at higher pHs but due to the close proximity of these two amine groups within the molecule the charge-charge interaction is strong between them. Thus, BTP has two pK_a values: 6.5 and 9.0 [39,40]. Below pH 6.5, both amines are protonated; between pH 6.5 and 9.0, one amine group is protonated and above pH 9.0 both groups are deprotonated. Amine and hydroxyl groups have been shown to coordinate Mn^{2+} in manganese synthesized complexes, polymers and even metalloproteins [41,42,43]. Crystal structures of the Mn-BTP cluster have been reported to contain both Mn^{2+} and Mn^{3+} species in a configuration of a trimer of dimers coordinated by the OH and NH groups of BTP [38]. The presence of the Mn^{3+} state in the crystals indicates a low potential of one pair of manganese that may be generated by auto-oxidation.

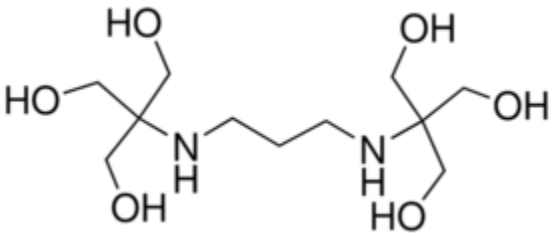

Figure 1.15. The structure of BTP. There are two secondary amine and six hydroxyl groups present in the molecule. The pK_as of the amine groups in solution are 6.8 and 9.0.

Apart from its presence in the OEC, manganese is a cofactor found in different metalloproteins. Proteins such as superoxide dismutase, ribonucleotide reductase and pseudocatalases require low potential manganese clusters in order to catalyze reactions [42,44]. Amino acid residues provide the octahedral geometry needed to coordinate manganese. The coordination and the lower dielectric constant in the core of the protein reduces the electrochemical potential of Mn^{2+} significantly (as low as 300 mV in superoxide dismutase) [42,45]. The optimal coordination also reduces the energy gap between the energy levels of different *d* orbitals, allowing for lower energy electronic transitions and subsequently spectroscopic signatures in the UV and even visible range (Fig. 1.16).

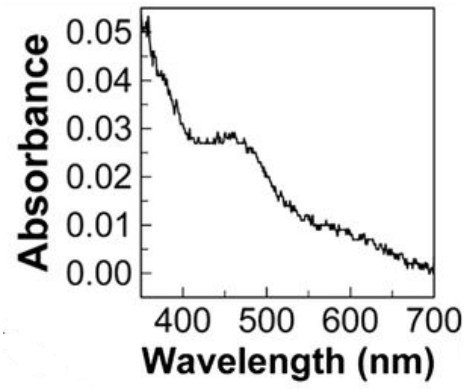

Figure 1.16 Optical spectrum of Mn-superoxide dismutase. The coordination of manganese by the residues of superoxide dismutase allows for the appearance of spectroscopic signatures in the visible and UV range. The optical spectrum of Mn^{2+} in water has no spectroscopic signatures. Figure taken from [46].

1.7 Relevant studies on the influence of Mn^{2+} on the dimer of the BRC

The influence of Mn^{2+} on BRCs has been studied extensively. The association of low potential bicarbonate coordinated manganese complexes on the native BRCs of *Rb. sphaeroides* has been examined [47,48]. Bicarbonate to manganese complexes in a ratio of 2:1 (Fig.1.10 B) have been shown to increase the recovery rate of the P^+Q^- state after saturating illumination [48]. The oxidation/reduction potential for these complexes has been reported as 520 mV at high concentrations of bicarbonate. However, with no elevation of the redox potential of the P/P^+ (505 mV in the dark-adapted state [14]), rapid electron donation from Mn^{2+} to P^+ was not observed.

The influence of bicarbonate manganese complexes was also studied in mutant BRCs. The mutations involved substituting neutral amino acids with positively charged residues in the vicinity of the BChl dimer [37,49]. The electrostatic influence from the nearby charges destabilized the formation of the oxidized dimer (P^+) and increased its potential to as high as 765 mV (Fig. 1.17 B). Bicarbonate complexes were also formed in order to reduce the potential of the Mn^{2+}/Mn^{3+} couple. Under these conditions, manganese oxidation by bacterial reaction centers was observed with a maximum rate constant of 30 s^{-1} in a diffusion-limited process. In a continuation of the study, a binding site for Mn was genetically designed in the vicinity of the dimer. Electron donation from manganese was observed with a first-order rate constant of 90 s^{-1}, showing that manganese binding to the designed pocket occurred. In total, six mutations are necessary for manganese binding and oxidation [49].

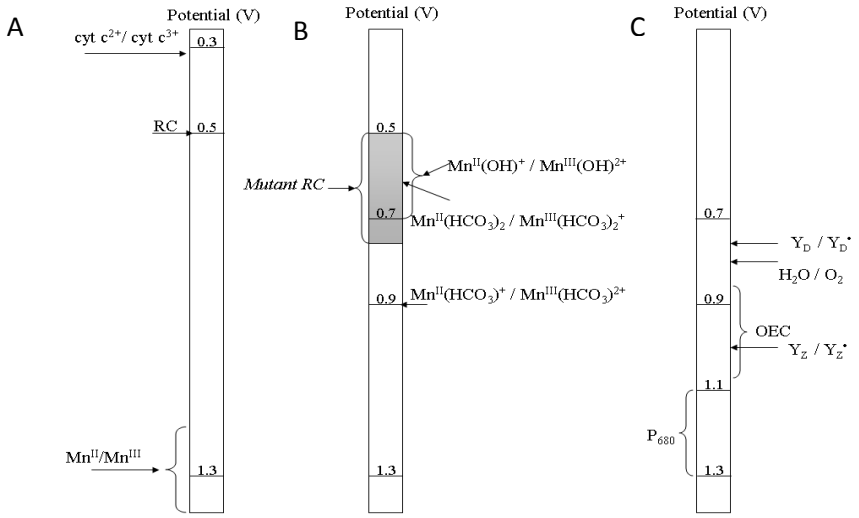

Figure 1.17 Bar diagram of the oxidation-reduction potential of (A) wild type BRC, (B) mutant BRC and (C) PS II. (A) The redox potential of the P/P^+ (0.5 mV), cyt c^{2+}/cyt c^{3+} (~0.32 mV) and *hexa-aquo* Mn^{2+}/Mn^{3+} (1.3 V). (B) The redox potential of mutant BRCs can increase due to different charges or hydrogen bonding near the dimer. In this case, mutations of neutral residues to charged amino acids increased the potential of the dimer to as high as 765 mV . The potential of the Mn was reduced by association with 1 HCO_3^- (900 mV) and 2 HCO_3^- (600 mV). (C) The redox potential of the P_{680} dimer in PSII (1.2 V) allows it to be the strongest oxidant in nature. As such it extracts an electron from the OEC (875-1050 mV) with the help of the Y_Z tyrosine (1 V) and the Y_D tyrosine (0.75 V). The OEC uses water splitting to extract up to four electrons. The potential of the H_2O/O_2 couple is ~800 mV.

The interaction between BRCs and manganese in BTP complexes was studied at pH 8 [50]. The presence of manganese caused the increase of potential of the dimer from 505 mV to 604 mV. Binding of Mn^{2+} was also identified to block the long-lived charge-separated states due to conformational changes after illumination and facilitate the rapid recovery of the P^+Q^- state. Molecular modeling has revealed two possible binding sites near the vicinity of P [50]. Although an interaction between Mn^{2+} and the BRC near the dimer has been shown at pH 8, secondary electron donation from Mn^{2+} was not observed in this instance.

1.9 Research perspective

The incorporation of Mn^{2+} ions into the structure of primitive RCs is the evolutionary milestone that led to oxygenic photosynthesis [11] and understanding this event can lead to major developments in artificial photosynthesis. Any evolutionary transition, however, is due to a triggering event, most likely the result of an environmental change that alters the relationship between the species involved. It is unknown exactly what redox interaction existed between ancient anoxygenic photosynthetic organisms and Mn^{2+} ions present in the environment ~2.8 billion years ago. One possibility is the use of the Mn^{2+} ions for secondary electron donation to the photo-oxidized chlorophylls, a similar role to that of Mn ions in the OEC of PS II. The ability of Mn^{2+} ions to act as a secondary electron donor to mutant BRCs has already been tested [37,49]. The oxidation/reduction potential of P was increased by mutations of nearby amino-acids, while the potential of Mn^{2+} ions in solution was reduced with bicarbonate coordination, making the electron transfer possible. Although mutations were a necessary part of the evolutionary transition to oxygenic photosynthesis, before they could be naturally selected for, the favorable association between Mn^{2+} ions and anoxygenic RCs should have already been established. Studies attempting to recreate electron donation from Mn^{2+} in native BRCs have already been conducted with Mn^{2+}-bicarbonate coordination [48,47]. Although promising, the results of these studies are not conclusive and the rate of electron transfer was very slow indicating energetically unfavorable conditions.

A different type of coordination could enable Mn^{2+} to act as an efficient secondary electron donor to the oxidized dimer. Following previous studies conducted by my colleague, Dr.

Deshmukh, the commonly used pH buffer, BTP, could provide such a coordination. The current work focuses on Mn^{2+} coordinated by BTP at pH 9.4 and the association between the coordinated complex and the BRC. The pH was selected such that the BTP is fully deprotonated, allowing for increased electrostatic attraction between the BTP ligand and the Mn^{2+} ions.

In these conditions, secondary electron donation from Mn^{2+} to P^{+} has been observed for the first time in native BRCs. Kinetic analysis was used to find the characteristics of the electron transfer process and develop a possible reaction mechanism. The influence of factors such as Mn^{2+} concentration, BTP concentration or pH was studied in order to understand the role of Mn^{2+}-BTP coordination on the electron transfer rate. The coordination complex was analyzed spectroscopically and electrochemically in the absence of BRC and structural characteristics were inferred based on available studies. Due to the charges on the species involved in the electron transfer, the electrostatic interaction between the Mn^{2+} ions and the BRC cofactors was analyzed in order to determine potential binding sites on the BRC surface. A competitive environment between Mn^{2+} and cyt c_2^{2+} was created in order to determine the secondary electron donor preference of the dimer. This could provide insight into the evolutionary mechanism that ultimately led to oxygenic photosynthetic organisms and might eventually assist in developing artificial photosynthetic energy conversion as a viable energy source.

Materials and methods

2.1 Growth of photosynthetic bacterium, *Rb. sphaeroides*

The growth of the cells and purification of the BRCs from carotenoid-less mutant R-26 and wild-type (WT) of *Rb. sphaeroides* were done following the protocol outlined by Feher and Okamura [53]. The steps involved were preparing and sterilizing media, inoculating cells and then photosynthetically growing bacteria. The growth media was prepared with 4 g of casamino acid, 4 mL of growth factor (vitamin solution), 80 mL concentrated base, 40 mL potassium succinate solution, 80 mL phosphate buffer at a 1 M concentration, and 25 mL of ammonium sulfate solution. A final volume of 4 L was obtained and the solution was autoclaved for 1 hour, in Pyrex glass bottles, in a SV-12 scientific pre-vacuum sterilizer. Following cooling to room temperature, the inoculations were performed by adding previously stored culture to the prepared media. To avoid contamination, all inoculations were done near a Bunsen burner.

Preparation of the vitamin solution involved mixing 2 mg of biotin with 50 mg of sodium bicarbonate, 100 g of nicotinic acid, 50 mg of thiamine-hydrochloride, and 100 mg and p-amino benzoic acid. The solution was boiled in order to dissolve the solutes. After boiling, the volume was adjusted to 100 mL and the solution was autoclaved for an hour. It was then cooled to room temperature.

Preparation of the concentrated base involved mixing 12 g of potassium hydroxide and 20 g of nitrilotriacetic acid. After 20 minutes of stirring, the supernatant was taken. Following this, 58 g of magnesium sulfate heptahydrate, 6.8 g of calcium chloride dehydrate, 200 mg of ferrous sulfate heptahydrate, and 4 mL of ammonium molibdenate were combined in solution. Each

separate component was dissolved before being added to the solution. The above solution was slowly added to the supernatant in 1 mL portions. Lastly, "metals 44" solution was added, the pH was adjusted to approximately 6.7 and the final volume was brought to 2 L.

The "metals 44" solution is a combination of 200 mg of ethylenediaminetetraacetic acid (EDTA), 1.1 g of zinc sulfate heptahydrate, 500 mg of ferrous iron sulfate heptahydrate, 150 mg of manganous sulfate monohydrate, 40 mg of cupric sulfate pentahydrate, 20 mg cobalt chloride, 12 mg boric acid, and 150 µL of 6 N sulfuric acid, all adjusted to a final volume of 100 mL. The solution is green at the start and then turns to amber.

The potassium succinate solution, at a 20% concentration, was made with 250 mL water and 200 g succinic acid poured into the same beaker. Although stirred, the solution did not fully dissolve yet. In a separate beaker, 200 g of potassium hydroxide was dissolved, cooled, and then slowly added to the succinic acid beaker. This step was performed with both beakers in an ice bath. Addition of HCl brought the pH to 7.0 and the final volume was adjusted to 1 L.

The phosphate buffer (1 M) was made through addition of 274 g dibasic potassium phosphate trihydrate to 1200 mL distilled water and then slowly combining that solution with a solution formed by dissolving 136 g monobasic potassium phosphate in 800 mL distilled water. The final volume was adjusted to 2 L with a final pH of 7.0.

The ammonium sulfate solution, at a 10% concentrate, involved dissolving 50 g of ammonium sulfate in 500 mL of water. The final pH was adjusted to 7.0.

Distilled water was used in the preparation of all solutions. Each solution was stored at 4 °C.

The media used for inoculation was placed in the dark for a maximum of 6 hours so that it could consume oxygen. *Rb. sphaeroides* was grown in the presence of light for two days, under anaerobic conditions. A set of 6 tungsten light bulbs with 60 W power each was used to provide

the wide spectrum illumination from visible to near infrared. Once the bacteria were fully grown they were placed in a Beckman J2-HS centrifuge at 4 °C with generating force of 7000 g for 20 minutes with a JA-10 rotor. After discarding the supernatant, the cells were collected and stored at 20 °C [53].

2.2 BRC purification

Following the aforementioned growth procedure, the BRCs were purified and dispersed in lauryldimethylamine-oxide (LDAO) detergent micelles according to a previous procedure [54,55,56]. For 1 hour, 100 g of collected cells, 200 ml of distilled water and 2 ml of 1 M Tris buffer were stirred in order to obtain a homogenized dispersion. Added to the mixture were 2 ml of EDTA, 1.25 g of sodium chloride (NaCl) salt and 1.7 ml of LDAO detergent. The NaCl salt is needed for obtaining the proper ionic strength that is needed to screen unfavourable electrostatic interactions.

A Mandel Scientific ultrasound processor (Model XL2020, Farmingdale, New York, USA) was used to break the cells. Sonication was done in an ice bath in order to avoid excessive temperatures. After 40 minutes of pulsed sonication in 10 s intervals, the cells were lysed.

The final volume of the solution, adjusted to 210 ml, was separated into 8 tubes. These were centrifuged in a Beckman Optima XL-100K ultracentrifuge (Fullerton, California, USA) with a Ti-70 fixed angle titanium rotor by generating force of 200 000 g at 4 °C for 2 hours. Following the primary centrifugation, the pellets were re-suspended in 205 ml of TEN buffer made from 15 mM Tris-HCl, 1 mM EDTA and 0.1 M NaCl. In the dark, 4.66 ml of LDAO was added and left to stir for 10 minutes at room temperature. This solution was centrifuged, identically to the first,

in order to solubilize BRCs in detergent micelles. The crude BRCs, dispersed in the detergent, were collected from the supernatant. Pellets containing membranes were discarded. For each 220 ml of supernatant, 72 g of ammonium sulfate and 7.3 ml of 30% LDAO were used in order to precipitate the crude BRCs. The mixture was stirred for 15 minutes at room temperature. The crude BRCs were then centrifuged by generating force of 10 000 g at 4 °C for 15 minutes in the Beckman J2-HS centrifuge with a JA-17 rotor type. These were finally re-suspended in TEN buffer and dialysed overnight in order to remove ammonium sulfate. The dialysing solution was $TL^{0.1}E$, which is 15 mM Tris-HCl mixed with 0.1% LDAO and 1 mM EDTA. For reconstitution of the Q_B site, 30 μM UQ-10 was added in the dialysis bag.

Further purification of BRCs was done by diethylaminoethyl (DEAE) ion exchange column chromatography. A Toyopearl 650 M beads were loaded to the column that was equilibrated using excess $TL^{0.1}E$ buffer. The protein was then loaded onto the column and remained bound to the column material. Using $TL^{0.1}E$, the column material was washed until free pigments stopped coming out of the column. The optical spectrum of the elute was recorded at 10 minute intervals, in a 260 to 1000 nm range, in order to determine when free pigment was coming out. To separate the purified BRC from other proteins and associated pigments, a linear salt gradient was created from 0.03 to 0.25 M NaCl in $TL^{0.1}E$ buffer.. This process enables a fine separation of the BRC from the LH1 antenna complex that surrounds the BRC *in vivo*.

The column was cleaned with 1 M NaCl to remove any bound materials. To verify the purity of the BRC protein, the ratio of absorbances at 280 nm and 800 nm was taken (A_{280}/A_{800}). A ratio of 1.2 is representative of the purest protein because aromatic amino acids have absorbance at 280 nm, which is 1.2 times that of bacteriochlorophyll monomers at 800 nm. The ratio was kept below 1.6. A ratio of 1:2:1 for the amplitude of absorption bands of bacteriochlorophyll dimer,

bacteriochlorophyll monomer and bacteriopheophytins is required. Excess salt from the BRC protein is removed through dialysis against salt-free $TL^{0.1}$ buffer once the column chromatography is completed. EDTA is not used in the dialysis solution as it will interfere in the measurements involving manganese. Dialysis was done at 4 °C, in the dark, with dialysis membranes with a molecular weight cut off (MWCO) of 12-14 kDa. For Q_B site reconstitution, 30 μM UQ-10 was added in the dialysis bag.

In order to further concentrate the BRC proteins dispersed in detergent micelles, ultra filtration was done using Millipore membranes with a nominal molecular weight limit (NMWL) of 30 kDa, under nitrogen pressure. The concentration of BRC protein was verified through optical spectroscopy by determining the absorption of the bacteriochlorophyll monomer at ~800 nm. The bacteriochlorophyll monomer band has an extinction coefficient of 288 $mM^{-1}cm^{-1}$ [57]. The purified protein was stored in the dark at -80 °C. Purified BRC can be dispersed into different detergent micelles by following the aforementioned column chromatography steps with $TX^{0.1}E$ buffer (15 mM Tris-HCl, X:TX-100, DOC, or CTAB and 1 mM EDTA) at an appropriate concentration with the detergent. The detergent concentration is above the critical micelle concentration (c.m.c.). For Q_A active samples, terbutryn, which is a potent inhibitor, was added in a concentration of 100 μM to block the electron transfer from Q_A^- to Q_B [58]. Sigma-Aldrich supplied all the chemicals used.

2.3 Sample preparation

In order to determine the optimum pH and concentrations of BTP and Mn^{2+}, spectroscopic titrations were performed. Titrations for the determining the optimum pH involved 15 mM bis-

tris propane and Mn^{2+} concentrations varying from 0.1 to 1000 mM. The titrations were performed at pH values ranging between 7.0 and 9.4. For the determination of the optimum concentration of BTP, Mn^{2+} concentration titrations were performed at pH 9.4. The Mn^{2+} concentration was varied from 0.01 mM to 30 mM. Titrations were performed at 5 mM, 15mM, 50 mM, 80 mM and 100 mM BTP.

Spectroscopic measurements involving the BRCs were conducted with 1 μM of the RC in 80 mM BTP and 0.1% LDAO detergent at pH 8 or 9.4. A fresh solution of 1 M Mn^{2+} in BTP was prepared an hour, at most, before the measurements were performed. Mn^{2+} dissolved in BTP solution was added last and at least 30 minutes of waiting time were required before measurements were taken. The waiting time is necessary for the complex to properly form.

2.4 Biophysical characterization

2.4.1 Steady-state absorption spectroscopy

A Cary 5000 UV-VIS-NIR spectrophotometer from Agilent (formerly Varian, Mulgrave, Victoria, Australia) was used to measure light-induced electron donation and charge recombination. To create light-induced states, a continuous wave excitation was achieved by using a 250 W tungsten lamp source (Oriel 6129) and the illumination was delivered to the samples through fiber optics (Newport Corp., Irvine, California, USA). Using the power supply (AMETEK, Sorensen, DCS33-33E, San Diego, California, USA), different light intensities, with powers from 40 to 250 W, were applied. Samples were prepared under weak green light and were dark-adapted inside the spectrometer for approximately 30 minutes before exposure to illumination of any sort. Measurements were performed in 4 ml quartz cuvettes under the

following conditions: wavelength ranges of 700-1000 nm or 1000-200 nm; data averaging time between datapoints was 0.033 s; spectral resoulution was set to 0.5 nm; the maximum scan rate of ~900 nm/min was selected; spectral bandwidth was 2 nm. The baseline was collected before measurement of spectra and, for light-minus-dark difference spectra, the baseline was taken with the BRC sample in the dark-adapted state. A series of spectra were recorded during and after the prolonged non-saturating illumination with 1 minute intervals up to 5 minutes and then with 5 minute intervals until full recovery. The spectra were recorded each minute during illumination.

In the kinetic mode of the spectrophotometer, absorption changes at a single wavelength were monitored as a function of time. Kinetic traces were analyzed by using a Levenberg-Marquardt algorithm, which decomposed them into exponentials.

2.4.2 Single flash excitation spectroscopy

For single flash experiments, a SIGMA EF-530 DG SUPER PA-PTTL electronic flash was used. The flash was powered by four type AA alkaline batteries with a recycling time at full charge of 6s. The flash duration was approximately 1.4 ms. The light-intensity was varied until full saturation of the light-induced signals at 1 μM BRC concentration was achieved. In these experiments the CARY 5000 spectrophotometer was used exclusively in kinetic mode. The data interval was set to 0.033 s. For studies involving the P/P^+ couple, a 865 nm wavelength was used with a 750 nm band pass filter; studies involving Q/Q^- were conducted at 760 nm with a band pass filter centered at 850 nm; the *cyt* c^{2+}*/cyt* c^{3+} couple was investigated at 550 nm with the 850 nm band-pass filter. At the selected wavelengths the optical transitions have significant differences between their corresponding reduced and oxidized forms and thus, are indicative of

the redox changes. With the interference filter the light excitation can be narrowed to a ±20 nm range around the specified wavelength, reducing the amount of stray light reaching the detector. In some experiments only single flash excitation could be used requiring a high-signal-to-noise ratio. Our spectrometer provides a remarkable noise level of $\sim 10^{-4}$ absorption units, allowing us to observe and analyse weak signals with high accuracy. The trade-off for the exceptional signal-to-noise, however, was the time resolution of only 33 ms.

For Q_B active samples, Q_B reconstituted BRCs were used and 30μM UQ-10 was added to the sample. For Q_A active samples 100 μM terbutryn was added.

The kinetic decomposition of the traces was done using a Levenberg-Marquardt algorithm..

2.4.3 Spectroelectrochemical redox titrations

The oxidation-reduction midpoint potential of the Mn-BTP complex and of the P/P^+ couple was determined by using spectroelectrochemical oxidation-reduction titration. The samples were placed into a spectroelectrochemical redox cell of local design [15,16]. The ambient redox potential was adjusted with a CV-27 potentiostat, supplied by Bioanalytical Systems (West Lafayette, Indiana, USA). The measuring electrode was 333 lines/in. gold mesh (Precision Eforming, Cortland, New York, USA) similar to a previous mentioned system [59]. For reference electrode, a miniature calomel electrode (Cole Palmer, Vernon Hills, Illinois, USA) was used. The calibration of this instrument was done according to O'Reilly [60]. Potassium hexacyanoferrate-(II) and potassium tetracyanomono(1,10-phenanthroline)ferrate-(II) at a 300 μM concentration were added to act as redox mediators. The Cary 5000 spectrophotometer was used to monitor the changes in absorption spectra with applied potentials [61]. For the Mn-BTP

complex, the difference between the spectrum at the respective potential and the spectrum at no applied potential was obtained and the amplitude of the highest peak (shifting from 252 nm to 267 nm) was recorded. For the P/P^+ potential, the degree of electrochemical oxidation was determined by measuring the amplitude of the Q_Y dimer band at 865 nm with respect to the applied potential [15,16]. For samples involving BRCs, the ionic detergent, LDAO, was replaced with a non-ionic detergent, Triton X-100 (TX-100), by ion exchange chromatography [59]. The BRCs for the electrochemical titrations were concentrated to approximately 200 μM and kept, regardless of pH values, in 0.1% TX-100 and 80 mM BTP. All measurements were taken at room temperature.

Certain experiments involved continuous illumination of the sample in the electrochemical cell. The light intensity was kept at a value corresponding to a power of 125 W angled at approximately 45° with respect to the propagation of the monitoring beam to avoid stray light entering the detector.

2.5 Data analysis

2.5.1 Analysis of the kinetic traces

Kinetic traces, recorded with absorption spectroscopy under continuous or short flash illumination, have characteristic of the various recoveries of the dimer from the oxidized state through either electron donation or charge recombination. The latter can occur at different rates characteristic of the various conformational sub-states of the protein. Decomposition of the kinetic traces into exponentials was done assuming from one to three kinetic components. One

component was fitted to recovery rates after flash illumination in Q_A active samples or for the changes during continuous illumination. Three components were used to approximate the recovery in Q_B active samples. The decomposition was done according to the following equation:

$$A(t) = Be^{-k_1 t} + Ce^{-k_2 t} + De^{-k_3 t} \quad (2.1)$$

Where,

A(t): amplitude of P band at 865 nm at any time t

B, C, and *D*: amplitudes of the decaying kinetic components

t: time

k_1, k_2, and k_3: rate constants of the decaying kinetic components

The lifetime (τ) of the charge-separated state was determined as the inverse of the respective kinetic rate constant (k).

2.5.2 Analysis of metal binding

The dissociation constant for the metal binding study was determined based on a binding model for high concentrations of Mn^{2+} [37]. Kinetic traces in the presence of different concentrations of metal ion were analyzed according to equation 2.1 and the dissociation constant of metal binding was determined through the following equation:

$$R_M = \frac{A}{1+\frac{K_D}{[Mn^{2+}]}} \quad (2.2)$$

Where,

R_M: fraction of the kinetic component

$[Mn^{2+}]$: manganese concentration

A: amplitude of the fraction

K_D: dissociation constant

In the case where the kinetic component decreased with increasing $[Mn^{2+}]$, the binding equation was:

$$R_M = A\left(1 - \frac{1}{1+\frac{K_D}{[Mn^{2+}]}}\right) \quad (2.3)$$

2.5.3 Decomposition of absorption spectrum into individual components

The bands of the NIR spectrum of the BRC were fit to Gaussian equations for the bacteriochlorophyll dimer and bacteriopheophytin, or by the sum of multiple Gaussians for the bacteriochlorophyll monomers (B_L and B_M). The single Gaussian equation is:

$$A = a \times \mathrm{e}^{-0.5\left(\frac{\lambda-\lambda_0}{b}\right)^2} \quad (2.4)$$

where,

A: absorbance at a given wavelength

a: peak absorbance

λ: wavelength

λ_0: peak position on wavelength scale

b: bandwidth at half maxima (BWHM)

2.5.4 Determination of the midpoint potential

The Nernst equation was used to fit the data of the fraction of the reduced species as a function of the applied potential. The data were fit with a one-electron Nernst equation. One component was necessary for the P/P^+ dark potential and for the in-situ Mn^{2+}/Mn^{3+} potential [59]. The Nernst equation is defined as:

$$E_i = E_m + \frac{RT}{nF} ln \frac{O_i}{R_i} \quad (2.5)$$

where,

E_i: applied potential

E_m: midpoint potential

R: universal gas constant; R=8.314 $JK^{-1}mol^{-1}$

T: absolute temperature

n: number of electrons

F: Faraday constant; F=9.648 × 10^4Cmol^{-1}

O_i: fraction oxidized at the applied potential

R_i: fraction reduced at the applied potential

A three component Nernst equation was used for the potential of the different Mn^{2+}/Mn^{3+} coordination in the BTP complex. In this case, no less than three components were necessary to fit the span of the data on the potential scale.

2.5.5 Determination of proton dissociation constant

The pH dependencies of the manganese oxidation were fitted with a Henderson-Hasselbach equation (2.6). The fit yielded the apparent pK_a of the protonatable amine residues of the BTP that are associated with the Mn ions as ligands.

$$f(H) = \frac{1}{1+10^{(pH-pK_a)}} \tag{2.6}$$

where,

$f(H)$: fraction protonated

pK_a: acid dissociation constant for protonatable residues

The Henderson-Hasselbach equation was extended to the involvement of two protonatable residues based on a model previously presented [62]:

$$f(H) = \frac{1}{1+10^{(pH-pK_a)}+\left[10^{(pH-pK_a)}\right]^2} \quad (2.7)$$

2.5.6. Determination of the rates of consecutive reactions

The rates of the dimer recoveries due to Mn^{2+} oxidation in the two states of the conformationally-gated mechanism have been determined using a previously adopted model for consecutive reactions [63]:

$$[P^+_{861} - Mn^{2+}] = \frac{k_1}{k_2-k_1} \times (e^{-k_1 t} - e^{-k_2 t})[P^+_{865} - Mn^{2+}]_0 \quad (2.8)$$

where,

$[P^+_{861} - Mn^{2+}]$ is the concentration of the conformationally altered P^+

k_1 and k_2 are the rates of the two reactions

$[P^+_{865} - Mn^{2+}]_0$ is the initial concentration of the P^+ in the original conformation

Results

3.1 Electron donation to the oxidized dimer by BTP-coordinated Mn^{2+}

Manganese ions acting as efficient secondary electron donors to native BRCs have not been observed so far primarily due to two major reasons: i) their oxidation potentials are much higher than the most oxidizing cofactor (P^+) in BRC making the electron transfer from Mn^{2+} thermodynamically unfavorable; ii) the time window available to the electron transfer to take place determined by the lifetimes of the charge separated states is too short. In this work we attempt to address and optimize both factors in order to utilize manganese ions as electron donors.

3.1.1 Secondary electron donation from Mn^{2+} during continuous illumination

Using continuous illumination addresses the second obstacle (ii) mentioned above, namely allows the charge separated states to exist in forms that have longer lifetimes. Illumination generates the light-induced charge separation in the BRC that results in the P^+Q^- state. In every single turnover a small percentage (< 5%) of the protein undergoes conformational changes that induces the formation of long-lived charge-separated states. Due to their low quantum yields in a single turnover experiment (using a short flash as an excitation source) they cannot be detected with confidence. Under continuous illumination these light-induced conformational states can be

accumulated as they have lifetimes from seconds to tens of minutes at room temperature depending on the specific conditions [13,14,15,62]. These conditions are thus advantageous to observe slow electron transfer reactions e.g. possible electron donation from the Mn^{2+}. Such reactions would not be possible to detect during the short lifetime of the charge-separated state in the dark-adapted conformation. Earlier studies conducted at pH 8 did not yield electron donation but did show an association between Mn^{2+} and the native BRC [50]. On the other hand, in previous studies of Mn^{2+} oxidation in mutant BRCs, increasing pH resulted in secondary electron donation from Mn^{2+} that was not observed at lower pH values [37]. These earlier observations gave us hints to extend our investigations to higher pH values, where not only the coordination of Mn^{2+} changes but also the increasing number of negative charges due to the deprotonation of amino acid side chains decreases the redox potential of Mn^{2+}/Mn^{3+} redox couple.

The light-minus-dark spectrum in the NIR range was recorded after 1 minute illumination, with and without added Mn^{2+} that was coordinated by BTP. In the absence of Mn^{2+}, the spectrum is representative of the P^+Q^- state (Fig. 3.1 A black trace). In the presence of 5 mM Mn^{2+}, the spectrum lacks all the spectroscopic features characteristic to the oxidized dimer: the bleaching of the dimer band centered around 865 nm and the electrochromic shift on the bacteriochlorophyll monomers around 800 nm. Instead the spectrum is representative of the PQ^- state featuring only the electrochromic shift on the bacteriopheophytins (Fig. 3.1 A pink trace). Similar spectral signatures are obtained with other secondary electron donors like cytochrome c_2^{2+} (Fig. 3.1 A brown trace) and ferrocene (Fig. 3.1 A olive trace). The presence of the PQ^- state is the sign of secondary electron donation to the dimer. This electron would be provided by the oxidation of Mn^{2+} to Mn^{3+}.

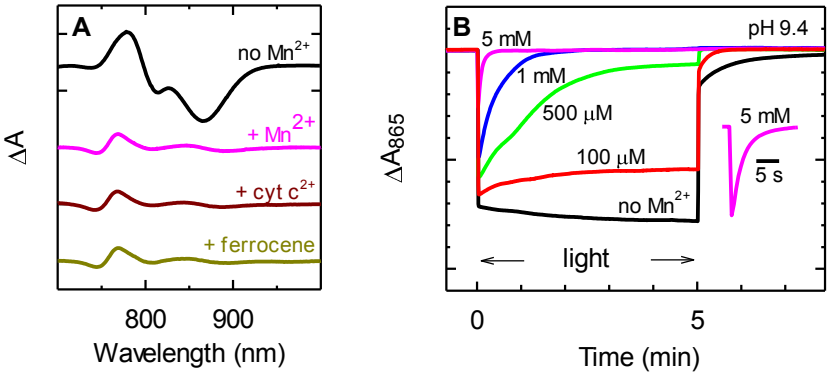

Figure 3.1 Spectral evidence of Mn^{2+} electron donation to the oxidized dimer. A. Light-minus-dark spectra with and without secondary electron donors. The light-minus-dark spectra were taken 1 minute into the illumination. The spectrum without Mn^{2+} shows features characteristic to the P^+Q^- charge-separated state (black), while the spectrum with Mn^{2+} shows features characteristic to the PQ^- state (pink). Similar spectra were recorded with other secondary electron donors, such as cyt c^{2+} (brown) and ferrocene (olive). B. Influence of Mn^{2+} on the kinetics of the formation and disappearance of the oxidized dimer during continuous illumination. The amount of P^+ is monitored through the absorbance change at 865 nm. As the light is turned on (time = 0 s) P is oxidized instantly. Without Mn^{2+}, long-lived charge-separated states are formed during illumination, which results in a slow decrease in the absorbance at 865 nm. At low Mn^{2+} concentrations (100 μM), the long-lived charge-separated states are blocked and a very small amount of P^+ recovers during illumination. As Mn^{2+} concentration increases, there is more evidence of the reduction of P^+. The rate constant of recovery in 5 mM Mn^{2+} (pink trace) has been measured to be 0.192 s^{-1}, resulting in a lifetime of 5.20 ± 0.05 s for the P^+ state. The conditions were: 1 μM RC in 0.1% LDAO and 80 mM BTP at pH 9.4. Mn^{2+} was added at the respective concentrations. In the respective studies, cyt c^{2+} and ferrocene concentrations were 10 μM and 250 μM, respectively.

By monitoring the amplitude of the dimer absorbance peak at 865 nm we can analyze the kinetics of formation and disappearance of P^+ during and after illumination at different concentrations of Mn^{2+} (Fig. 3.1 B). The initial light excitation immediately oxidizes P, forming P^+. Spectroscopically, the formation of P^+ is characterized by a bleaching of the dimer band at 865 nm, resulting in a decrease in absorption at that wavelength. In the absence of Mn^{2+}, under subsaturating illumination, the protein undergoes conformational changes that results in an increase in absorbance at 865 nm (Fig. 3.1 B black trace). At 100 μM of Mn^{2+}, these conformations are blocked and the P^+ recovers, to some extent, even during illumination. As Mn^{2+} concentration increases further, it becomes more evident that P^+ is reduced to P. This is due

to an electron donation from Mn^{2+} to P^+, eventually forming P and Mn^{3+} according to the following scheme:

$$PQ + Mn^{2+} \xrightleftharpoons{hv} P^+Q^- + Mn^{2+} \xrightarrow{e^-} PQ^- + Mn^{3+} \longrightarrow PQ + Mn^{3+}$$

Scheme 3.1 Simplified mechanism of electron donation from Mn^{2+} to P^+ under continuous illumination. Light induces the P^+Q^- charge-separated state which can recombine back to the original state or the P^+ can accept an electron from an external Mn^{2+} forming PQ^- and Mn^{3+}. The charged quinone can slowly find an electron acceptor in the environment, reverting back to the PQ state. Illumination will continuously consume the PQ state, while electron transfer will consume the P^+Q^- state, leaving only the PQ^- state detectable.

The presence of the PQ^- state and the disappearance of the P^+Q^- state during illumination indicate the first observation of Mn^{2+} acting as a secondary electron donor to the oxidized dimer in native BRCs. The rate of electron donation increased with Mn^{2+} concentration, while the amount of P^+ formed initially (at time = 0) decreased. At 5 mM Mn^{2+}, the electron is donated with a rate of ~0.192 s^{-1}, resulting in a lifetime of 5.20 ± 0.05 s (Fig. 3.1 B pink trace). Under these conditions, initial P^+ concentration (when the light is turned on), is only ~25% of the concentration without Mn^{2+}. This indicates that there must be a faster phase of the electron donation from Mn^{2+} to the oxidized dimer that could not been observed at the time resolution used here and that the Mn^{2+} oxidation by P^+ must have two different mechanisms..

In order to understand the electron donation process, the rates were plotted with respect to varying Mn^{2+} concentration. At lower concentrations (below 1 mM Mn^{2+}) the rate of electron donation was slow. The maximum concentration of Mn^{2+} used was 30 mM as at higher concentrations the optical quality of the sample suffered. In Figure 3.2 B, there is a linear relationship between the rates before saturation (below 5 mM) and the concentration of added Mn^{2+}. This relationship indicates a second-order diffusion-limited process and its measured rate constant is 4×10^2 $M^{-1}s^{-1}$.

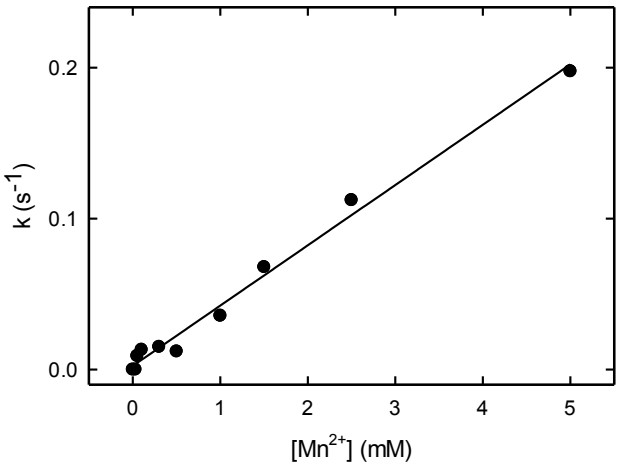

Figure 3.2. Change in rate of electron donation with respect to Mn^{2+} concentration. The rate of secondary electron donation from Mn^{2+} to P^+ is plotted with respect to the concentration. The linear dependence of electron donation rate on Mn^{2+} concentration indicates a diffusion-limited process. The second order rate constant is determined to be 4×10^2 $M^{-1}s^{-1}$. Representative traces are presented in Fig. 3.1 B.

3.1.2 Mn^{2+} electron donation to the oxidized dimer after single flash excitation

In order for an electron donor to be considered efficient, the process must occur within the lifetime of the P^+Q^- charge-separated state. To test the effectiveness of Mn^{2+} as a secondary electron donor, the dimer was excited by using a saturating single flash. In order to assess the efficiency of electron donation, two types of charge recombination were chosen: $P^+Q_A^- \rightarrow PQ_A$ and $P^+Q_B^- \rightarrow PQ_B$. Under typical experimental conditions (pH 8, 15 mM Tris, 0.1% LDAO) the time constants of these reactions are 100 ms and 1 s, respectively [65]. Recovery from $P^+Q_A^-$ is achieved by using the inhibitor terbutryn to block the electron transfer from Q_A^- to Q_B [58]. Recovery from $P^+Q_B^-$ is achieved by reconstituting the Q_B binding site in the protein (see Materials and Methods). Briefly, ubiquinone was added to reach 30 μM concentration after the

extraction and purification steps, as well as in the final sample, in order to ensure saturation of the Q_B binding site.

The flash-induced kinetics of both the $P^+Q_A^- \rightarrow PQ_A$ and $P^+Q_B^- \rightarrow PQ_B$ charge recombinations were recorded at different Mn^{2+} concentrations. Every trace was measured at least four times in the same conditions, with representative traces shown in Figure 3.3. The instantaneous flash immediately oxidizes P, resulting in a decrease of absorbance in the dimer band at 865 nm. The recovery kinetics were found to be highly dependent upon the occupancy of the Q_B binding site and the presence or absence of Mn^{2+}. The kinetic traces were decomposed into exponentials according to Eq. 2.1 depending on whether Q_A or Q_B active samples were used.

The time constant of the $P^+Q_A^- \rightarrow PQ_A$ charge recombination at pH 9.4 in the presence of 80 mM BTP was 122 ± 3 s. The presence of Mn^{2+} at high concentrations (over 5 mM) decreased the recovery time constant to 86 ± 4 ms. This increase in the rate can be caused by two factors: i.) the presence of the Mn^{2+} ions in the vicinity of P^+ that would electrostatically destabilize the $P^+Q_A^-$ state and/or ii.) a rapid electron donation from Mn^{2+} to P^+ that can compete with the $P^+Q_A^- \rightarrow PQ_A$ charge recombination. Given the small increase (only 1.4-fold) in the rate constant in the presence of manganese we cannot distinguish between the two possible processes (Fig. 3.3 A). The rate of $P^+Q_B^- \rightarrow PQ_B$ charge recombination, on the other hand, is about 5-fold lower, 650 ± 10 ms at pH 9.4 and thus could be utilized to identify which of the two above mechanisms is responsible for the acceleration of P^+ recovery. In Q_B active samples, where the reconstitution of the Q_B binding site is ~90% even without added Mn^{2+} the recovery was found to be complex (Figs 3.3 B and 3.4). As the reconstitution of the Q_B binding site can never be achieved at 100 % efficiency it is expected that a small fraction (<10 %) of the BRCs are found in the $P^+Q_A^-$ state, while the vast majority of the BRCs, which have active Q_B are in the $P^+Q_B^-$ state. The longer

lifetime of the charge separated state also allows slower conformational changes to take place in a small population of the BRCs. The three recovery processes result in complex kinetics with three components (see also Fig 3.4) corresponding to the three above mentioned populations of the BRCs. Upon Mn^{2+} addition the recovery kinetics accelerated markedly as the concentration of Mn^{2+} increased to an observed lifetime of 83 ± 4 ms. Such a dramatic acceleration (nearly 8-fold) cannot be explained by simple Coulomb interactions. Thus, we attributed it mainly to the electron donation from Mn^{2+} to P^+ (Fig. 3.3 B). Decomposition of the observed kinetic traces to exponentials according to Eq. 2.1 yielded the rate constants and the amplitudes of the corresponding kinetic components that are plotted as a function of the applied Mn^{2+} concentration in Figure 3.4.

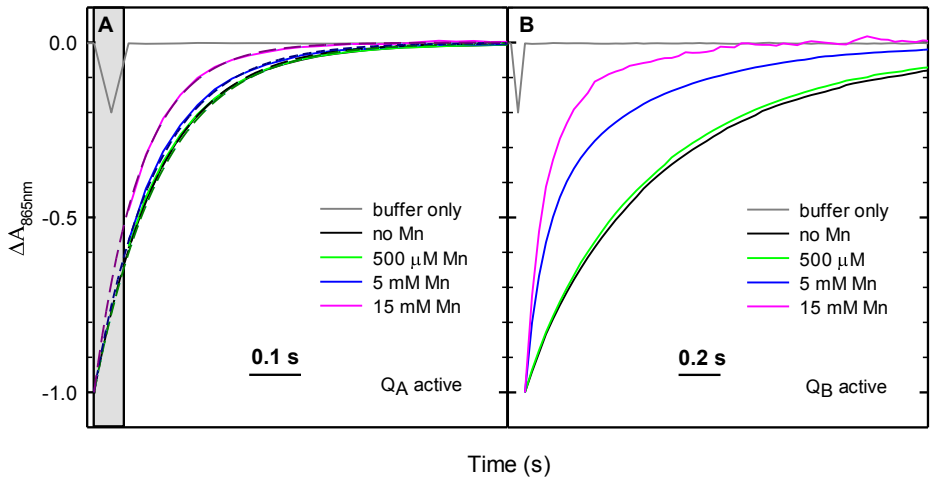

Figure 3.3 Recoveries of the oxidized dimer after single flash excitation. A. Recovery of the $P^+Q_A^-$ state with increasing Mn^{2+} concentration in Q_A active samples. The data immediately after the flash is fired is lost due to the slow acquisition rate of the equipment (gray rectangle). The gray trace represents the spike generated by the flash. The fits to the recoveries are represented with dashed lines and are extended to the start of the flash. Without Mn^{2+} (black trace), the $P^+Q_A^- \rightarrow PQ_A$ lifetime is measured at 122 ± 3 ms. With increasing Mn^{2+} concentration, the lifetime decreases to ~86 ± 4 ms. B. Recovery of the P^+Q^- state with increasing Mn^{2+} concentration in Q_B active samples. Without Mn^{2+}, (black trace) the lifetime of the P^+ is measured at ~650 ± 10 ms. With Mn^{2+}, the lifetime drops significantly to ~ 83 ± 4 ms. Same conditions as Figure 3.1 except with 100 μM terbutryn for Q_A active samples and 30 μM ubiquinone for Q_B active samples.

In Q_A active samples, the recovery without added Mn^{2+} was monophasic, corresponding to the $P^+Q_A^- \rightarrow PQ_A$ charge recombination (Fig. 3.4 open circles). In Q_B active samples without Mn^{2+} the recovery was more complex, consisting of three kinetic phases: a fast (black circles), a slow (blue circles) and a very slow component (green circles). At these concentrations, the fast component is attributed to the $P^+Q_A^- \rightarrow PQ_A$ charge recombination, the slow component to the $P^+Q_B^- \rightarrow PQ_B$ charge recombination and the third, marginal, very slow component to a $P^+Q^- \rightarrow$ PQ recovery in a different, light-induced conformation.

The most significant change with increasing Mn^{2+} concentration is the increase in the amplitude of the fast component and the coupled decrease in the amplitude of the slow component in Q_B active samples. Equations 2.2 and 2.3 were used to quantify the change in the amplitudes with respect to the concentration of Mn^{2+}. The dissociation constants, K_D between the Mn^{2+} and the BRC were found to be 6.4 ± 0.5 mM and 6.5 ± 0.5 mM from both amplitudes (from fits represented by solid lines in Fig. 3.4 B). The agreement in dissociation constant between the two processes suggests that there must be a single site where the Mn^{2+} is donating electron from.

From the above analysis we can conclude that the measured lifetime of 83 ± 4 ms in the presence of high concentration of Mn^{2+} can mainly be attributed to the intrinsic electron donation from Mn^{2+} to P^+ which competes with the normal charge recombination from the $P^+Q_A^-$ state, which has a lifetime of ~122 ± 3 ms. The electron transfer lifetime of 5.2 s determined under continuous illumination would be characteristic of the diffusion of Mn^{2+} inside the binding pocket.

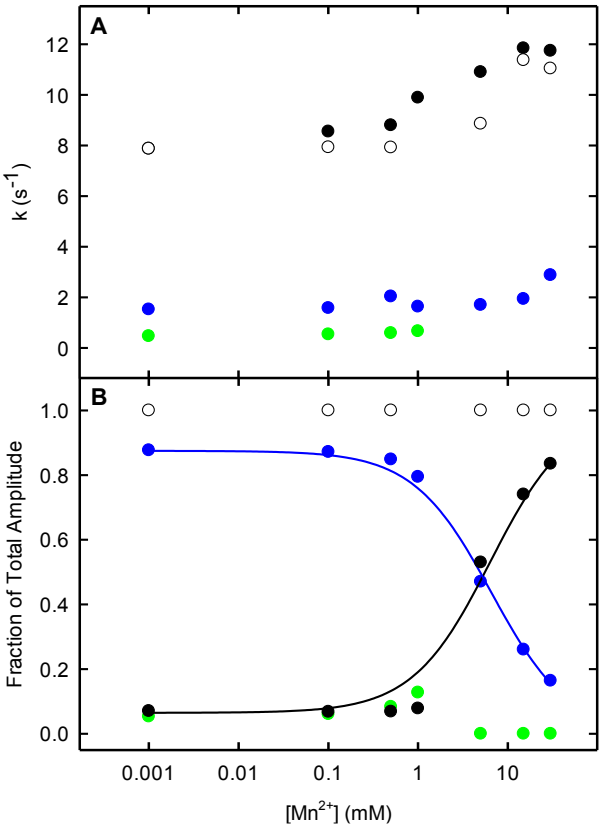

Figure 3.4 Kinetic parameters of the P^+Q^- recovery after single flash excitation in Q_A and Q_B active samples. After the flash was fired, the P^+Q^- state recovered with a single component in Q_A active samples and a complex multiphasic recovery in Q_B active samples. Open circles represent kinetic parameters (rate constants and fraction of total amplitude) acquired in Q_A active samples, while closed circles represent kinetic parameters acquired in Q_B active samples. Black circles are use to label the fastest components (representing the $P^+Q_A^- \rightarrow PQ_A$ charge recombination at lower $[Mn^{2+}]$ and $P^+Q^- + Mn^{2+} \rightarrow PQ^- + Mn^{3+}$ electron transfer at higher $[Mn^{2+}]$), blue circles are used to label the slow component ($P^+Q_B^- \rightarrow PQ_B$ charge recombination) and green circles are used to label the very slow component ($P^+Q^- \rightarrow PQ$ charge recombination from light-induced conformations). A. Rate constants as a function of Mn^{2+} concentration. The rate constant of the fast component increases slightly with Mn^{2+} concentration with a corresponding time constant decrease from 122 ± 3 ms to 83 ± 4 ms, while the rate constants of both the slow and very slow components stayed fairly similar throughout the measurements. The very slow component disappeared at higher Mn^{2+} concentrations. B. Fraction of total amplitude with respect to Mn^{2+} concentration. In Q_B active samples, the fraction of the fast component increases with Mn^{2+} concentration, while the fraction of the slow component decreases with Mn^{2+} concentration. Eq. 2.2 and 2.3 were used to fit he respective changes (solid lines) and binding constants of 6.5 ± 0.5 mM and 6.4 ± 0.5 mM were determined. Representative traces in Fig. 3.3.

3.1.3 Multiple flash excitation analysis on the reduction of P^+ by Mn^{2+}

The ~60-fold difference in the observed kinetics for electron donation from Mn^{2+} to P^+ using continuous illumination (Fig. 3.1 B) or single flash excitation (Fig. 3.3) clearly suggest two different mechanisms under different conditions. The faster process observed in Fig. 3.3 suggests a rapid, first-order kinetics from a bound Mn^{2+}, while the slower process (Fig. 3.1 B) can be attributed to a second-order reaction, where the electron donation is limited by the slow diffusion of the Mn^{2+} to and from the vicinity of P. The huge gap between the single flash and continuous illumination was bridged with an experiment where trains of flashes were used with rapid succession (Fig. 3.5 A). The absorbance changes at 865 nm, at the center of the dimer band were monitored in the presence of Mn^{2+}. Two separate experiments were conducted involving a series of up to 49 consecutive flashes fired within 10 seconds, in a sample containing 1 μM Q_B active BRC, 5 mM Mn^{2+}, and 80 mM BTP. Interference filters were not used to ensure saturating illumination.

The kinetics of the absorbance changes at 865 nm were dependent upon the number of flashes fired and the envelope of the individual flash-kinetic responses resembled the signal obtained in the same conditions under continuous illumination (Fig. 3.5 A, insert, red trace). As opposed to the kinetic trace recorded under continuous illumination, the signal after multiple flashes did not recover fully, but reached saturation before 10 s had passed. The recovery after the first flash closely resembled the kinetic trace that was obtained in a single flash experiment using 5 mM Mn^{2+} (Fig. 3.5 A pink trace and blue trace in Fig. 3.3 B). The trace after the 49^{th} flash, however, was found significantly longer and resembled the trace that was obtained without added Mn^{2+} in

a single flash experiment (green trace in Fig. 3.5 A and black trace in Fig. 3.3 B). This indicates that once the signal reaches saturation, Mn^{2+} electron donation is no longer observed after subsequent flash excitations.

The concentration of P^+ detected after each flash also decreased with time and concomitantly with the amount of flashes fired (Fig. 3.5 B). The small interval between flashes (~0.20 s) did not allow the electron to return from Q^- to P^+ in all BRCs. The decrease in the initial amplitude was attributed to the slow, diffusion limited electron transfer from Mn^{2+} to P^+. The signal also reached a plateau similarly to the overall kinetic trace (Fig. 3.5 B and Fig. 3.5 A, insert, black trace). The incomplete recovery of the signal can be attributed to the existence of two populations of BRC. Since the concentration of Mn^{2+} present is approximately equivalent to the determined K_D, half of the population will have Mn^{2+} bound and half will not have Mn^{2+}. Thus Mn^{2+} electron donation to P^+ only occurs in half of the population, while the other half recovers via charge recombination. Diffusion-limited Mn^{2+} oxidation followed by subsequent illuminations eventually generated a state of the BRC whose response to flash excitation was beyond the detection limit of the equipment (see Scheme 4.1 and Section 4.2.4 in Discussion). Once saturation had been reached, only the population without Mn^{2+} was responsive to flash excitation and it recovered via charge recombination.

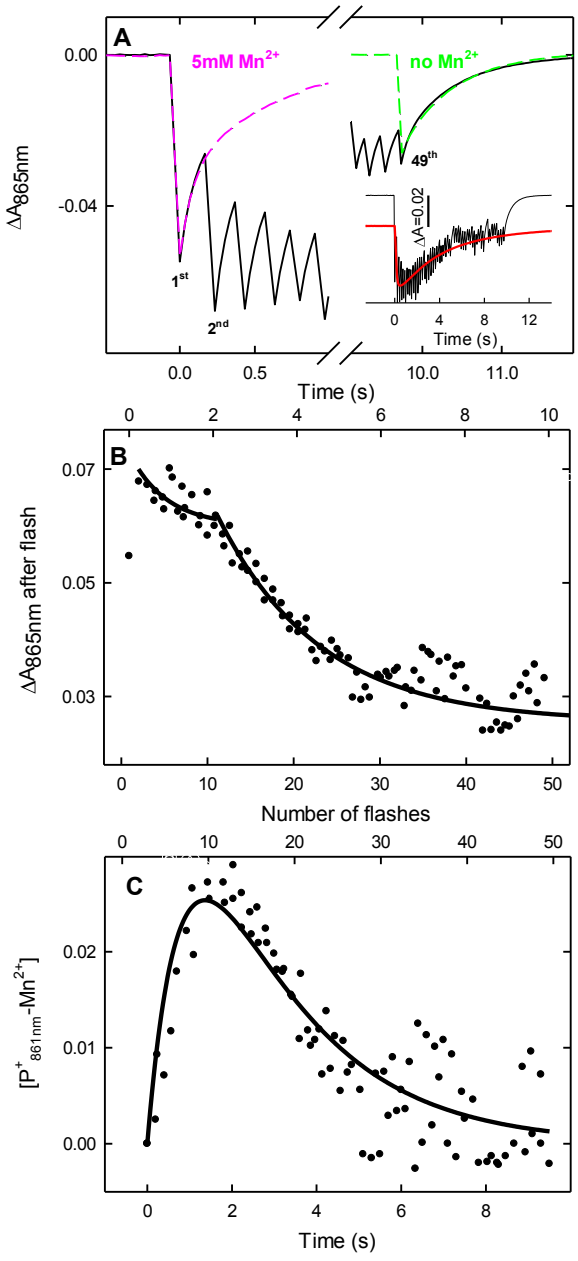

Figure 3.5 Recovery of P^+ during multiple flashes. A. The changes in the 865 nm P band were monitored as a series of 49 flashes was fired within 10 s. The small interval between flashes did not allow the full recovery of the P^+ state. The kinetic recovery during illumination (black trace) resembles the recovery during continuous illumination (red trace). The recovery reached saturation after ~50% of P^+ was recovered. The individual flash recoveries of the 1st and 49th trace resembled the recoveries after single flash excitation with 5 mM Mn^{2+} (pink trace) and no Mn^{2+} (green trace), respectively, presented in Fig. 3.3 B. B. The absorption immediately after each flash was recorded with respect to time and number of flashes fired. The results of two different experiments are analyzed in order to increase the quality of the fittings. C. The formation and disappearance of the conformationally-altered P_{861}–Mn^{2+} state. The decrease in amplitude was analyzed with a model of two consecutive reactions (Eq. 2.8) with time constants of τ_1 = 800 ± 100 ms and τ_2 = 2.4 ± 0.2 s. The first reaction corresponds to the photo-activated conformational change that allows Mn^{2+} to diffuse in the vicinity of the dimer, while the second reaction corresponds to the electron donation from diffusing Mn^{2+} ions. Solid lines were used to represent the fittings from the model in panels B and C. Conditions: 1 μM Q_B active BRC, 5 mM Mn^{2+}, 80 mM BTP, pH 9.4.

The analysis of the decrease of amplitude revealed that the slow oxidation is preceded by another process that slightly decreases the amplitude of the signal (Fig 5 B). We attribute this observation to a few nm blue-shift in the P band from 865 to 861 nm as the Mn^{2+} diffuses to the vicinity of P and establishes a Coulomb interaction with it (see later Fig. 3.11 insert). Once Mn^{2+} diffused to the vicinity of P, the electron donation will be feasible and the kinetics becomes similar to what we found using continuous illumination in the presence of Mn^{2+} (red trace in the insert of Fig. 5 A). We have established that the blue-shifted form of P is a marker of Mn^{2+} diffusion to the vicinity of P that in turn allows the electron transfer to happen. The diffusion of Mn^{2+} inside the binding pocket is an illumination-dependent process, probably associated with light-induced conformational changes occurring in the BRC. The formation and disappearance of the P_{861}^{+}-Mn^{2+} association is plotted as a function of time (and indirectly the number of flashes applied) and was fitted with a consecutive reaction model (Eq. 2.8 and Fig, 3.5 C). The time constant for the formation of the P_{861}^{+}-Mn^{2+} state was 850 ± 100 ms, while its disappearance due to the diffusion and subsequent oxidation of Mn^{2+} occurs with a time constant of 2.4 ± 0.2 s. The difference between the latter time constant and the one determined under continuous illumination (5.2 s) could be explained by the difference in conditions between the two experiments. The presence of a charged Q_B^{-} in the Q_B binding site in flash experiments could promote a favorable electrostatic interaction which would increase the diffusion time of Mn^{2+} into its pocket.

3.2 The effect of BTP coordinating ligand on the ability of Mn^{2+} to act as a secondary electron donor

For the first time, evidence has been presented that Mn^{2+} effectively reduces the oxidized dimer in native BRCs. Coordination of the Mn^{2+} ions by BTP molecules allows them to act as secondary electron donors. The influence of BTP concentration on the ability of Mn^{2+} to donate an electron to P^+ is investigated by kinetic analysis of the signal under continuous illumination. The light was kept on for 5 min in samples containing 1 μM RC and 5 mM Mn^{2+} at pH 9.4, each with different BTP concentrations. The absorption change was recorded as a function of time at 865 nm, at the center of the P band, during and after illumination (Fig. 3.6 A). Decreasing signal amplitudes during the illumination are the signatures of Mn^{2+} being utilized as secondary electron donor to P^+. Figure 3.6 A clearly shows that without added Mn^{2+} the signal amplitude did not decrease at all. The slow increase in the 5 minute illumination is in agreement with the accumulation of the long-lived charge-separated states. As Mn^{2+} was added in 5 mM concentration, the decrease of the P^+ signal during illumination was found strongly dependent on the BTP concentration. Using another pH buffer, CAPS that also have hydroxyl groups similar to BTP did not result in the decrease of the P^+ signal. This observation indicates that coordination by hydroxyl groups alone is most likely insufficient to reduce the potential of Mn^{2+} to the level that P^+ could accept an electron from it. As the BTP concentration was increased not only did the magnitude of the initial P^+ signal decrease, but also the rate of disappearance of P^+ increased. The maximum rate was achieved at 80 mM BTP concentration and all P^+ was reduced by Mn^{2+} in the first few seconds of the illumination (Fig. 3.6).

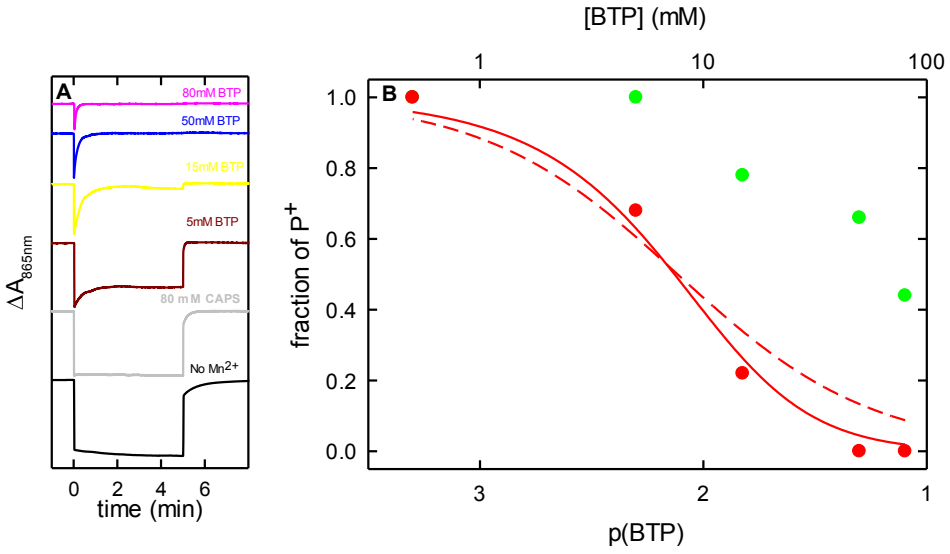

Figure 3.6 Effect of BTP concentration on the rate of Mn^{2+} oxidation by P^+. A. Absorbance changes measured at 865 nm during and after continuous illumination at different concentrations of BTP. Increasing BTP concentration increases the rate of P^+ reduction and the extent of Mn^{2+} oxidation. The maximum rate is observed at 80 mM BTP. Electron donation doesn't occur when replacing BTP with CAPS or without Mn^{2+}. B. Fraction of P^+ with respect to BTP concentration. The fraction of P^+ measured immediately after turning the light on (green circles) and at the maximum extent of oxidation (red circles) is plotted with respect to the negative logarithm of concentration of BTP (p(BTP)). The extent of oxidation increases with increasing BTP concentration. Models similar to the Henderson-Hasselbach equations, with p(BTP) instead of pH, were used to fit the data (Eq. 2.6 and 2.7). The fit with 1 BTP/Mn^{2+} ion is represented by a dashed line and the fit with 2 BTP/Mn^{2+} is represented by a solid line. The latter model provides a significantly better fit, indicating the presence of two coordinating BTP molecules per Mn^{2+} ion. All traces were gathered with 1 µM RC in 0.1% LDAO with 5 mM Mn^{2+} under 125W continuous illumination for 5 minutes

The extent of Mn^{2+} oxidation initially and at the end of illumination was recorded. These parameters were plotted with respect to the negative logarithm of the concentration of BTP, an analogous term to pH. (Fig. 3.6 B). A model using equations 2.6 and 2.7 was applied to the data to determine how many BTP molecules per Mn^{2+} are required to enable the Mn^{2+} to serve as a secondary electron donor to P^+. Equation 2.6 assumes only one BTP/Mn^{2+} and equation 2.7 accounts for two BTP/Mn^{2+} stoichiometry. Fitting our data with these two models clearly shows that the former model (dashed line in Fig. 3.6 B) is far less accurate than the latter (solid line in Fig.3.6 B). This suggests that the optimal stoichiometry is 2 BTP/Mn^{2+}.

3.3 Coordination of Mn^{2+} by BTP

3.3.1 Spectroscopic signatures of the Mn-BTP coordination complex

The complex formed through the coordination of Mn^{2+} by BTP is analyzed through optical spectroscopy in the visible and near UV range (Fig. 3.7). At low pH (blue trace), the spectrum lacks spectroscopic signatures and resembles the spectrum of Mn in the *hexa-aquo* coordination. At higher pH values, characteristic features emerge in the spectra (Fig. 3.7 pink and green traces). The appearance of spectroscopic signatures is partly related to the color of the solution. Just as with coordination by water molecules, in the presence of BTP at pH 6, dissolved $MnCl_2$ forms a colorless complex, most likely also coordinated by only water molecules, as indicated by the lack of spectroscopic signatures in the visible and UV ranges. The same solution of Mn^{2+} in BTP at pH values higher than 7 initially has a pink color. The color deepens as the the pH is increased.

The influence of the concentration of Mn^{2+} ions is displayed in Figure 3.7 (solid vs. dashed traces). The freshly made complexes of manganese formed at pH 8 and 9.4 have a strong absorption band between 230 and 250 nm and weaker bands at around 410 nm and in the 520-540 nm range. The exact position and amplitude of these peaks are influenced by both concentration and pH. The presence of spectroscopic signatures at pH 8 and 9.4 indicates that Mn^{2+} is no longer in the *hexa-aquo* coordination, rather it is also coordinated by BTP.

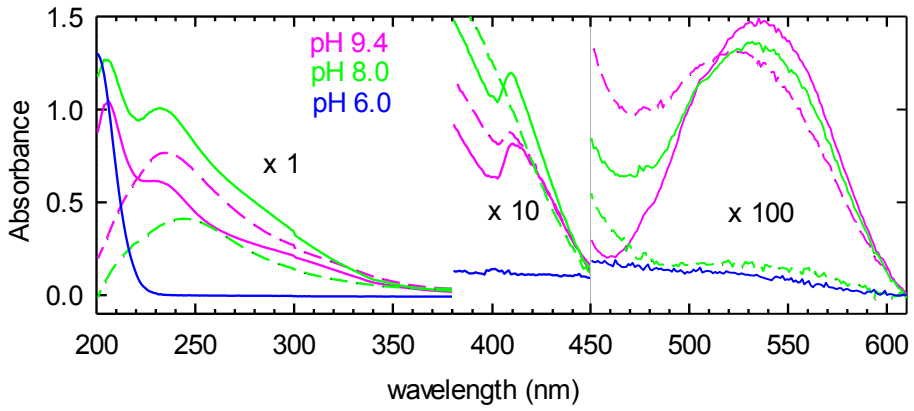

Figure 3.7 Spectra of the Mn-BTP complex at different pH values. The spectrum of 1 M (solid lines) and 100 mM (dashed lines) $MnCl_2$ in 80 mM BTP was taken from 200 nm to 600 nm. The spectra are shown at three pH values: 6 (blue), 8 (green) and 9.4 (pink). Certain features are cut or magnified for clarity. Features for the pink and green traces are: a 535 nm peak for 1 M concentration at both pH 8 and 9.4; a 525 nm peak for 100 mM at pH 9.4; a 410 nm shoulder for 1M pH 8 & 9.4 and 100 mM pH 9.4; a 245 nm peak for 100 mM at pH 8; a 236 nm peak for 1 M pH 8 & 9.4 and 100 mM pH 9.4; a 207 nm peak for 1M pH 8 & 9.4. There are no features for the complex at pH 6.

Time after dissolving the $MnCl_2$ in BTP was also a factor in the formation of the complex. Although the color of the Mn^{2+} and BTP solution was initially pink, the solution eventually turned brown. At pH 8 this transition occurred in over six hours, while at pH 9.4 the change in color was faster. Figure 3.8 shows the time dependent spectra of the Mn-BTP complex at pH 9.4 after Mn^{2+} is added. The spectra are shown as differences between the spectra recorded at the designated time and the initial spectrum recorded immediately after the $MnCl_2$ was dissolved. As time increases, there was also a slight increase in the amplitude of absorption and a shift in the peak. The peak position was found initially at 257 nm and after approximately 1 hour, the position of the peak settled at 268 nm. This shift may indicate a slow formation of a species in the solution and could be evidence of auto-oxidation of some Mn^{2+} to Mn^{3+}.

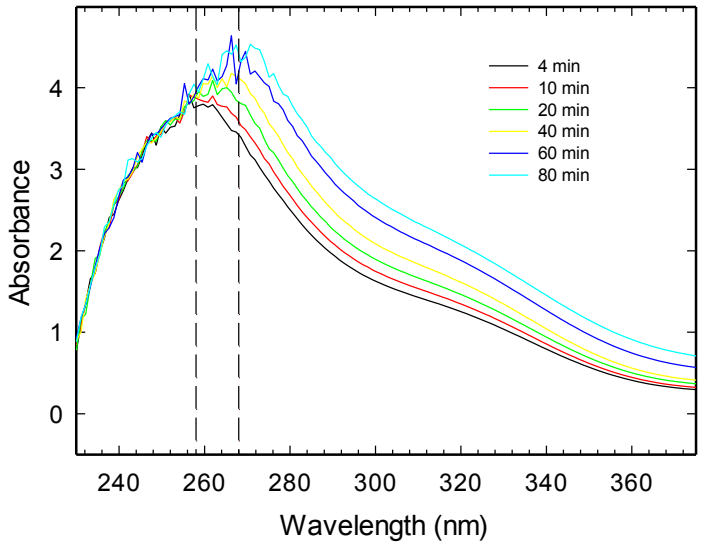

Figure 3.8 Time evolution of the spectra of the Mn-BTP complex. The spectra of 5 mM Mn in 80 mM BTP at pH 9.4 were taken at various times and the differences between the spectrum at the specific time and the spectrum at time zero (addition of Mn^{2+}) is presented in the figure. The peak originally at 257 nm increases, and shifts over time, to 268 nm.

3.3.2 The oxidation/reduction potential of the Mn^{2+}/Mn^{3+} couple in BTP coordinated complexes.

The ability of Mn^{2+} to act as a secondary electron donor to the oxidized dimer suggests the existence of a Mn^{2+} with lower potential than that of the dimer (505 mV in 15 mM Tris and 0.05% TX-100 detergent [15,16]). The possible auto-oxidation of Mn^{2+} to Mn^{3+} along with the existence of spectroscopic signatures in the near UV and visible range suggest that coordination with BTP reduces the potential of the Mn^{2+} from 1.2V observed in the *hexa-aquo* complex.

The oxidation/reduction potential of the Mn^{2+}/ Mn^{3+} redox couple in 80 mM BTP solution was determined by spectroelectrochemical redox titrations (Fig. 3.9). The titrations were conducted at

pH 8 (Fig. 3.9 B) and at pH 9.4 (Fig. 3.9 A), where the BTP exists in two different protonational states. The spectra were obtained as differences between the spectra at the respective potential and the spectrum without applied potential. The fraction of oxidized Mn^{3+} is plotted with respect to applied potential. The measurements were performed twice, both in the oxidative and in the reductive direction. The errors in the measured amplitudes were smaller than 2%.

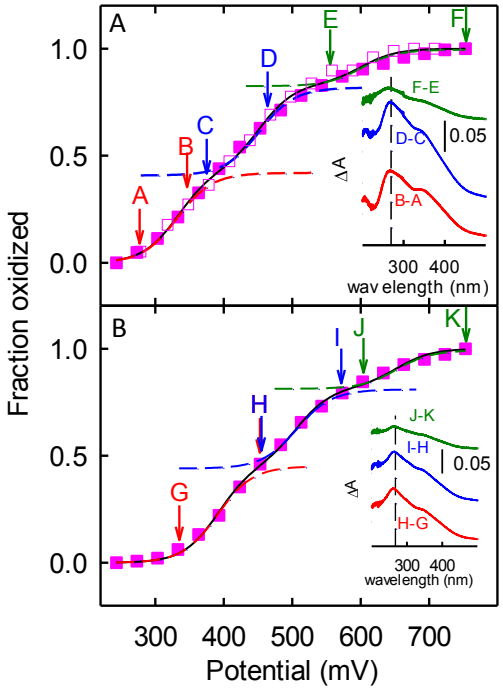

Figure 3.9 Electrochemical potential of the Mn-BTP complex. The fraction of Mn^{3+} oxidized is plotted against the applied potential at pH 9.4 (A) and pH 8 (B). The oxidized fraction is obtained as a ratio between the highest and lowest point of the peak varying from 255 nm to 267 nm. The titration for pH 9.4 was performed both in the oxidative (closed squares) and reductive (open squares) directions. The errors are smaller than 2% and graphically smaller than the selected symbol size. For each pH, a three component Nernst equation (derived from Eq. 2.5) was necessary to fit the data. The individual components are represented with dashed lines and their parameters are presented in Table 3.1. The inserts represent the difference spectrum between the fully reduced and fully oxidized states for each component. The change in the amplitude at 267 nm is represented with a dashed line. Conditions: 5 mM Mn^{2+} and 80 mM BTP.

Table 3.1 Parameters of the Nernst fit to the electrochemical titration of the Mn^{2+} coordinated by BTP

pH 9.4			pH 8		
E_m (mV)	A (%)	Closest integer	E_m (mV)	A (%)	Closest integer
332 ± 5	42 ± 2	2	391 ± 5	45 ± 2	2
452 ± 5	41 ± 3	2	507 ± 5	37 ± 2	2
601 ± 7	17 ± 1	1	652 ± 5	18 ± 2	1

The variation of the amplitude was fit with a three component Nernst equation (equation 6). The presence of all components was necessary to fit the entire range of the change in amplitude. The midpoint potential and the relative amplitude of each component for both pH values are listed in Table 3.1. The necessity of the three-component Nernst model indicates three different types of Mn^{2+} species in solution. The relative amplitudes indicate a ratio of 2:2:1 for the three types of Mn^{2+}, at both pH values (see table 3.1). Coordination by BTP reduces the potential of the Mn^{2+} to as low as 332 ± 5 mV and 396 ± 5 mV at pH 9.4 and pH 8, respectively. The potential of all three types of Mn^{2+} ions is increased by 49-53 mV at pH 8 compared to pH 9.4. This increase could indicate the participation of the protonatable amine groups of BTP in the coordination of the Mn^{2+} ions.

The position of the absorbance peak from 255 nm to 267 nm is also plotted with respect to applied potential (Fig. 3.10). As the change in potential influences the position of the peak, it provides an indication of the formation of an oxidized Mn^{3+} ion. A single component Nernst equation is used to fit the data and the midpoint potential is determined to be 336 ± 5 mV. This

suggests that the lowest potential Mn^{2+} at pH 9.4 is responsible for the peak shift. The oxidation potential determined from the peak shift in Fig. 3.10 was found to be the same within the experimental error as the lowest potential determined from the amplitudes of absorption changes in Fig. 3.9.

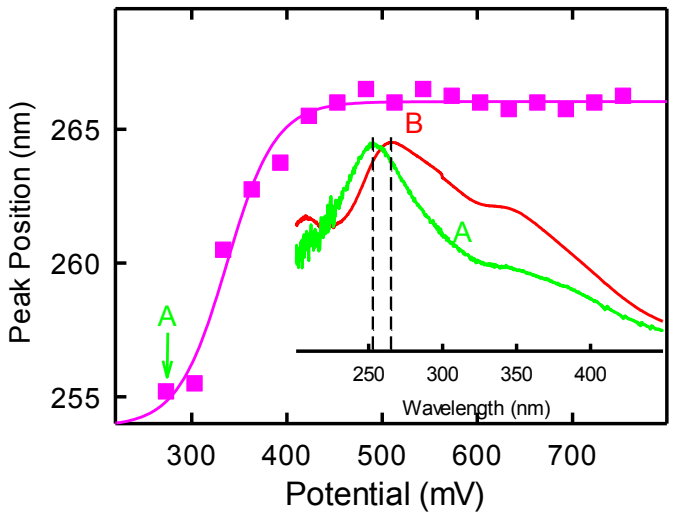

Figure 3.10 Correlation between the shift in the 252 nm peak and the lowest potential component. The position of the peak is plotted with respect to applied potential. The insert shows the normalized absorption spectra with the position of the peak varying from 255 nm to 267 nm. The midpoint potential is identified as 336 ± 5 mV. This correlates with the potential of the first component with 332 ± 5 mV. The shift in this peak correlates with that in Figure 3.8 and indicates that the lowest potential component undergoes auto-oxidation.

3.4 Interaction between Mn-BTP complex and the BRC

3.4.1 The *in situ* Mn^{2+}/Mn^{3+} potential

All three types of Mn^{2+} ions at pH 9.4 (Fig. 3.9, Table 3.1) have low enough potential to participate in electron donation to the oxidized dimer. In order to determine the identity of the electron donor among the three different kind of Mn^{2+} present in solution, a sample including

BRC in 200 μM concentration and 30 mM Mn^{2+} in 80 mM BTP was added to the electrochemical cell. As an external potential was applied to the sample, continuous illumination was used to monitor the ability of Mn^{2+} to reduce P^+. Illumination was on for 1 minute in order to allow enough time for the Mn^{2+} to reduce P^+. The light-minus-dark spectra were recorded and were analysed for signs of electron donation.

At potentials below 300 mV, the same spectra were recorded as shown in Figure 3.1 A without applied potential. These spectra are characteristic to the PQ^- state and clear indicators of electron donations from Mn^{2+} to P^+ (Fig. 3.11 blue trace). As the potential was further increased according to our conclusions from Figures 3.9 and 3.10, the lowest potential forms of Mn^{2+} in the cluster must be gradually oxidized. If this is the manganese species that donates the electron to P^+ then it will no longer be able to reduce P^+ and the recorded light-minus-dark difference spectra should retain the features of P^+ even at the end of the illumination. This is exactly what we have observed. At potentials over 400 mV the spectra recorded are characteristic to the P^+Q^- state (Fig. 3.11 red trace). This spectrum was recorded in Figure 3.1 A in the absence of Mn^{2+} and indicates that the lowest potential manganese must be the electron donor, which has been disabled by electrochemical oxidation. Intermediate potentials resulted in spectra characteristic to mixed-states, where both PQ^- and the P^+Q^- states are present to certain degrees (Fig. 3.11 green trace). The wavelength of the strongest positive absorption peak is monitored with respect to applied potential (Fig. 3.11 pink circles). For the PQ^- state, the maximum absorption in the light-minus-dark spectrum is at 768 nm, while for the P^+Q^- state, the maximum absorption peak is at 779 nm. For comparison purposes, the same analysis is applied to a sample without Mn^{2+} and no significant shift was observed with applied potential. A one component Nernst equation (Eq. 2.5) was satisfactory to fit the data and the midpoint potential of the *in situ* Mn^{2+} acting as

secondary electron donor is determined to be 349 ± 4 mV. The 17 mV increase of the manganese potential *in situ* as opposed to those determined in the free complex leads to the conclusion that the lowest potential Mn^{2+} ions in the cluster must be in an unfavorable electrostatic interaction (repulsion) with P. This interaction must also be mutual and therefore the redox potential of P is also expected to be elevated in the presence of Mn^{2+} (see section 3.4.2 below). The identity of the electron donating Mn^{2+} is in accordance with the observation that the ability of Mn^{2+} to act as a secondary electron donor to the oxidized dimer decreases with time. This is due to the auto-oxidation at ambient conditions of the lowest potential Mn^{2+}.

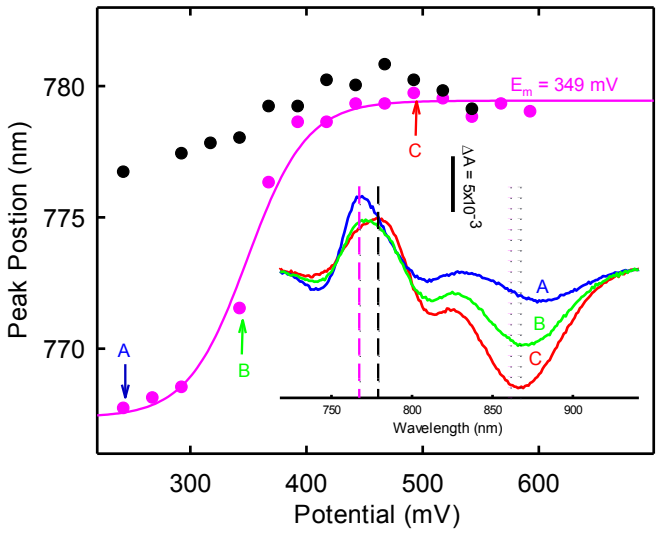

Figure 3.11 Potential of the *in situ* Mn^{2+}/Mn^{3+}. Electrochemical redox titrations under continuous illumination were done in order to determine the *in situ* potential of the Mn^{2+}. Light-minus-dark spectra are taken at various applied potentials. At lower potentials, the spectra are representative of the PQ^- state (blue trace), while above 443 mV the spectrum is characteristic of the P^+Q^- state (red trace). At intermediate potentials, the spectra are mixtures of the two states (green trace). The peak position with the highest absorbance is plotted against applied potential. For the PQ^- state, the absorption is at a maximum at 768 nm (pink dashed line), while for the P^+Q^- state, the absorption peaks at 779 nm (black dashed line). The change in wavelength is fit with a single component Nernst equation (Eq. 2.5) and the fit results in a midpoint potential of 349 ± 4 mV for the Mn^{2+}/Mn^{3+} donating the electron. The dotted line represents the position of the dimer absorption band in the presence of Mn^{2+}. The P band shifts from 865 nm (black dotted line) to 861 nm (pink dotted line) due to the diffusion of Mn^{2+} near P. Conditions: ~200 µM BRC in 0.05% TX-100, 80 mM BTP, 30 mM Mn^{2+} and 300 µM ferro/ferricyanide.

The blue trace in Figure 3.11 is representative of the PQ^- state in the presence of Mn^{2+}. The extent of the P blue-shift occurs between a minimum absorbance at 885 nm and a maximum absorbance at 837 nm. In the presence of other secondary electron donors such as cyt c^{2+} and ferrocene, the extent of the observed shift was between 888 nm and 840 nm (Fig. 3.1 A). The 4 nm difference indicates that the P absorption band is blue-shifted from 865 nm to 861 nm in the presence of Mn^{2+}, but not in the presence of other electron donors. The new position of the P absorption band is indicated by a dotted line in the insert of Figure 3.11. The P absorption band shift would be a consequence of the diffusion of the Mn^{2+} ions in the vicinity of P interacting with the electrons distributed over the conjugated part.

3.4.2 The effect of Mn^{2+} on the electrochemical potential of P/P^+

The ability of the Mn^{2+} in solution to act as a secondary electron donor to the dimer indicates an interaction between the Mn^{2+} and the BRC in the vicinity of the dimer. The interaction was investigated by determining the electrochemical potential of the P/P^+ dimer with and without Mn^{2+} both at pH 8 and pH 9.4. Following a redox titration, the amplitude of the dimer peak at 865 nm was plotted with respect to the applied potential. As the external electric field was applied, the amount of reduced P present depends on the strength of the field. The Nernst model (Eq. 2.5) was used in order to analyze the data.

Without Mn^{2+}, the potential of the dark-adapted dimer was determined to be 505 ± 5 mV and 501 ± 4 mV both in the reductive and oxidative directions for pH 8 and 9.4, respectively (Fig 3.16 A & B). This is in accordance with previously determined P/P^+ potentials in the dark [15,16]. At

pH 9.4, where electron donation occurs, the midpoint potential with Mn^{2+} was determined to be 555 ± 5 mV in the oxidative direction, which is 60 mV higher than the potential determined without Mn^{2+} (Fig. 3.12 D). At pH 8, the midpoint potential in the oxidative direction with Mn^{2+} was even higher, measuring 605 ± 5 mV (Fig. 3.12 C). As the electrochemical titration was performed in the reductive direction, the midpoint potential of the dimer in the presence of Mn^{2+} was measured at 510 ± 5 mV for pH 8 and 515 ± 5 mV for pH 9.4, reverting close to the original dark-adapted potential without Mn^{2+}. Generally, a hysteresis in redox titrations is representative of the reaction not reaching equilibrium. However, this would result in a change between oxidative and reductive directions of 5-20 mV [66]. The increase in potential in the oxidative direction (95 mV and 40 mV for pH 8 and pH 9.4, respectively) indicates the presence of Mn^{2+} in the vicinity of the dimer, and not lack of proper equilibration. The hysteresis between oxidative and reductive directions could indicate a slow diffusion of the Mn^{2+} ions in their fully reduced form near the dimer, followed by the subsequent repulsion of the oxidized Mn^{3+} by the positively charged P^{+}. Our data also suggests that the Mn^{3+} ions remain in the vicinity of P even after being oxidized and only the steady presence of P^{+} at high potentials repels them. The titrations were performed in the loop fashion namely oxidative, reductive and again in the oxidative direction to make sure the Mn ions diffuse back to the vicinity of P after its reduction.

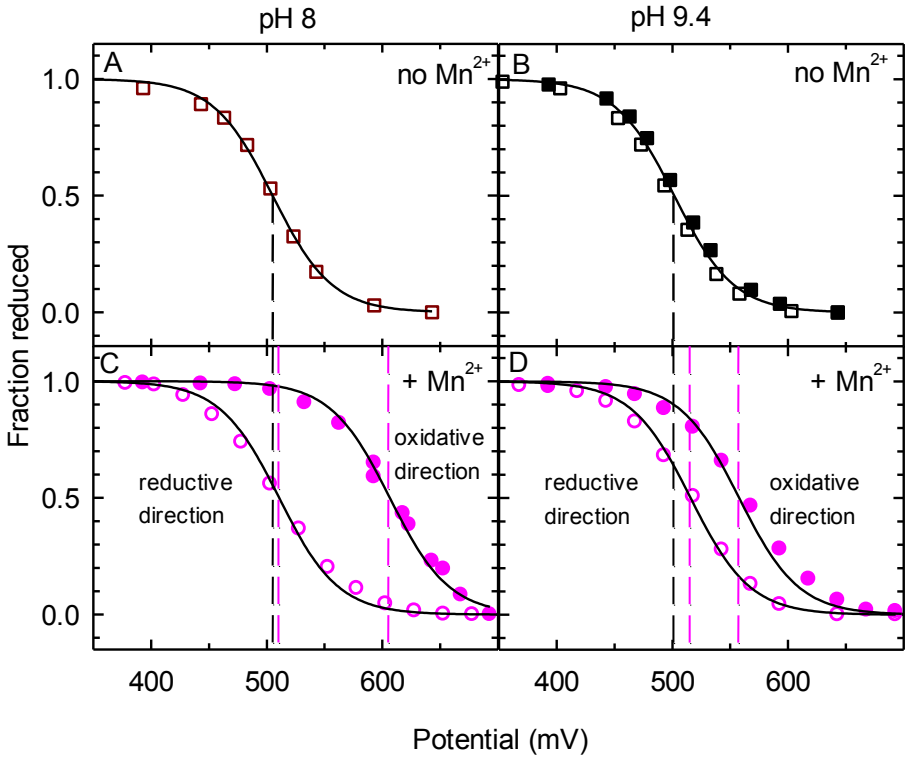

Figure 3.12. The oxidation-reduction potential of the P/P^+ with and without Mn^{2+}. The amplitude of the dimer peak at 865 nm is plotted against applied potential without Mn^{2+} (A and B) and with Mn^{2+} (C and D) at pH 8 (A and C) and pH 9.4 (B and D). Closed symbols represent data points taken in the oxidative direction, while open symbols represent points taken in the reductive direction. Measurements were conducted at least twice in both directions and the errors are smaller than 4% and graphically smaller than the selected symbol sizes. The Nernst fittings (solid lines) are used to determine the midpoint potentials (Table 3.2). Conditions : 80 mM BTP, 70 mM KCl, ~200 µM RC, 300 µM ferro/ferricyanide and 5 mM Mn^{2+} where applicable.

Table 3.2 Electrochemical midpoint potential of the P/P^+ couple with and without Mn^{2+} at pH 8 and pH 9.4

Direction	pH 8		pH 9.4	
	no Mn^{2+}	Mn^{2+}	no Mn^{2+}	Mn^{2+}
Oxidative	505 ± 5 mV	605 ± 5 mV	501 ± 4 mV	555 ± 5 mV
Reductive	505 ± 5 mV	510 ± 5 mV	501 ± 4 mV	515 ± 5 mV

3.4.3. Spectroscopic evidence of Mn^{2+} binding

The influence of Mn^{2+} on the electrochemical potential of P and *vice versa* indicate a strong interaction between Mn^{2+} ions coordinated by BTP and the P. The sensitivity of the cofactors to local electric fields allows us to investigate any changes in their spectroscopic signatures when they are in the presence of Mn^{2+} ions. The influence of Mn^{2+} ions on the Q_Y dipole moments of the pigment molecules (dimer, monomers and pheophytins) are investigated by NIR spectroscopy. The spectra with and without Mn^{2+} were recorded under an external applied potential of 293 mV in the electrochemical cell. Due to the external applied potential, the auto-oxidation of Mn^{2+} was not a factor. All Mn was present in the +2 oxidation state and P was only in the reduced state. The dark spectra (PQ state) with and without Mn^{2+} are presented in Figure 3.17 A (pink trace for $+Mn^{2+}$ and black trace for $–Mn^{2+}$). The spectra were decomposed to individual contributions of cofactors modeled each with single Gaussians for the pheophytin (760 nm) and dimer peaks (865 nm) and double Gaussian functions for the monomer peak (800 nm). The fit to the monomer peak is shown with dashed lines (Fig. 3.13A purple trace for $+Mn^{2+}$ and gray trace for $–Mn^{2+}$). The fits for the pheophytin and dimer were not shown in Figure 3.13 for clarity. The PQ state spectra show differences in the absorption peaks of the cofactors, indicating the influence from the local electric field generated by Mn^{2+} ions in the vicinity.

The difference spectrum between the spectra with and without Mn^{2+} is presented in Figure 3.13 B (gray). The presence of Mn^{2+} in the vicinity of the cofactors causes a hypsochromic shift of the dimer from 867 nm to 865 nm and a broadening of the monomer band (blue) centered at 800 nm. These electrochromic absorption changes indicate an interaction between Mn^{2+} and the BRC and

suggest binding of Mn^{2+} to the BRC in the vicinity of P and BChl monomer. The broadening of the 800 nm band suggests that there is a change in the Q_Y dipole moment of both the BChl monomer A and B molecules and the shift of the 865 nm band indicates the change in polarizability of P.

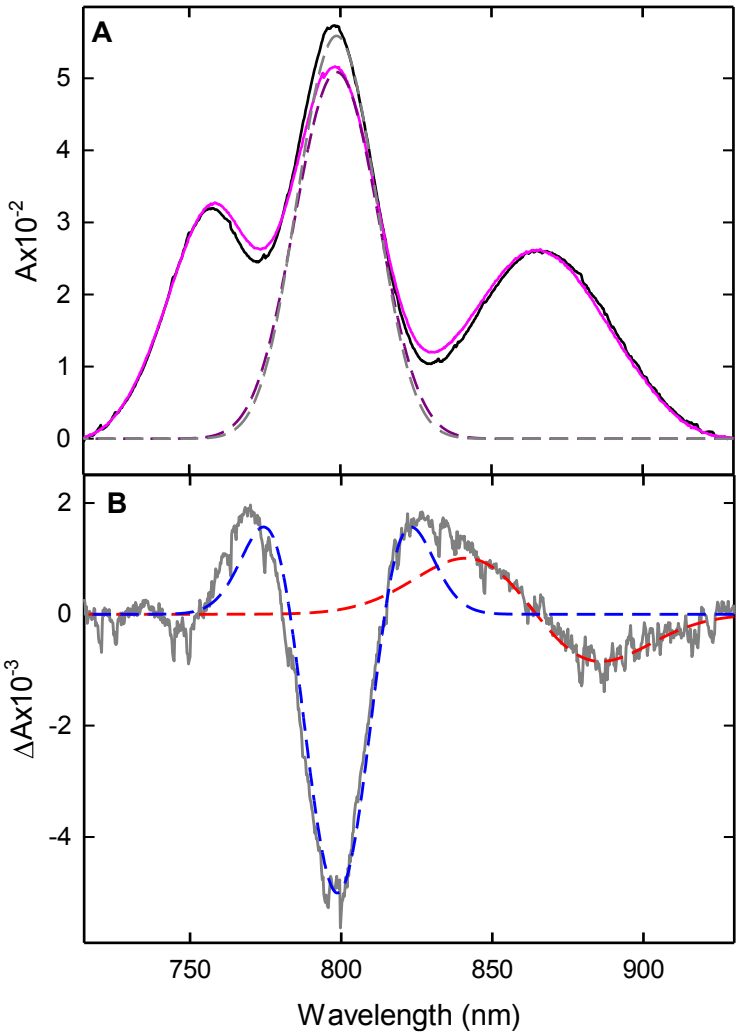

Figure 3.13 Spectroscopic differences in the PMn^{2+} and P states. A. The dark-adapted spectra with Mn^{2+} (pink) and without Mn^{2+} (black). Each spectrum was decomposed by assigning Gaussian fits to the corresponding peaks in the spectrum. A single Gaussian function was used for the dimer and pheophytin peaks, while the sum of two Gaussians was used for the monomer peak (Eq. 2.4). The monomer peak is shown in purple for $+Mn^{2+}$ and in gray for $–Mn^{2+}$. The other peaks are omitted for clarity. B. The difference spectra between the ground state spectra with and without Mn^{2+} is presented in gray. The spectra were fitted with peak shifts and broadening according to the fittings obtained from the ground state spectra (dashed lines). The dimer suffers a hypsochromic shift (red) from 867 nm to 865 nm and the monomer suffers a broadening of the peak centered at 800 nm (blue). Conditions are the same as in Figure 3.16 at pH 9.4.

3.5 The influence of pH on the *in situ* Mn^{2+}-BTP coordination complex

As demonstrated earlier at pH 9.4 coordination of Mn^{2+} ions by BTP is essential for their ability to act as secondary electron donors to the oxidized dimer. The potential of the Mn^{2+} was reduced to 349 mV and the potential of the dimer increased to 555 mV. Two coordinating BTP molecules per Mn^{2+} ion were identified (Fig. 3.6). The protonatable amine groups of the BTP have also been shown to play an important role in coordinating the Mn^{2+} ions that were identified as the secondary electron donor to the oxidized dimer. Without Mn^{2+} coordination, the pK_as of the amine groups are 6.6 and 9.0 in aqueous solution where the dielectric constant can be estimated as 80. At pH values below the first pK_a, spectroscopic evidence suggests that there is no coordination of the Mn^{2+} (see Fig. 3.7). One deprotonated residue is enough to coordinate the Mn^{2+} ions and reduce the electrochemical potentials to as low as 391 mV. However, studies involving the Mn^{2+} and BRC at pH 8 have shown that BTP in its semi deprotonated form cannot facilitate the formation of a Mn-complex that could serve as a secondary electron donor to the oxidized dimer. It appears from the presented pH dependency that the association between the fully deprotonated amines of the BTP and the lowest potential Mn^{2+} is what allows the Mn-BTP complex to act as a secondary electron donor. This association can also shift the apparent pK_a value of the second amine, depending on the nature of the electrostatic interaction between the species involved.

We are interested in the apparent pK_a of the *in situ* Mn^{2+}-BTP complex and the relationship of the protonatable amine groups with the ability of the lowest potential Mn^{2+} ions to act as secondary electron donors. In order to assess the relationship, the recovery of the dimer band at

865 nm after a single flash was recorded at different pHs (Fig. 3.14 A). Q_B active samples were used as the effect of secondary electron donation is more visible. The kinetics traces were decomposed as previously described into their components (Fig. 3.4). The rates and the fraction of the total amplitude are plotted with respect to pH (Fig. 3.14 B and C).

The most noticeable effect of varying pH is an increase in the fraction of the fast components (attributed to either Mn^{2+} electron donation to P^+ at higher pHs or with the $P^+Q_A^-$ charge recombination at lower pH values) with increasing pH corroborated with a decrease in the amplitude of the slow component (attributed to $P^+Q_B^-$ to PQ_B charge recombination). The changes in these kinetic parameters were fit with Henderson-Hasselbach curves for both a single proton per unit of pH and two protons per unit of pH (Eq. 2.6 and 2.7). Both fits are presented in Figure 3.18 C (dashed lines for single proton and solid lines for double proton). The model using two protons per pH provides the better fit to the data. This model indicates the presence of two protonatable residues per Mn^{2+} ion and confirms the relationship found in Figure 3.5 B.

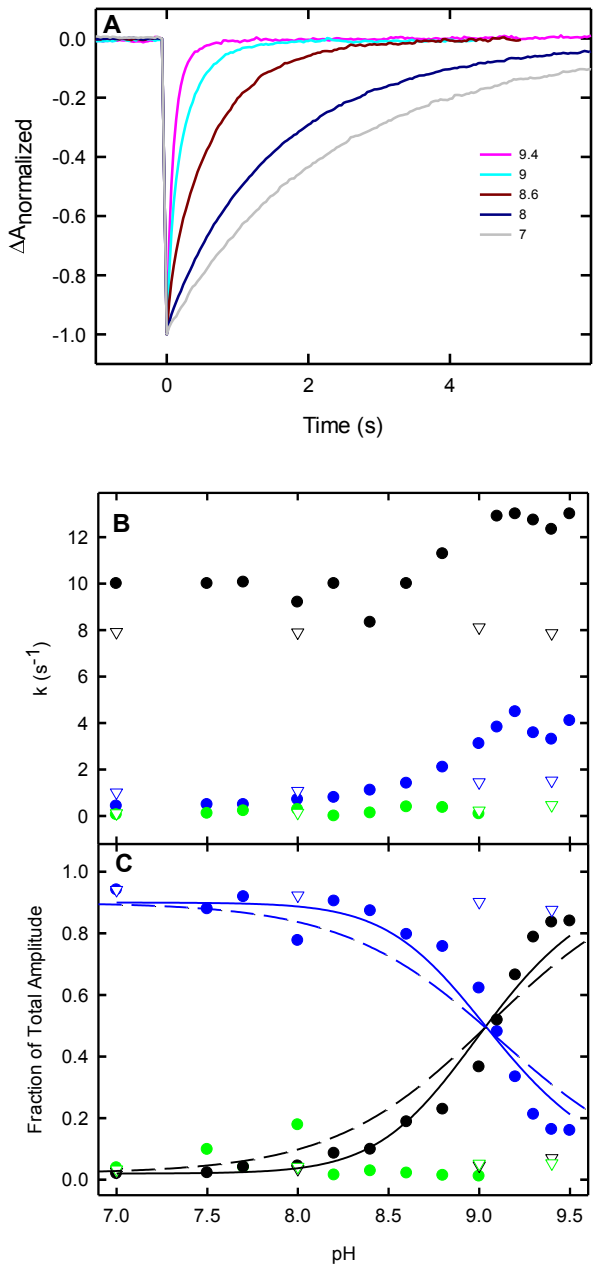

Figure 3.14. The effect of pH on the recovery of the dimer after single flash excitation. Single flash excitation experiments were conducted on a sample containing BRC and Mn^{2+} in BTP. The kinetics of the dimer band (865nm) recovery were monitored at different pHs. Representative traces are shown in panel A. The rates and fractions of the total amplitudes are plotted with respect to pH (B and C). Black circles represent kinetic parameters of the fast component, blue circles correspond to parameters of the slow component and green circles are attributed to the amplitudes and rate constants of the very slow component. The attribution of the symbols is done according to Figure 3.4. Open triangles represent the respective parameters in the same conditions, without Mn^{2+} added. Increasing pH causes an increase in the amplitude of the fast component correlated to a decrease in the amplitude of the slow component. One proton per pH (dashed lines) and two proton per pH (solid lines) Henderson-Hasselbach models are used to fit the two curves (Eq. 2.6 and 2.7). The two proton model fits the data better. pK_a values of 8.84 ± 0.04 (for black trace) and 8.89 ± 0.04 (for blue trace) are obtained. Conditions: 1 µM RC, Q_B active, with 15 mM Mn^{2+} in 80 mM BTP

The pK_a values obtained were 8.84 ± 0.04 (for black trace) and 8.89 ± 0.04 (for blue trace). There is approximately a 0.1 pH decrease from the standard pK_a of BTP, possibly due to the interaction between the amine and the Mn^{2+} ions. The high concentration of Mn^{2+} (15 mM) also seems to slightly increase the $P^+Q_A^-$ to PQ charge recovery rate possibly due to the unfavorable electrostatic interactions between the Mn^{2+} and the P^+.

The effect of pH on the BRC with the Mn-BTP complex under continuous illumination was also studied. This produced an independent set of measurements of the apparent pK_a value of the *in situ* Mn-BTP complex. A sample containing 1 μM BRC (Q_A active) with 5 mM Mn^{2+} and 15 mM BTP was exposed to 5 minutes of illumination. The recoveries of P^+ during illumination were monitored for different pH values. During continuous illumination, electron donation may or may not occur from the Mn^{2+} to the oxidized dimer depending on the pH. The percent of oxidation varies with pH, being at its maximum at pH 9.4 and decreasing at lower pH values. The fraction of P^+ at maximum oxidation was measured and plotted against pH. Henderson-Hasselbach models involving 1 or 2 protons per pH were used to fit the data (Eq. 2.6 and 2.7). The latter model fits the data significantly better (Fig. 3.15) and a pK_a of 8.90 ± 0.03 is obtained, which reinforces the previous results shown in Figure 3.14.

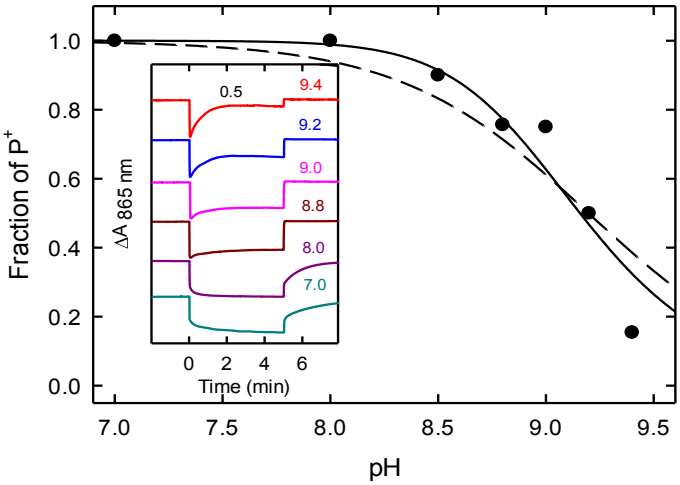

Figure 3.15. The effect of pH on the secondary electron donation from Mn^{2+} to P^{+} during continuous illumination. The formation and disapearance of P^{+} during continuous illumination is monitored at various pH values. The fraction of P^{+} available at full oxidation is plotted against pH (black circles). Henderson-Hasselbach models with 1 H^{+}/pH and 2 H^{+}/pH are used to fit the data (dashed and solid curves, respectively). The apparent pK_a obtained was 8.90 ± 0.03, which is in agreement with previous measurements. In the insert, the kinetic traces of the recovery of the 865 nm dimer band are presented for representative pH values. Conditions: 1 µM RC, 100 µM terbutryn, 5 mM Mn^{2+} in 15 mM BTP.

3.6. The influence of the Mn^{2+}-BTP coordinated complex on the ability of cyt c^{2+} to act as secondary electron donor

3.6.1 The reduction of cyt c^{3+} by Mn^{2+}

Anoxygenic reaction centers are naturally adapted to use cyt c_2^{2+} as a very efficient secondary electron donor to the oxidized dimer. However, this process, like many others, is influenced by environmental conditions. Changes in pH and ionic strength influence the midpoint potential of cyt c_2^{2+} *in vitro* and subsequently the redox interaction between it and the dimer [67,68,69]. Our study investigates the effect of millimolar concentrations of Mn^{2+} on the ability of cyt c^{2+} to

donate its electron efficiently to the oxidized dimer. The potential of cyt c_2^{2+}/cyt c_2^{3+} in standard conditions is reported at 300 mV and it decreases with increasing pH [66].

A solution containing 10 μM cyt c_2^{3+} in 80 mM BTP was prepared and the amplitude of the peak at 550 nm was plotted with respect to time after adding 5 mM Mn^{2+}. The peak at 550 nm is characteristic to the reduced cyt c_2^{2+}. The increase in the peak in Figure 3.16 shows that Mn^{2+} is reducing cyt c_2^{3+} to cyt c_2^{2+}. This is the first observation of a redox interaction between Mn^{2+} and cyt c_2. The reduction occurs faster at pH 9.4 than at pH 8 likely due to the decreased potential of manganese at higher pH values (332 mV vs 391 mV). The 49 mV difference between the lowest potential components at each pH provides an extra driving force for the electron to be exchanged.

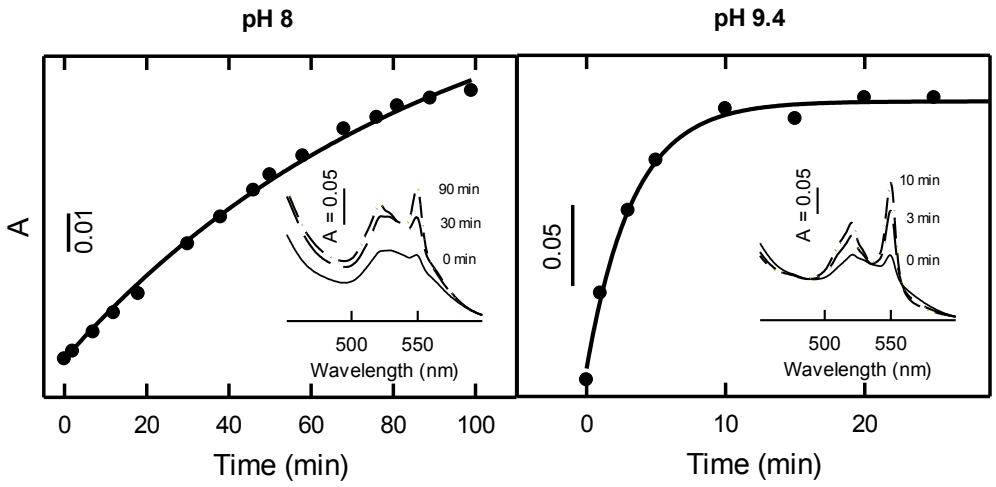

Figure 3.16 Reduction of cyt^{3+} to cyt^{2+} by Mn^{2+}. The amplitude of the peak at 550nm, characteristic of reduced cyt c^{2+}, is plotted with respect to time after adding Mn^{2+} to the solution. As time increases, more cyt c^{2+} is formed. The data is fit with exponential growth kinetics. The lifetimes of the reduction process were measured as 89 min at pH 8 and 4 min at pH 9.4. Conditions: 10 μM cyt c_2^{3+}, 80 mM BTP and 5 mM Mn^{2+}.

3.6.2 Competitive selection of electron donor between cyt^{2+} and Mn^{2+} for the oxidized dimer

The ability of Mn^{2+} to reduce cyt^{3+} in coordinated BTP complexes signifies an interaction between the two. This interaction might influence the efficiency of cytochrome as a secondary electron donor to the oxidized dimer. A single flash excitation experiment was set up where the electron donation from Mn^{2+} and/or cyt c^{2+} was observed by comparing the 865 nm dimer band recovery kinetics (Fig. 3.17). The concentrations were selected to reflect the most efficient electron transfer using manganese and the abundance of cyt *c* in bacterial photosynthesis. Q_B active BRCs (1 μM concentration) were used to better see the electron donation from Mn^{2+}. Sodium-ascorbate was added to samples containing cyt c^{2+} to act as a reductant for the oxidized cytochrome in order to avoid fully consuming the cyt c^{2+}. Without a secondary electron donor (black trace), the recovery kinetics follows the $P^+Q_B^-$ to PQ_B charge recombination. In samples containing cyt c^{2+}, a very fast electron donation occurs, which is not resolved due to the time resolution used in this experiment resulting in a flat signal (red trace). Presence of Mn^{2+} only causes electron donation to the oxidized dimer after the flash with a lifetime of ~85 ms (pink trace). Simultaneous presence of Mn^{2+} and cyt c^{2+} yields a recovery kinetics that is similar to that observed in the presence of Mn^{2+} only (cyan trace). This observation suggests that the presence of manganese inhibits the rapid electron donation from cytochrome. The absorbance changes were also recorded at 550 nm and shown in the insert of Figure 3.17. With just cytochrome added (red trace in the insert), cyt c^{3+} was formed immediately (limited by our data sampling) after the flash and the recovery due to ascorbate occurred slowly. With both Mn^{2+} and cyt^{2+}, there is no change in the signal from cyt *c*, (except a tiny overlap from the P^+Q^- spectrum). This

proves that under the conditions used in the competition between Mn^{2+} and cyt^{2+}, Mn^{2+} is the preferred electron donor regardless of the much faster electron donation rate from cytochrome. This indicates that the cyt^{2+} is either disabled or inhibited from binding by the high concentration of Mn^{2+}.

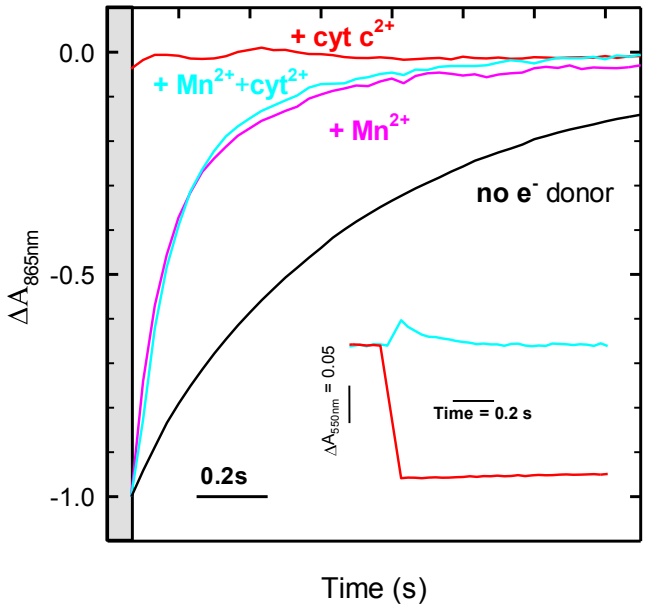

Figure 3.17. Recovery of the dimer from single flash excitation with and without various electron donors. The recovery of the P band at 865 nm is measured after a single flash excitation. The black trace is the recovery of the $P^+Q_B^-\rightarrow PQ_B$ without any secondary electron donor present. The red trace is the recovery of P^+ with added cyt c^{2+} present. The electron donation is undetectable due to the data sampling rate smaller than the lifetime of the reaction (one to a few microseconds). The pink trace represents the recovery with Mn^{2+}. The recovery occurs with a lifetime of ~ 85 ms. The cyan trace is the recovery with both secondary electron donors present. The recovery is very similar to that of the sample containing only Mn^{2+}. This indicates that Mn^{2+}, not cyt c^{2+}, participates in reducing the oxidized dimer. In the insert, the change in the absorbance at 550 nm, characteristic of the cyt^{2+}, is presented. In a sample containing only cyt^{2+} (red trace) the electron is donated to P^+, forming cyt^{3+} which reduces slowly due to the ascorbate present. In a sample containing both cyt c^{2+} and Mn^{2+}, the only change in absorbance is due to an overlap with the P^+Q^- specrum. This confirms that cyt c^{2+} does not participate in the redox reaction, possibly due to interference from Mn^{2+} or inhibition of the cyt c^{2+} binding site. Conditions: 1 µM RC, 80 mM BTP, pH 9.4. For Mn^{2+} samples 5 mM Mn^{2+} was added. For cyt c^{2+} samples, 10 µM cyt c^{2+} and 20 µM sodium ascorbate were added.

Discussion

First-time evidence for efficient electron donation from Mn^{2+} to the oxidized dimer in native bacterial reaction centers has been presented and the electron transfer rate has been determined both intrinsically and under diffusional limitations. The reaction is made possible by proper coordination of the Mn^{2+} ions with BTP, which reduces the oxidation/reduction potential of the metal ion significantly. The influence of pH on the electron donation process highlights the importance of the deprotonated amine groups of BTP in the proper coordination of the complex. The association between Mn^{2+} and P causes an elevation of P/P^+ potential in the oxidative direction indicating the presence of Mn^{2+} in the vicinity of the dimer. The Q_Y dipole moment of the BChl molecules has been found spectroscopically affected by the presence of Mn^{2+} ions. In a competitive environment with two available electron donors, cyt c_2^{2+} and Mn^{2+} coordinated by BTP, the oxidized dimer is preferentially reduced by the Mn^{2+}.

In the discussion, the focus lies on assigning the observed phenomenon to interactions at the molecular level and on the various implications of this study. The coordination of BTP with Mn^{2+} is explained in terms of the observed behaviour in reference to previously determined complex structures. The characteristics of the observed electron transfer process are analyzed with respect to the total driving force, molecular distance between donor and acceptor, and diffusion limitations. A complex reaction mechanism is proposed for the electron transfer from Mn^{2+} to P^+ under continuous illumination or during multiple flash excitation. The electrostatic influence of the presence of a charged coordination complex near the BRC cofactors is considered. The destabilization of the natural electron donor cyt c_2^{2+} by Mn^{2+} interaction is

explained. Finally, the implications of this study are discussed both in terms of evolution of photosynthesis and enzymatic reactions in Mn containing metalloproteins.

4.1 Structural evidence of the Mn^{2+}-BTP coordination complex

The ability of Mn^{2+} to donate an electron efficiently to the oxidized dimer is enabled by the coordination with BTP. The coordination significantly reduces the oxidation/reduction potential of the Mn^{2+} from 1.2V in the *hexa-aquo* coordination in water [37,70,71]. At pH 9.4, where electron donation was observed, the existence of at least three types of Mn^{2+} with respective midpoint potentials of 332 mV, 452 mV and 601 mV was observed (Table 3.1). The decreased potential provides sufficient driving force for the Mn^{2+} to perform the reduction of P^{+}. The *in situ* potential measurements have revealed that the Mn^{2+} with 332 mV (349 mV *in situ*) is solely responsible for performing the electron transfer to the oxidized dimer (Fig. 3.11).

Even at pH 8, where electron donation was not observed, the midpoint potentials of three types of Mn^{2+} were found significantly lower : 391 mV, 507 mV and 652 mV, than the potential of Mn ions in coordination with water only (Table 3.1). The ~50 mV difference between the respective Mn^{2+} potentials at pH 8 and 9.4 could indicate that the same types of Mn^{2+} exist in both cases. The difference is possibly given by the different protonatable states of the amine groups of BTP at the respective pHs. The lack of both amine protons at pH 9.4 would provide a more favorable electrostatic interaction with the Mn^{2+} and Mn^{3+}, effectively reducing the potential of the Mn^{2+}/Mn^{3+} transition. The absence of spectral features at pH 6 (Fig. 3.7) indicates that when

both amines are protonated, BTP can no longer coordinate Mn^{2+} and thus unable to lower its potential to the desired range.

The influence of the protonational state of the amine groups on Mn^{2+} coordination is also demonstrated by the observation that electron donation to the oxidized dimer could only occur at pH 9.4, not pH 8, despite the fact that the potential at pH 8 is also low enough for the reaction to occur. Two separate pH titrations involving electron donation from Mn^{2+} to the oxidized dimer (Fig. 3.14 and 3.15) measured the same apparent pK_a of ~8.9 for the electron donor Mn^{2+}. The value is close to the measured pK_a of ~9 for the fully deprotonated BTP. The difference is possibly due to the favorable interaction between the deprotonated amines and the positively charged Mn^{2+}.

The model we used revealed the stoichiometry of Mn^{2+}:BTP necessary for efficient electron donation. Coordination with BTP involves two amine groups per Mn^{2+}. However, the model used in Figure 3.6 indicates that the change in extent of oxidation due to BTP concentration requires two BTP molecules to coordinate the Mn^{2+} reducing agent. Thus, the coordination necessary for the Mn^{2+} could either be provided by amines in different BTP molecules or by amine groups of one molecule and hydroxyl groups of another molecule. Although studies involving BTP coordination of transition metals are rare in the current literature, there is evidence of BTP coordinating Co^{2+} and Zn^{2+} in ratios of 2:1 ligand to metal ion [72].

Ferguson et al. [38] also reported complex coordination of Mn^{2+} by BTP. The study was conducted in crystallized synthesised clusters and provides the only available structure of a Mn^{2+}/Mn^{3+}-BTP complex (Fig. 4.1). The reported structure contains six Mn ions arranged symmetrically in a trimer of dimers with two of the dimers in their oxidation states of +2 and one

pair having +3 charges on each Mn. The presence of Mn^{3+} in the reported crystal structure also indicates that two of the manganese ions must have low potentials and they most likely auto-oxidize during the crystal growth process. Our time dependent spectroscopic analysis also supports the auto-oxidation of manganese as the complex lost its ability to serve as secondary electron donor a few hours after making the solution (Fig. 3.8). Other similarities between the synthesized cluster and the Mn coordinated by BTP in solution occur in the number and type of Mn^{2+} atoms identified. The six Mn ions in their reported structure form three pairs, while at least five Mn^{2+} ions in solution form two pairs. We suspect that we generated the same complex but the limitations of the spectroelectrochemical redox titration did not allow us to measure potentials above 700 mV. It is highly likely that the sixth manganese has a higher potential. The auto-oxidizing Mn^{2+} at pH 9.4 was identified as the one with potential of 332 mV (Fig. 3.10) as well as the one responsible for donating the electron (Fig. 3.11).

In the synthesized clusters, both amine and hydroxyl groups are reported to provide coordination to the Mn^{2+}/Mn^{3+} ions. Coordination is provided by seven ligands per Mn ion, where the ligands originate from 10 different BTP molecules and some are shared amongst Mn ions (Fig. 4.1). The ratio of protonatable amines coordinating Mn^{3+} ions in the cluster is 2:1. This is also in accordance with the ratio obtained in solution where two amines are responsible for coordinating the electron donating Mn^{2+}. Furthermore, the functional groups coordinating the Mn^{2+} (two amines and five hydroxyl groups) are provided by just two separate BTP molecules. This is in accordance with the ratio of 2:1 BTP to Mn^{2+} donating the electron determined in Figure 3.6). The importance of protonatable groups that not only lower the potential of manganese but can also facilitate its binding to proteins have been explored earlier in mutant BRCs [60]. It has been found that different anions can bind with different stoichiometry to Mn^{2+}. Two bicarbonate/Mn^{2+}

and one acetate/Mn^{2+} stoichiometries were identified that altered the pH dependency of Mn^{2+} binding and oxidation by screening the unfavorable Coulomb interactions. A similar role for BTP in our work here is highly probable.

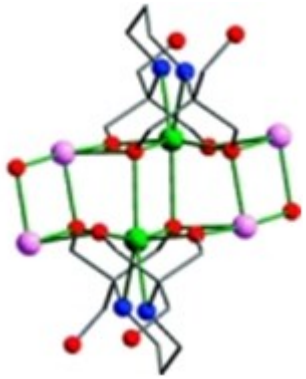

Figure 4.1 Structure of the Mn-BTP cluster. The synthesized Mn-BTP complex as reported by Ferguson et al. [38]. Amine groups are identified in blue, oxygen groups in red, Mn^{2+} in pink and Mn^{3+} in green. The presence of the Mn^{3+} oxidation state indicates that coordination has lowered the potential of Mn^{2+} significantly.

4.2 Characteristics of the electron transfer from Mn^{2+} to the oxidized dimer

4.2.1 Driving force for the electron transfer between manganese and the bacteriochlorophyll dimer

The oxidation of Mn^{2+} by P^{+} in BRCs can be modeled using the Marcus theory of electron transfer. In this analysis, the kinetic rate of the electron transfer depends on the free energy difference between the two species' (ΔG^{0}) and the reorganization energy λ (Eq. 1.1). In a redox reaction, the reorganization energy depends on the overlap between the potential energy functions of the donor-acceptor couple before and after the reaction. The electronic coupling would need to be calculated from measurements of the reaction rates at different temperatures.

The free energy difference depends solely on the reduction/oxidation potential of the species involved and the number of electrons transferred in the process. In the case of electron transfer from Mn^{2+}, it is safe to assume only one electron is exchanged and Mn^{3+} is formed as P^+ can only accept one electron. Also, the lack of precipitation in the solution indicates that Mn^{4+} is not formed. The driving force per electron ΔG^0 is given by equation 1.3. For the reaction to take place spontaneously ΔG^0 should be negative, hence the electrochemical potential of the acceptor should be higher than that of the donor. Coordination by BTP provides a Mn^{2+} with a low potential (349 mV measured *in situ* at pH 9.4, Fig. 3.11), while association between Mn^{2+} and the dimer raises the potential of the electron acceptor (P^+) to 555 mV (Fig. 3.12).

The driving force for the electron donation to the oxidized dimer by Mn^{2+} is calculated as 0.206 eV. In terms of electron donation, the free energy difference is smaller to that of the natural secondary electron donor to P^+, cyt c_2^{2+}, which has a driving force of ~0.50 eV [59]. In PS II, the driving force for the reduction of the Y_Z tyrosine by the manganese ions in the oxygen evolving-complex is higher (~0.30 eV) [73]. In Mn^{2+} oxidizing BRC mutants, the reported driving force values varied between 0.05 and 0.12 eV [37]. In previous Mn^{2+} oxidation studies in mutant BRCs, the rates were found to range from ~ 30 ms without a designed binding site [37] to ~10 ms if strong binding was achieved [49,44,74]. Our slower time constant of ~83 ms indicates that in our system, the reorganization energy for the electron transfer is higher and the electronic coupling between the two must be weaker.

The reorganization energy is inversely proportional to the distance between donor and acceptor. Even if the driving force is high, the rate could be low if the donor and acceptor are too far apart. One example is the charge recombination of P^+Q^- to PQ, which has a driving force of 0.5 eV but has a rate of 1 s^{-1} due to the ~23.4 Å distance between the two species in question. Since the rates

of Mn^{2+} oxidation in our system are similar, we expect a distance of over 20 Å between the Mn^{2+} and the P^+ (see later Figs. 4.2 and 4.3).

4.2.2 The rate of Mn^{2+} oxidation in comparison with other systems

The intrinsic electron donation time constant from the Mn^{2+} to P^+ assuming a bound manganese to the protein was measured at ~ 83 ms. This rate is in direct competition with the $P^+Q_A^-$ charge recombination, which has a lifetime of 122 ms (Fig. 3.3A). The natural electron donor, cytochrome c_2, donates the electron in one to a few microseconds, ferrocene donates the electron in ~250 μs, while 3,6-diaminodurene (DAD) has an electron donation time of >1 ms [15]. These reactions were studied extensively [73,74]. Even though it has been proposed that aforementioned molecules donate their electrons to P^+ from the same distance, the significant differences between their electron transfer rates are due to different driving forces and reorganization energies. Although the electron donation time for Mn^{2+} to P^+ is orders of magnitude higher than the aforementioned molecules, it is approximately an order of magnitude shorter than the lifetime of the $P^+Q_B^-$ charge recombination at 650 ms, making it an efficient electron donor.

A weak association between Mn^{2+} and the BRC has been demonstrated by the determined binding constant of 6.5 mM. A diffusion limited mechanism is suggested by the linear dependence of the rate of electron donation from Mn^{2+} to P^+. The second order rate constant for Mn^{2+} has been measured at 4.0×10^2 $M^{-1}s^{-1}$. A previous study conducted by Kalman et al. [37] regarding Mn^{2+} secondary electron donation to the dimer of mutant BRCs with elevated

potentials measured the rate constant at 9×10^4 $M^{-1}s^{-1}$. Reduction of P^+ by cyt c_2^{2+} has a measured second-order rate constant in the order of 10^9 $M^{-1}s^{-1}$ [74]. In photosystem II, the bound manganese is oxidized by tyrosine Y_Z^* with a rate constant of 2×10^4 $M^{-1}s^{-1}$ [37]. Second-order rate constants for manganese oxidation were measured up to 6×10^6 $M^{-1}s^{-1}$ in PS II samples with the oxygen-evolving cluster removed. The orders of magnitude difference between the rate in our systems and the other reported rates are possibly due to the high reorganization energy, long donor-acceptor distance or the need for a conformationally-gated mechanism (Fig. 3.5).

The rate of association between Mn^{2+} and the BRC can be calculated using the observed electron donation under continuous illumination with a rate of 0.192 s^{-1} and the rate of the electron transfer of 11.6 s^{-1} using the following equation:

$$\frac{1}{k_{obs}} = \frac{1}{k_{diff}} + \frac{1}{k_{ET}} \tag{4.1}$$

The Mn^{2+} diffuses into its interaction site with a rate constant of 0.195 s^{-1}, resulting in a measured lifetime of 5.1 s. In comparison, cytochrome diffuses into its binding pocket with a lifetime of microseconds [77]. Ferrocene is also reported to use the same binding site, diffusing into the pocket with a lifetime faster than 0.1 ms [74]. The slow diffusion rate might suggest that the Mn^{2+} cannot access the cyt c_2 binding site and diffuses to another location.

4.2.3 Calculation of the distance between Mn^{2+} and the oxidized dimer

The relationship between the electron donation rate of Mn^{2+} to P^{+} and the distance between donor and acceptor was analyzed. As discussed in section 4.2.1, the reorganization energy and subsequently the rate of electron transfer is inversely dependent on distance. Proteins have adapted for short distances in order to increase the electronic coupling and yield productive electron transfers [33]. The distances between cofactors in the BRC vary from 5 Å between the BChl dimer and monomer to ~23.4 Å between the dimer and Q_B. The difference in distances is part of the reason electron transfer from dimer to the quinone is preferred to charge recombination. In terms of secondary electron donors to the dimer, the cytochrome binding site lies ~10 Å away from the dimer. The designed binding site for Mn^{2+} in the study conducted by Thielges et al. [49] also lies ~ 10 Å away from the dimer. In our system, the distance between Mn^{2+} and P^{+} is calculated using the Dutton ruler [78], which is an empirical relationship between the rate of electron transfer and the distance between donor and acceptor based on the packing of the respective protein. The relationship is given by the following equation:

$$k = 10^{13} e^{-\beta(R-R_0)} \tag{4.2}$$

In this relationship the rate constant (k) is dependent on a packing factor (β), the distance between donor and acceptor (R) and the van der Waals distance (R_0). The value of β for the BRC (the slope of the line in Fig. 4.2) has been determined as 1.4 $Å^{-1}$ using the crystallographic distances between cofactors and the measured rates in the electron transport chain [33]. The same relationship was re-plotted for our purpose. By knowing the electron transfer rate, the distance between the Mn^{2+} and P^{+} can be determined (Fig. 4.2).

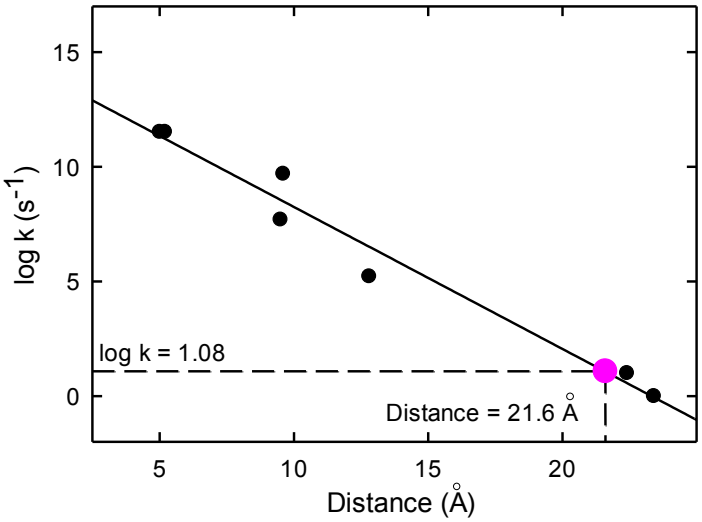

Figure 4.2. Influence of electronic coupling on the observed rate of electron transfer. The relationship between electron donation rates and the distances between cofactors in the BRC is recreated according to available data (Moser 2008). A β value of 1.4 Å^{-1} is forced on the fit (solid line). The natural logarithm of the obtained electron donation rate of 11.6 s^{-1} is plotted (pink circle). A distance of 21.6 Å between the donor (Mn^{2+}) and the acceptor (P^{+}) is obtained.

The Dutton ruler gives an approximate distance between Mn^{2+} and P^{+} of 21.6 ± 1 Å, assuming the electron transfer occurs within the BRC. This value is similar to the P–Q_A distance of 22.4 Å which is in accordance with the similarity between the electron donation rates of the two pairs ($P^{+}Mn^{2+}$ and $P^{+}Q_A^{-}$). A circle with a radius of 21.6 Å and a line thickness of 1 Å is plotted in order to identify possible association sites between Mn^{2+} and BRC (Fig. 4.3). The cytochrome binding site (on top) lies well within the circle (Fig. 4.3 C, see also Fig. 1.6). Mn^{2+} binding to the site would result in a faster electron transfer rate. The circle also encompasses part of two solvent-accessible cavities which lie at the required distance from the dimer. One is in the vicinity of monomer A and the other one in the vicinity of monomer B (Fig. 4.3 A and B). Analysis of the structure using Pymol (published by Schrödinger Inc.) has shown these cavities to measure between 25 and 35 Å in diameter and might be able to accommodate even molecules as large as a Mn^{2+}/Mn^{3+}-BTP cluster. The commonly used reducing agent sodium borohydrate

($NaBH_4$) was reportedly able to access monomer B by diffusing in the respective cavity [79]. In solubilised RCs, detergent molecules have been reported in both cavities [78,79,62]. Lipid molecules have also been reported in the empty carotenoid binding site near monomer B [62]. The presence of other molecules in the solvent-accessible cavities might indicate a site for association between Mn^{2+} and BRC where the electron transfer would take place.

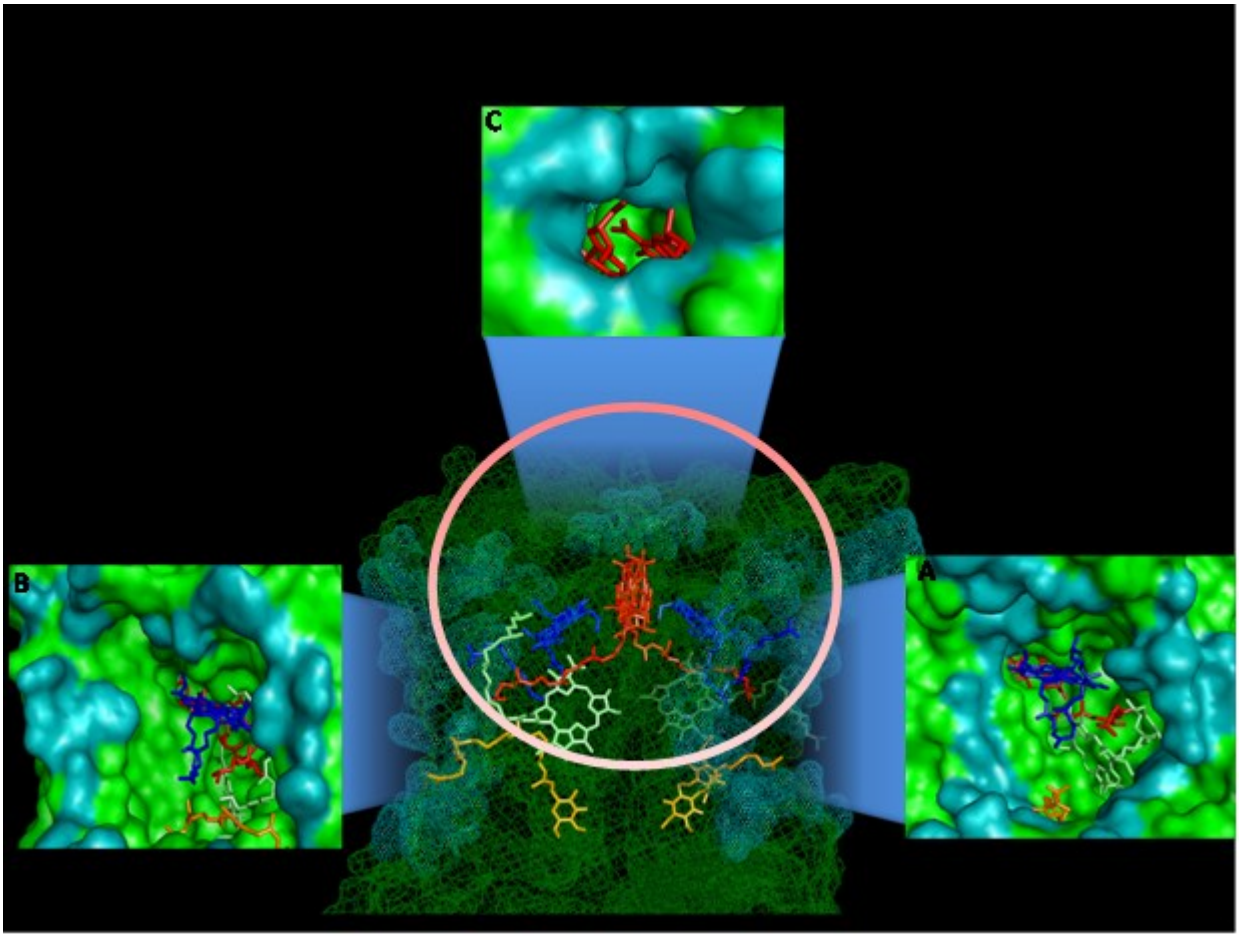

Figure 4.3 Potential association sites between the BRC and the Mn^{2+}. The structure of the BRC is presented with key cofactors highlighted: BChl dimer (red), BChl monomers (blue), BPheo (lime) and quinones (orange). A circle with a diameter corresponding to 21.6 Å is drawn from the center of the dimer and has a width corresponding to 1 Å. Possible association sites are identified in the structure with light blue shading and rotated and zoomed in for clarity: the cavity near monomer A (A), the cavity near monomer B (B) and the cytochrome binding site (C). PDB code: 1RCR

4.2.4 Proposed mechanism for the electron transfer from Mn^{2+} to P^+ in Q_B active BRCs during continuous illumination and multiple flash excitation

The electron donation from Mn^{2+} to P^+ has been characterized by an intrinsic lifetime of 83 ms and a slower diffusional process with a lifetime of 5.1 s. A multiple flash excitation experiment was conducted in Q_B active samples to bridge the gap between the two processes (Section 3.1.3). The analysis of the kinetic recoveries during the multiple flash illumination indicated the presence of two populations of BRCs. Furthermore, in the percentage of P^+ that could be reduced by Mn^{2+}, a light-induced conformational change occurring with a lifetime of ~800 ms is necessary in order to have Mn^{2+} diffuse near the dimer. This conformational change was attributed to a shift in the dimer band from 865 nm to 861 nm (Fig. 3.11, insert). Upon charge separation this alteration, P_{861}^+-Mn^{2+} first needs to be formed by the diffusion of the Mn^{2+} as an intermediate and it decays later by electron donation to form the P_{861}-Mn^{3+} association at the donor site. In this section, a mechanistic approach relating the suggested processes with the observed data is presented. The process is presented in Scheme 4.1 and described below.

As the concentration of Mn^{2+} present was near the determined K_D, ~50% of the population of BRCs had Mn^{2+} bound and ~50% were lacking Mn^{2+}. The population without bound Mn^{2+} could only undergo $P^+Q_B^-\rightarrow PQ_B$ charge recombination after light excitation. The BRCs with Mn^{2+} would be able to recover via Mn^{2+} oxidation. This population, however, would first need to undergo the light-activated conformational change related to the shift of the dimer band from 865 nm to 861 nm. Once activated, illumination of the $P_{861}Q_AQ_B$—Mn^{2+} state generated the $P_{861}^+Q_AQ_B^-$—Mn^{2+} state which could recover by $P^+Q_B^-\rightarrow PQ_B$ charge recombination with a

lifetime of 650 ms or could undergo electron donation from Mn^{2+} with a lifetime of 83 ms, forming the $P_{861}Q_AQ_B^-$—Mn^{3+} state. As the rate of Mn^{2+} oxidation is 8 fold higher, kinetics would favor Mn^{2+} oxidation. The presence of the bound Mn^{3+} and Q_B^- in the $P_{861}Q_AQ_B^-$—Mn^{3+} state means subsequent illuminations could only generate the $P_{861}^+Q_A^-Q_B^-$—Mn^{3+} state, which recovers only by charge recombination. The oxidized Mn^{3+} is not coupled electronically to the Q_B^-, similarly to all other secondary electron donors, such as cytochrome and ferrocene, thus charge recombination cannot take place. Instead, the charge recovers independently by finding redox partners in their own vicinities. However, diffusion of the bound Mn^{3+} and replacement with Mn^{2+} could occur with a lifetime of 5.1 s. Once Mn^{2+} was present, a subsequent illumination would generate the $P_{861}^+Q_A^-Q_B^-$—Mn^{2+} state, the P^+ could recover either by charge recombination or by Mn^{2+} oxidation. When the latter occurs, the doubly charged $P_{861}Q_A^-Q_B^-$—Mn^{3+} state was formed. Further illumination of this state would produce the $P_{861}^+H^-Q_A^-Q_B^-$—Mn^{3+} state which would recover via charge recombination in ~20 ns. The creation and recovery time of this state were beyond the detection limit of the equipment. Thus, flash excitation of the $P_{861}Q_A^-Q_B^-$—Mn^{3+} state would not generate a change in amplitude associated with the presence of P^+. The formation of this state is associated with the saturation of the kinetic signal during multiple flash excitation or continuous illumination. Further illumination of the sample beyond the saturation point would only affect the population without bound Mn^{2+} which would only recover by $P^+Q_B^-\rightarrow PQ_B$ charge recombination.

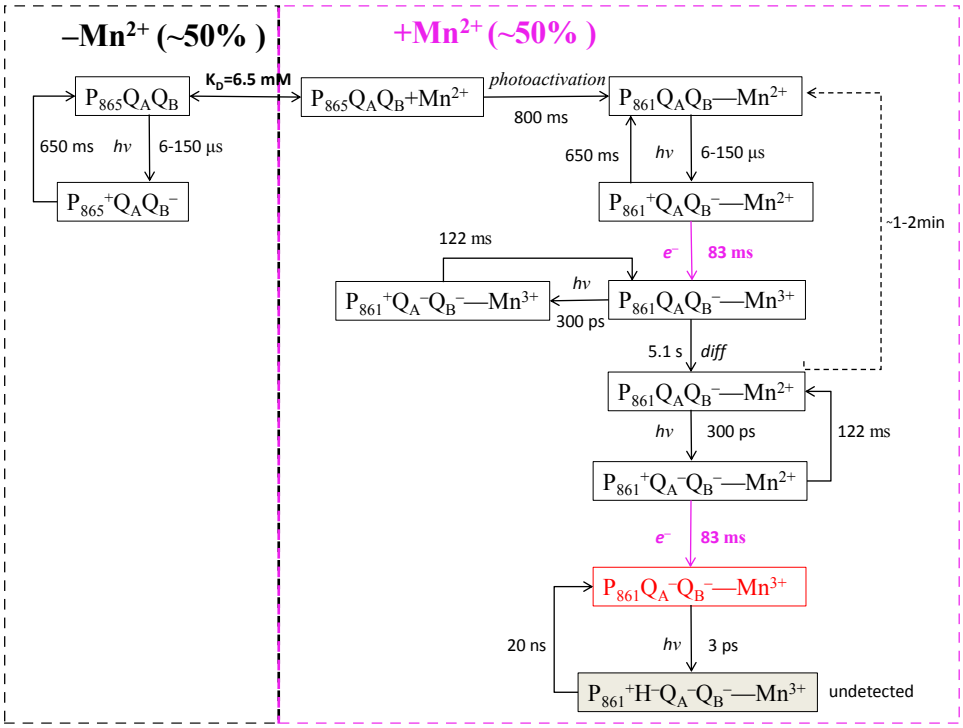

Scheme 4.1 Reaction mechanism of Mn^{2+} oxidation of P^+ in Q_B active BRCs during continuous illumination or multiple flash excitation. Explanation in the text.

The saturation of the kinetic signal before full recovery in Figure 3.5 indicates the presence of two populations of BRCs, one with bound Mn^{2+} and one without bound Mn^{2+}. The discrepancy with the full saturation observed in samples under continuous illumination could be due to the presence of UQ-10 in the cavity near monomer B in Q_B active BRCs. As results in the previous section suggest the solvent-accessible cavities as potential binding sites for Mn^{2+}, the presence of the 30 µM UQ-10 would affect the binding of Mn^{2+} to the monomer B site. This would identify the cavity near monomer B as the site for electron donation. The determined K_D in Fig. 3.4 B would thus be associated with the binding of Mn^{2+} in the specific cavity with Q_B bound to the site.

It could be argued that the K_D reported in Fig. 3.4 B would just be associated with Mn^{2+} displacing Q_B from its binding site. However, the Q_B^- formed after flash excitation remains

tightly bound in its site [82] and displacement by Mn^{2+} is unlikely. Furthermore, the pH titration both after single flash excitation and under continuous illumination (Fig. 3.13, Fig. 3.14) does not show displacement of Mn^{2+} from its binding site by Q_B in the same conditions. The decrease in the fraction of the amplitude of the slow component and the increase in the fraction of the fastest component (Fig. 3.4 B) only occurs at pH values higher than 8.9.

4.3. Electrostatic influence of the Mn-BTP complex on the native BRC cofactors

4.3.1 Estimation of the effective charge of the Mn cluster in vicinity of the dimer

The influence of the Mn association with the BRC can be seen in the increase of the dimer redox potential in the oxidative direction. The 100 mV and 55 mV difference between the potentials in the presence and absence of Mn for pH 8 and pH 9.4, respectively, represents a strong electrostatic interaction between the dimer and Mn cluster. A charged molecule within the Van der Waals distance (~ 5 Å) away from the dimer would produce a change in potential of approximately 60 mV per charge [81,82]. The total charge necessary to cause the observed effect can be determined by coupling this relationship with the determined distance of 21.6 Å from Mn to dimer. For pH 9.4, where this distance was measured, this would result in a net charge of +4 for the Mn. Since the expected oxidation state of Mn is +2, the net charge indicates the presence of multiple Mn^{2+} ions in the vicinity of the dimer. Coordination of the ions by BTP could also provide negative stabilizing charges due to the deprotonation of the amine and hydroxyl groups of the ligands. At pH 8, assuming the same distance, the 100 mV change would indicate the presence of +8 charges, accounting for a minimum of 4 Mn^{2+}. In these conditions, the amines

would be semideprotonated. Thus, if coordination at pH 8 and 9.4 is similar, the difference in the dimer potential would account for the absence of four amine protons. These observations again indicate the presence of a Mn-BTP cluster in association with the protein, involving multiple Mn^{2+} ions and ligands.

The estimation of the net charge in both conditions involves a dielectric constant of ~4.5. However, as reported by Steffen et al. [34], this value is only attributed to the environment of the BChl molecules (dimer and monomers). For the complex in solution, the local dielectric constant would be higher (~80 for water) and the dielectric constant over the electrostatic interaction between dimer and Mn would be inhomogeneous [84]. This indicates that the estimation of the net charge of the complex would represent a minimum limit.

4.3.2 Analysis of the change in Q_Y dipole moment of the monomers in the $Mn^{2+}P$ state

The electrostatic influence of the charged Mn-BTP complex also results in the broadening of the 800 nm absorption band (Fig. 3.13). The broadening is characteristic to the change in the Q_Y dipole moment of the monomers (Fig. 1.7 B). The presence of the electric field created by the charged Mn^{2+} ions destabilizes the distribution of the charge over the porphyrin macrocycle. The significance of the change in absorption indicates a close-range electrostatic interaction between the monomers and the Mn cluster. Potential solvent-accessible interaction sites would be the two cavities previously identified in Figure 4.2. The distance from the center of the Q_Y dipole to the center of the cavity is ~ 15 Å. The presence of multiple charges and the low dielectric constant around the monomers would allow for a stronger interaction. The fact that the broadening occurs

precisely at 800 nm indicates that both monomers are more or less equally affected. This would involve the presence of the Mn cluster in both sites simultaneously.

An estimation for the change in dipole moment can be given using an analysis developed in Stark spectroscopy [36,34,85]. As opposed to Stark spectroscopy, which requires an applied electric field over the entire sample, the effect of the Mn^{2+} ion charge is only local. The total change in dipole moment is related to the change in the absorption spectrum by the equation (adapted from Parson [36]):

$$A_{Mn}(800nm) - A_0(800nm) = \frac{1}{2}\left(\frac{\partial^2 A_0}{\partial v^2}\right)\frac{|\Delta\boldsymbol{\mu}\cdot\boldsymbol{E_{Mn}}|}{h^2} \quad (4.3)$$

The change in absorbance at 800 nm with Mn^{2+} present and not present (A_{Mn}(800 nm) – A_0(800 nm)) is related to the scalar product of the change in Q_Y dipole moment vector ($\boldsymbol{\Delta\mu}$) and local electric field generated by the charge ($\boldsymbol{E_{Mn}}$) by the second derivative of the absorption spectrum and Planck's constant (h). The scalar product of the change in dipole moment and electric field is calculated at 1.7×10^{-21} C^2m^{-1}. For comparison, the scalar product of the change in dipole moment and electric field on the pigment molecules (BChl and BPheo), due to the P^+Q^- dipole, ranges from 3.4×10^{-21} C^2m^{-1} to 8.9×10^{-21} C^2m^{-1} [34]. Finding the exact change in dipole moment is rendered difficult by the uncertainity in the number of charges of the Mn-BTP complex, the inhomogeneous dielectric constant and the unknown position of the cluster with respect to both monomers inside their respective cavity. However, the calculation has identified an electrostatic effect when in the presence of the Mn-BTP complex similar to the presence of the P^+Q^- dipole inside the protein.

4.4 Evolutionary implications of the use of Mn^{2+} as secondary electron donor to the oxidized dimer in native BRCs

Many different microorganisms in diverse environments, ranging from deep sea vents in oceans to the hot dessert climate, reduce or oxidize manganese in order to survive [84]. The development of the oxygen evolving cluster is an evolutionary milestone that marked the transition from anoxygenic to oxygenic photosynthesis, ultimately shaping Earth's present-day environment. The necessity of Mn ions for catalytic water splitting underlines their fundamental implications in this process. At the time of the evolutionary transition, ~2.8 billion years ago, manganese would have provided a readily available electron source for the oxidizing processes necessary for photosynthetic organisms to sustain life [42].

Studies in BRC mutants with increased oxidizing power have shown that oxidation of manganese in order to sustain the photosynthetic electron transport cycle is possible [37,49]. Mutations would have provided a selective advantage for these organisms in some of the harsh environments at the time. However, these favorable mutations that ultimately led to the oxygen evolving complex had to be preceded by a mutually beneficial relationship between manganese and the primitive reaction centers. One possibility is the use of manganese as a secondary electron donor. This requirement would be more likely pressing in an environment where the natural secondary electron donor, cytochrome c_2, is ineffective or disabled. Such conditions were recreated in Figure 3.17 where the high concentration of Mn^{2+} and BTP did not allow cyt c_2 to perform its task as secondary electron donor. Although orders of magnitude slower, Mn^{2+} oxidation was the preferred process of reducing P^+ in these circumstances. The high concentration of Mn^{2+} in solution would increase the collision frequency between cyt c_2^{2+} and Mn^{2+} [74], reducing the accessibility of cyt c_2^{2+} for electron donation to the oxidized dimer. The reduction of oxidized cyt c_2^{3+} by Mn^{2+} also provides evidence of the interaction between the two

(Fig. 3.16). Ultimately, there is experimental evidence of preference towards Mn^{2+} as a secondary electron donor to the oxidized dimer. The inability of cyt c_2^{2+} to perform the required tasks in such an environment indicates the possibility that Mn^{2+} would have been used as a secondary electron donor by primitive anoxygenic photosynthetic organisms fighting for survival. Such high (millimolar) concentrations were reported for the ancient oceans [86].

4.5 Mn^{2+}/Mn^{3+} as a redox couple in the enzymatic reactions in metalloproteins

The ability of Mn^{2+} to donate an electron is heavily dependent on its coordination by BTP molecules. Proper coordination reduces the midpoint potential significantly, allowing sufficient driving force for the process to occur even at a separation of over 20 Å. However, BTP is not commonly found in association with natural systems and is purely a synthesized product. It is unlikely that at the time of the evolutionary transition from anoxygenic to oxygenic photosynthesis BTP was found in sufficient concentrations to properly coordinate the Mn^{2+}. Although not commonly found in nature, BTP is in essence an organic compound containing four essential elements: C, H, O and N. The ligating ability to Mn^{2+} is established primarily by the amine and hydroxyl groups. The same functional groups are commonly found in numerous organic molecules such as amino acids. The ability of these groups to coordinate Mn is already reported in manganese containing metalloproteins such as superoxide dismutase, ribonucleotide reductase or pseudocatalase [42].

Superoxide dismutase uses a mononuclear Mn cofactor to catalyze the conversion of superoxides dangerous to the organism into water and hydrogen peroxide. The protein cycles between Mn^{2+}

and Mn^{3+} with an oxidation/reduction midpoint potential ranging from 290 mV to 390 mV [45,87]. Mn peroxidase is a protein which catalyzes peroxides into alcohols using Mn^{2+} as an electron donor [87]. Unfortunately, the Mn^{2+}/Mn^{3+} electrochemical potential has yet to be determined in this protein. Mn catalases reduces hydrogen peroxide to water and molecular oxygen, using a binuclear Mn cofactor which can exist in three different states: Mn^{2+}/Mn^{2+}, Mn^{2+}/Mn^{3+} or Mn^{3+}/Mn^{3+} [89,90]. The midpoint potential, however, has not been established in these systems.

The abundance of Mn performing enzymatic functions underlines its importance in life sustaining processes. The Mn^{2+} to Mn^{3+} transition is crucial to the enzymatic activity of the aforementioned proteins due to the reduced midpoint potentials of the Mn cofactors participating in redox reactions. Coordination by BTP provides soluble Mn^{2+} a low oxidation/reduction potential within the range of the Mn cofactor found in superoxide dismutase. Thus, the high degree of coordination of Mn^{2+} by BTP could allow soluble Mn^{2+} to perform reactions only seen in the core of Mn containing metalloproteins.

Conclusion

This study presents the first-time observation of rapid and efficient electron donation from Mn^{2+} ions to the oxidized dimer in native BRCs. This has been achieved by satisfying three conditions:

i) lowering the reduction/oxidation potential of the Mn^{2+} ions by coordination with BTP, ii) elevating the potential of the dimer by ~60 mV and iii) having a long enough P^+Q^- charge-separated state. The time constant for the electron transfer has been measured intrinsically at ~83 ms using single flash excitation spectroscopy (Fig. 3.3 and 3.4). Under these conditions, Mn^{2+} has been proven to be an efficient electron donor to P^+ in Q_B reconstituted BRCs (Fig. 3.3 B). The electron transfer occurs over a distance of 21.6 Å, with the Mn^{2+} likely present in the vicinity of the cavities near the BChl monomer A and B (Fig. 4.2 and 4.3). The Mn^{2+} diffuses into its pocket with a time constant of 5.10 s and this process represents the rate limiting step of the electron transfer under continuous illumination (Fig. 3.1 B and 3.5 and Section 4.2.2). The Mn^{2+} associates with the BRC with a determined binding constant of 6.45 mM in the presence of Q_B (Fig. 3.4 B). The electron transfer occurred by a conformationally-gated mechanism involving slow diffusion of the Mn^{2+} to a site where electron donation occurs (Fig. 3.5 C, Scheme 4.1).

Coordination with BTP significantly reduces the oxidation/reduction potential of the Mn^{2+} ions in solution. This creates a positive driving force of ~0.2 eV for the electron transfer to occur spontaneously from Mn^{2+} to P^+ (Section 4.2.1). At least three types of Mn^{2+} ions have been identified, with potentials varying from 332 mV to 652 mV in a pH range from 8 to 9.4 (Fig. 3.9, Table 3.1). A five or six Mn^{2+} ion coordination cluster is likely formed with BTP (Section 4.1). Measurements of electron transfer in varying pH and BTP concentrations have revealed the importance of the deprotonated amine groups of the BTP in the coordination of Mn^{2+} (Fig. 3.6 and Fig. 3.14). The apparent pK_a of the BTP coordinating the electron donor Mn^{2+} has been determined as 8.9 (Fig. 3.14 C and Fig. 3.15). The Mn^{2+} ion with the lowest potential at pH 9.4 (332 mV) is capable of auto-oxidation under ambient conditions (Fig. 3.8 and 3.10). The

electrostatic repulsion between the P^+ and the Mn^{2+} increased the redox potential of the *in situ* Mn^{2+}/Mn^{3+} by 17 mV (Fig. 3.11). The presence of a charged Mn^{2+} cluster in the vicinity also increased the P/P^+ redox potential by 54 mV at pH 9.4 and as much as 100 mV at pH 8 (Fig. 3.12, Table 3.2).

Mn^{2+} coordinated by BTP is not only able to reduce P^+, but also the oxidized form of cyt c^{3+}, indicating an unprecedented redox interaction between the two (Fig. 3.15). This interaction, coupled with the high collision frequency between cyt c^{2+} and Mn^{2+}, could explain the inability of cyt c^{2+} to perform as an electron donor to P^+ in an environment with both electron donors present (Fig. 3.16, Section 4.4). The positive association between Mn^{2+} and the anoxygenic BRC demonstrated in this study, along with the apparent disabling of the ability of cyt c^{2+} to act as a secondary electron donor in high concentration of Mn^{2+} could provide clues as to how the evolutionary transition from anoxygenic to oxygenic photosynthesis occurred ~ 2.8 billion years ago (Section 4.4). Understanding of the incorporation of Mn atoms into what eventually became the OEC in PS II could help develop an artificial photosynthetic energy converter that would prove both efficient and cost-effective.

Future Work

The current work can be extended by studying the effect of different parameters such as illumination or temperature on the electron transfer from Mn^{2+} to P^{+}. Initial studies have already reported that pre-illumination of the BRC before adding the Mn^{2+} influences the rate of electron transfer. Efforts involving variations in the time and intensity of illumination used could reveal more information about the conformationally-gated mechanism involving the diffusion of Mn^{2+} into its binding pocket. Changing the temperature, on the other hand, could reveal significant information on the diffusion process and the electronic coupling between Mn^{2+} and P^{+}. The dependence of the electron transfer rate on temperature could be mapped using an Arhenius plot. Using Marcus electron transfer theory one could then calculate the activation energy of the electron transfer and ultimately the donor-acceptor electronic coupling and reorganization energy.

As BRCs are naturally membrane-bound proteins, studies involving the electron transfer in BRCs incorporated into artificial liposomes could also provide information on the Mn^{2+} binding site and the diffusional ability and charge of the Mn^{2+}-BTP cluster. Different head-group charge of the lipids composing the liposome could have an effect on the ability of Mn^{2+} to diffuse to the binding site. Preliminary studies show that electron transfer was limited by diffusion in liposomes with negative, neutral or positive head-groups charge. In negatively-charged lipids, the electron transfer was shown to occur even at pH 8. Spectroscopic analysis revealed a change in the dipole moment of the BChl monomer absorption band and shift of the BChl dimer band, indicating a similar influence of the presence of Mn^{2+} in the two cavities. A conformationally-gated mechanism was also reported in neutral and positively charged head-group lipids. Spectroelectrochemical titrations are underway to determine the driving force of the electron transfer under these conditions.

The evolutionary mechanism that characterized the transition from anoxygenic to oxygenic photosynthesis could be related to the use of Mn^{2+} as a secondary electron donor to P^{+}. However, since the natural availability of the BTP coordinating ligands is limited, another molecule could have performed the same task. Amino-acids have already been proposed as alternative ligands to BTP in section 4.5. A study concerning the coordination of BTP by amino-acid residues might produce a similar drop in Mn^{2+} potential as BTP coordination. As both amine and hydroxyl groups are suggested to participate in coordinating Mn^{2+} amino-acids that contain both groups might yield successful results. Serine, threonine and tyrosine contain both groups and could be used as coordinating ligands. Their structure is shown if Figure 8.1.

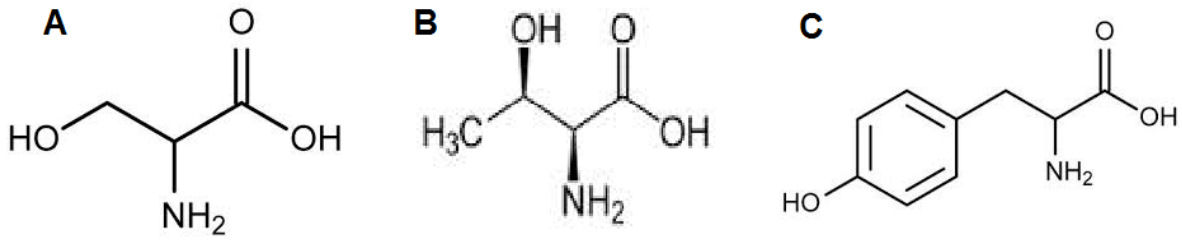

Figure 8.1 Structure of amino-acids containing hydroxyl groups. (A) Serine. (B) Threonine. (C) Tyrosine

References

1 Reece JB, Urry LA, Cain ML, Wasserman SA, Minorsky PV, Jackson RB. Campbell Biology. Benjamin Cummings / Pearson; 2011. p. 570-571.

2 Cavalier-Smith T. Proc. Biol. Sci. 2006;361(1470):969-1006.

3 Nisbet EG, Fowler CMR. Proc. Biol. Sci. 1999;266(1438):2375-2383.

4 Parkinson CL. Coming Climate Crisis?: Consider the Past, Beware the Big Fix. Rowman & Littlefield; 2010. p. 35-37.

5 Des Marais D. Science. 2000;289(5485):1703-1705.

6 Mann P, Gahagan L, Gordon MB. Giant Oil and Gas Fields of the Decade, 1990-1999. Tulsa, Oklahoma: American Association of Petroleum Geologists; 2003. p. 50.

7 Office of Science and Office of Energy Efficiency and Renewable Energy. Scientific Report. Rockville, Maryland: U.S. Department of Energy; 2009. Available from: http://genomicscience.energy.gov/biofuels/2005workshop/2005low_lignocellulosic.pdf.

8 Raymond J, E. BR. Coordination Chemistry Reviews. 2008;252:377–383.

9 Marshall J. Nature. 2014;510:22-24.

10 Bittl R, Kawamori A. Photosystem II: The Light-Driven Water:Plastoquinone Oxidoreductase. Springer; 2006. p. 390-402.

11 Dismukes GC, Klimov VV, Baranov SV, Kozlov YN, DasGupta J, Tyryshkin A. PNAS. 2001;98(5):2170-2175.

12 Hunter CN, Daldal,F, Thurnauer MC, Beatty JT. The Purple Phototropic Bacteria. Dordrecht, The Netherlands: Springer Verlag; 2008.

13 Deshmukh SS, Williams JC, Allen JP, Kálmán L. Biochemistry. 2011;50(3):340-348.

14 Deshmukh SS, Akhavein H, Williams JC, Allen JP, Kálmán L. Biochemistry. 2011;50(23):5249–5262.

15 Deshmukh SS, Williams JC, Allen JP, Kálmán L. Biochemistry. 2011;50(16):3321–3331.

16 Xiong J, Fischer WM, Inoue K, Nakahara M, Bauer CE. Science. 2000;289:1724-1732.

17 Koepke J, Krammer E, Klingen A, Sebban P, Ullmann G, Fritzsch G. Journal of Molecular Biology. 2007; 371(2):396-409.

18 Umena Y, Kawakami K, Shen J, Kamiya N. Nature. 2011;473(7345):55-U65.

19 Yeates T, Komyia H, Chirino A, Rees D, Allen J, G F. PNAS. 1988; 85(21):7993-7997.

20 Ferreira K, Iverson T, Maghlaoui K, Barber J, Iwata S. Science. 2004;303(5665):1831-1838.

21 Yano J, Yachandra V. Chemical Reviews. 2014;114:4175-4205.

22 Cook SA, Borovik A . Nature Chemistry. 2013;5:259-260.

23 Stowell M, McPhillips T, Rees D, Soltis S, Abresch E, Feher G. Science. 1997;276(5313):812-815.

24 Cámara-Artigas A, Brune,D, Allen JP. Proc. Natl. Acad. Sci. U.S.A. 2002;99:11055-11060.

25 Feher G, Allen JP, Okamura MY, Rees DC. Nature. 1989;339:111-116.

26 Axelrod HL, Abresch EC, Okamura MY, Yeh AP, Rees DC, Feher G. J. Mol. Biol. 2002;319:505-515.

27 Nugent J. Eur. J. of Biochem. 1996;237(3):519-531.

28 Deisenhofer J, Michel H, Huber R. Trends in Biol. Sci. 1985;10(6):243-248.

29 de Paula JC, Innes JB, Brudvig GW. Biochem. 1985;24:8114-8120.

30 Maxwell R. Biology Newsletter Archive. [Internet]. 2013 Available from: http://biomoocnews.blogspot.ca/2013/10/daily-newsletter-october-9-2013.html.

31 Marcus R. J. Chem Phys. 1957;26(872).

32 Marcus R. J. Chem. Phys. 1957;26(867).

33 Moser CC, Chobot SE, Page CC, Dutton PL. Bioch. et Bioph. Acta. 2008;1777:1032-1037.

34 Steffen MA, Lao K, Boxer SG. Science. 1994;264:810-816.

35 Clayton RK. Photosynth. Res. 2000;73:63-71.

36 Parson WW. Modern Optical Spectroscopy. Seattle, WA: Springer; 2009. p. 182-186.

37 Kálmán L, LoBrutto R, Allen JP, Williams JC. Biochem. 2003;42:11016-11022.

38 Ferguson A, Darwish A, Graham K, Schmidtman M, Parkin A, Murrie M. Inorg. Chem. 2008;47:9742-9744.

39 Liu SY, Kono M, Ebrey TG. Biophys. J. 1991;60:204-214.

40 Tóth-Boconádi R, Dér A, Keszthelyi L. Biophys. J. 2000;78(6):3170–3177.

41 Sarma R, Perumal A, Baruah J. J. of Coord. Complex. 2009; 62(9):1513-1524.

42 Wieghardt K. Angew. Chem. Int. Ed. 1989;28:1153-1172.

43 Sheriff T, Carr P, Coles S, Hursthouse M, Lesin J, Light M. Inorg. Chim. Acta. 2004;357(9):2494-2502.

44 Kálmán L, Williams JC, Allen JP. Biochem. 2011;50:3310-3320.

45 Leveque VJP, Vance CK, Nick HS, N. SD. Biochem. 2001;40:10586-10591.

46 Sheng Y, Gralla EB, Schumacher M, Cascio D, Cabelli DE, Valentine JS. PNAS. 2012;109(36):14314–14319.

47 Khorobrykh A, Dasgupta J, Kolling DRJ, Terentyev V, Klimov VV, Dismukes GC. Chem.BioChem. 2013;14:1725 – 1731.

48 Terentyev VV, Shkuropatov AY, Shkuropatova VA, Shuvalov VA, Klimov VV. Biochemistry (Moscow). 2011;76(12):1360-1366.

49 Thielges M, Uyeda G, Camara-Artigas A, Kallman L, Williams JC, Allen JP. Biochem. 2005;44(20):7389-7394.

50 Deshmukh SS. PhD Thesis. Montreal: Concordia University; 2013.

51 Feher G, Okamura MY. The photosynthetic bacteria. New York: Plenum Press; 1978. p. 349-386.

52 Muller MG, Griebenow K, Holzwarth AR. Biochim. Biophys. Acta. 1991;1098:1-12.

53 Maróti P, Wraight CA. Prog. Photosynth. Res. 1987;2:401-404.

54 Williams JC, Alden RG, Coryell VH, Lin X, Murchison, A. H, Peloquin JM, Woodbury,NW, Allen JP. Research in photosynthesis. Dordrecht, The Netherlands: Kluver; 1991. p. 377-380.

55 McPherson PH, Okamura MY, Feher G. Biochim. Biophys., Acta. 1993;1144:309-324.

56 Kálmán L, Maróti P. Biochem. 1997;36:15269-15276.

57 Lin X, Murchison HA, Nagarajan V, Parson WW, Allen JP, Williams JC. Proc. Natl. Acad. Sci. U.S.A. 1994;91:10265-10269.

58 O'Reilly JE. Biochim. Biophys. Acta. 1973;292:509-515.

59 Moss DA,LM,BM,aMW. FEBS Lett. 1991;33-36:283.

60 Tang K, Williams JC, Allen JP, Kálmán L. Biophys. J. 2009;96:3295-3304.

61 Atkins P, de Paula J. Physical Chemistry 9th ed. New York: W.H. Freeman & Company; 2009. p. 811.

62 Deshmukh SS, Tang K, Kálmán L. J. Am. Chem. Soc. 2011;133:16309-16316.

63 Clayton RK, Straley SC. Biophys. J. 1972;12:1221-1234.

64 Fritz F, Moss DA, Mäntele W. FEBS Lett. 1992;297:1-2.

65 Pettigrew GW, Bartsch RG, Meyer TE, Kamen MD. Biochim. Biophys. Acta. 1978;503(3):509–523.

66 Prince R, Bashford C. Biochim Biophys Acta. 1979;546(3):447-454.

67 van der Wal HN, van Grondell R, Millett F, Knaff,DB. Biochim. Biophys. Acta. 1987;893(3):490–498.

68 Blankenship R, Hartman H. Trends Biochem. Sci. 1998;23(3):94-97.

69 Baranov SV, Tyryshkin AM, Katz D, Dismukes GC, Ananyev GM, Klimov VV. Biochem. 2004;43(7):2070-2079.

70 Laureys T, Pinto ISS, Soares CFM, Boppudi HB, Soares HMVM. J. Chem. Eng. Data. 2012;57:87-92.

71 Vass I, Styring S. Biochem. 1990;30:830-839.

72 Kálmán L, Williams JC, Allen JP. Adv. Photosynth. Resp. 2005;22:715-727.

73 Ortega JM, Mathis P. Photosynth. Res. 1992;34(1):127-127.

74 Kálmán L, Arlene L, Haffa M, Williams JC, Woodbury NW, Allen JP. J. Porphyrins Phthalocyanines. 2007;11(3-4):205-211.

75 Moser CC, Dutton LP. Biochem. 1988;27:2450-2461.

76 Page CC, Moser CC, Chen X, Dutton PL. Nature. 1999;402:47-52.

77 Maroti P, Kirmaier C, Wraight C, Holten D. Biochim. Biophys. Acta. 1985;810:132-139.

78 Roszak AW, McKendrick K, Gardiner AT, Mitchell IA, Isaacs NW, Cogdell RJ, Hashimoto H, Frank HA. Structure. 2004;12:765-773.

79 Roszak AW, Gardiner AT, Isaacs NW, Cogdell RJ. Biochem. 2007;46:2909-2916.

80 Diner BA, Schenck CC, de Vitry C. Biochim. Biophys. Acta. 1984;766(1):9-20.

81 Hay S, Westerlund K, Tommos C. Biochem. 2005;44:11891-11902.

82 Williams JC, Haffa ALM, McCulley JL, Woodbury NW, Allen JP. Biochem. 2001;40:15403-15407.

83 Renge I, Mauring K. Spectrochim. Acta A: Mol. Biomol. Spectr. 2013;102:301–313.

84 Gounot AM. FEMS Microb. Rev. 1994;14(4):339-349.

85 Schatz G. FEBS Letters. 2003;27576(1-3):1-2.

86 Miller AF. Curr. Opin. Chem. Biol. 2004;8:162-168.

87 Gold MH, Youngs HL, Sollewijn Gelpke MD. Manganese and Its Role in Biological Systems. New York: Marcel Dekker Publishers; 2000. p. 559-586.

88 Dismukes GC. Chem. Rev. 1996;2909-2926:96.

89 Yoder DW, Hwang J, Penner-Hahn JE. Manganese and Its Role in Biological Systems. New York: Marcel Dekker Publishers; 2000. p. 527-557.

90 Lawlor DW. Photosynthesis. England, UK: Longman Scientific and Technical Publications; 1993. p. 1-15.

91 Hohmann-Marriott MF, Blankenship RE. Annu. Rev. Plant Biol. 2011;62(515):515-548.